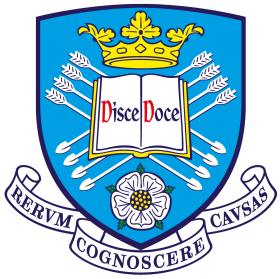

The University Of Sheffield.

Electron identification efficiency and W^+W^- cross section measurements with the ATLAS detector

Elias Michael Rüttinger

A thesis submitted in partial fulfilment of the requirements for the degree of Doctor of Philosophy

The University of Sheffield
Department of Physics and Astronomy

September 2020

Acknowledgements

First and foremost I would like to thank my supervisor, teacher and mentor Kristin Lohwasser, who supported me from the time I was a master student at Humboldt University, even in some more difficult times. Beside of all the useful tips and tricks and her open ear for many questions, she also gave a lot of useful comments on the final text of this thesis. Without her, this thesis would not exist.

Furthermore I want to thank the many wonderful people I worked together in ATLAS at CERN, DESY, Humboldt University and the University of Sheffield. My time at CERN was probably one of the times in my life I enjoyed the most, therefore everybody I met there or at a related workshop should feel addressed. Special thanks go to the Sheffield Crew, especially Philip Sommer and Hannes Mildner, both of them had many useful comments on my work on electron identification and on the matrix element method. I also want to thank everybody from DESY, I had a wonderful time and many nice lunches at the lake. In addition, I want to thank Cyril Becot and Stefan Richter, who helped me to finalise the new Z_{mass} measurements by asking many critical questions. I also want to thank David Prinz, for proofreading the theory chapter and for many fruitful discussions about physics.

Most of all I want to thank my little family for their patience, Büşra and Leo, who always supported me and will always make me happy.

Abstract

This thesis concludes the doctoral studies done within the last four years at DESY in Zeuthen and the University of Sheffield. An update on the measurement of electron identification efficiencies is presented, providing a more coherent background estimate resulting in lower systematic uncertainties than in previous measurements. The measurement of the W^+W^- production cross section using the ATLAS 2015 and 2016 datasets and contributions made to this measurement are described. This includes the preparation of the Bayesian data unfolding and studies of the background composition. Furthermore studies towards a multivariate analysis of the same process making use of the matrix element method is presented. A proof of principle on particle level events is presented as well as the ingredients for the implementation at detector level.

Declaration

I, the author, confirm that the thesis is my own work, except where specific reference is made to the work of others. I am aware of the university's guidance on the use of unfair means*. This work has not been previously been presented for an award at this, or any other, university.

Publications arising from this thesis

Working on this thesis lead to personal contributions in three publications by the ATLAS collaboration:

- Similar measurements of electron identification efficiencies as described in Chapter 5 with contributions from me were presented before in two publications [1, 2]. However, the method presented in this thesis underwent significant changes since then, as described in detail in Chapter 5. Therefore the presented analysis in Chapter 5 can be regarded as independent of the aforementioned publications.
- Chapter 6 describes a measurement published before in Reference [3], however focusing on my personal contributions to this analysis.

The mentioned publications are also referred to specifically in the corresponding sections of the thesis.

Elias Rüttinger
September 2020

*www.sheffield.ac.uk/ssid/unfair-means

Contents

List of Figures

List of Tables

Chapter 1

Introduction

Talking about modern physics is talking about particle physics. The etymology of the word "physics", already gives a hint what it is about: The ancient greek word $\phi\upsilon\sigma\iota\kappa o\varsigma$ – "natural, regarding nature" – coming from $\phi\upsilon\sigma\iota\varsigma$ – "nature, origin" – stems back to the Proto-Indo-European *bheue-, which has interestingly a meaning of "to be, exist, grow" [4]. This is the same root as for the english word "build". So one could say physics is about the very existence of everything, and particle physics is about the key ingredients which build up our world.

Using particle accelerators to produce particles in collisions with higher and higher energies, allowed particle physicists to discover a huge number of elementary particles. These elementary particles are found to be linked to very basic symmetries of nature. The developed state of the art Standard Model of particle physics (SM), is in fact a quantum field theory (QFT) having a gauge symmetry of $U(1) \times SU(2) \times SU(3)$. I, personally, believe, that these symmetries are a beautiful discovery, since it shows, that the universe itself is based on logic, even if we do not know all of it yet.

1.1 Open questions

In fact a lot of things are not understood yet. The discovery of the Higgs boson in 2012 by the ATLAS and CMS collaborations [5, 6] closed the last gap of the SM. Physicists had hoped, that the Large Hadron Collider (LHC), the accelerator providing the proton collisions for these experiments, would make it possible to truly discover hints of new physics phenomena like supersymmetry [7]. These hopes were disappointed quickly, however it makes it even more puzzling, as this leaves all open questions unexplained. One of the great questions of this time is the nature of dark matter. It turns out that the visible matter of our universe described

by the SM actually makes up only roughly one fifth of the total matter. The rest stems from dark matter, which has strong astronomical evidence of existence but can not be described in any way with the tools provided by the SM yet [8, 9].

Another open question is the missing link of gravitation and the SM. The recent discovery of gravitational waves [10] further underlines the validity of Einstein's general relativity. However this theory has no particle level explanation or at least no link to the microscopic world.

A rather simple example is the observation that neutrinos mix and thus should have mass [11–13] , a fact not covered by the SM, even if it can be easily included.

The last example is the universe itself, which seemingly only consists of matter but lacks antimatter and thus seems to break with its own basic rules of symmetry [14].

1.2 Outline of this thesis

An ordinary thesis like this one of course cannot provide any answer to these open questions. However it can try to give little contributions to the discovery of new hints which might lead to new answers in the future. This happens in two ways:

1. Optimising the experimental basics. A great fraction of work went into the optimisation of electron identification efficiency measurements inside the ATLAS detector. These efficiencies are needed by all kinds of analyses making use of electrons. Thus, improving them, is contributing a little to a broad range of scientific advances.

2. Contribution to actual physics measurements. The focus lays on cross section measurements of W^+W^- production as well as providing input and ideas for a better future measurement.

The second point of course is only one of many possible measurements to be undertaken. However it is a rather rare but unique SM process. Providing precise measurements of the differential cross section is helping to understand the SM and its prediction on a deeper level. On the other hand, if the prediction fail to describe the physical measurement it can also provide indirect evidence for unknown new physics. This process contains a self-coupling of vector bosons. This has not been measured to the same accuracy as other couplings and thus could be affected by new physics if higher resolution was to be applied. Thus, measuring and understanding W^+W^- pair production provides a good test how of how well we understand what we think to understand.

In order to give an overview over the used terminology and the theoretical background, the SM will be discussed briefly in Chapter 2. Also the collision of hadrons as happening in the LHC is discussed here. For understanding the key elements of the measurement, the experimental environment, that is the ATLAS detector and the LHC, is introduced in Chapter 3. Chapter 4 gives a brief overview on how different types of particles are reconstructed within the ATLAS detector. The first main topic, the measurement of identification efficiencies, is discussed in Chapter 5. The following two chapters focus on the second main topic mentioned above: Chapter 6 focuses on the W^+W^- cross section measurement using ATLAS data recorded in 2015 and 2016, while Chapter 7 discusses the matrix element method as a more sophisticated way of separating signal and background and also the sub-processes of W^+W^- generation.

Chapter 2

The Standard Model of particle physics

This chapter gives a brief introduction into the basic theoretical concepts of particle physics by introducing the Standard Model of particle physics. After a short historical overview in the first Section 2.1, the second Section 2.2 gives a brief overview of the very basic concepts of the SM by introducing the fundamental particles and interactions. Section 2.3 briefly discusses the electroweak sector of the SM in a bit more detail, since it will be relevant later in this thesis. The fourth Section 2.4.3 gives an introduction how these concepts are applied in the light of hadronic collider experiments as the LHC, which will be introduced in the following Chapter 3.

2.1 A short history of the Standard Model

With growing knowledge from collider experiments in the last century a theory of particle physics emerged, the SM. Paul Dirac was was the first to successfully introduce a Lorentz-invariant description of the electron in 1928 [15] and also introduced the concept of emission and absorption of radiation [16]. His theory was soon expanded by many others like Shin'ichirō Tomonaga, Julian Schwinger and Richard Feynman and was developed into the first QFT in the late 40s, quantum electrodynamics (QED), which describes the interactions of electrons and photons to an unknown precision [17–19]. It was also Feynman who introduced so-called Feynman diagrams as pictorial representations of QFT interaction processes. QED has an underlying abelian gauge symmetry ($U(1)$).

The growing knowledge of the role of symmetries and group theory in particle physics lead to the concepts of gauge theories. Chen Ning Yang and Robert

Mills found out that a non-abelian gauge group ($SU(3)$) could explain the strong interaction in the 1954 [20].

Based on Yang-Mills theories, Sheldon Lee Glashow could successfully introduce a ($SU(2)$) symmetry describing the weak interaction by combining it with the $U(1)$ symmetry from QED in 1961 [21]. Soon after, this ansatz was expanded by Steven Weinberg and Abdus Salam [22, 23] by introducing Higgs mechanism [24–26] into the theory and thus giving rise to the masses of the interacting particles and also the weakness of the weak force.

2.2 Fermions, symmetries and bosons

The SM is a quantum gauge field theory, that is particles are described by fields. Interactions of particles arise from the gauge symmetries of these fields, where each symmetry gives rise to a bosonic field. The gauge group of the SM is

$$\mathcal{G}_{\text{SM}} = U(1)_Y \times SU(2)_L \times SU(3)_C \ , \tag{2.1}$$

and thus contains $1 + 3 + 8$ different force fields. The SM Lagrangian can be written as [27]*:

$$\begin{aligned}\mathcal{L}_{\text{SM}} = &\underbrace{-\frac{1}{2}\,\text{Tr}\big(F_{\mu\nu}F^{\mu\nu}\big)}_{\text{Section 2.2.1}} + \underbrace{\bar{\Psi}_L i\gamma^\mu D_\mu \Psi_L}_{\text{Section 2.2.2}} \\ &+ \underbrace{(D_\mu\Phi)^\dagger D^\mu\Phi - V(\Phi)}_{\text{Section 2.2.3}} + \underbrace{\left(\frac{1}{2}\Psi_L^T \Upsilon \Phi \Psi_L + h.c\right)}_{\text{Section 2.2.4}}\end{aligned} \tag{2.2}$$

The Lagrangian can be split up into four main pieces, each of them will be discussed in the respective section denoted below it. Main sources for this part were the lecture notes from Buchmüller and Lüdeling [27] and Novaes [28], as well as the books by Peskin and Schroeder [29], Berger [30], Nachtmann [31] and Cottingham and Greenwood [32]. Some parts were already described in my master thesis [33], which is why similarities could not be avoided.

2.2.1 Vector bosons

The $\text{Tr}\big(F_{\mu\nu}F^{\mu\nu}\big)$ term is an inner product of the field strength tensors. Each of the three symmetries in Equation (2.1) has its own field strength tensor, which is given

*Ignoring gauge fixing terms and ghost fields.

via

$$F^a_{\mu\nu} := \partial_\mu X^a_\nu - \partial_\nu X^a_\mu + g C^a_{bc} X^b_\mu X^c_\nu \ , \tag{2.3}$$

with X being a vector boson field. In this equation, g is a generic coupling constant and C^a_{bc} is the structure constant of the corresponding symmetry group. The vector boson field can be expressed via its basis decomposition

$$X_\mu = \sum_a X^a_\mu T^a \ , \tag{2.4}$$

with T^a being the generators of the Lie group.

It is possible to sketch a general non-abelian field tensor as follows [28]

$$F \propto (\partial X - \partial X) + g[XX] \ . \tag{2.5}$$

Because F is contracted within the Lagrangian, it looks like the following:

$$\mathcal{L}_X \propto \underbrace{(\partial X - \partial X)^2}_{\text{propagator}} + \underbrace{g(\partial X - \partial X)[XX]}_{\text{triple couplings}} + \underbrace{g^2[XX][XX]}_{\text{quartic couplings}} \tag{2.6}$$

Thus, a non-abelian theory contains a self coupling of its gauge bosons.

The gauge group $\mathcal{G}_{\text{SM}}$ can be separated into two parts: $U(1)_Y \times SU(2)_L$ corresponds to the electroweak sector and $SU(3)$ corresponds to the strong interaction. It is a unification of electro-magnetic and weak interaction, which is discussed in more detail in part III of this section. From this, four force fields are obtained:

$$\begin{aligned} SU(2)_L &: W^1_\mu \ , \ W^2_\mu \ , \ W^2_\mu \\ U(1)_Y &: B_\mu \end{aligned} \tag{2.7}$$

After symmetry breaking these will result in the heavy $W^\pm$ and Z bosons and the massless photon γ.

The $SU(3)_C$ is the quantum chromodynamics (QCD) gauge group, responsible for the strong interaction, resulting in 8 massless gluon fields.

2.2.2 Fermions

The SM contains two types of fermionic spinor fields, leptons and quarks. The latter carry colour charge while leptons do not.

For each lepton ℓ a correspondingly named neutrino ν_ℓ exists. Neutrinos are not carrying electric charge and thus can only interact weakly (see below). The three lepton generations are electron (e), muon (μ) and tau lepton (τ). The quarks are named up, down, strange, charm, top, and bottom, usually indicated by their

first letter. For all of these particles there exists also an antiparticle with opposite charge.

Fermions are described by Dirac spinors, meaning they are relativistic spin 1/2 particles. These are solutions of the Dirac equation

$$(i\partial\!\!\!/ - m)\psi = 0 \ . \tag{2.8}$$

One can split those up into a right-handed ψ_R and a left-handed part ψ_L by applying the projection operators to them:

$$\psi_L = \frac{1}{2}(1-\gamma^5)\psi \ , \ \psi_R = \frac{1}{2}(1+\gamma^5)\psi \tag{2.9}$$

γ^5 denotes the fifth gamma matrix defined via the product of the four Dirac matrices γ^i

$$\gamma^5 := -i\gamma^0\gamma^1\gamma^2\gamma^3 \ . \tag{2.10}$$

In the Glashow-Weinberg-Salam model left-handed fermions transform as weak isospin doublets

$$\begin{pmatrix}\nu_e\\ e\end{pmatrix}_L, \begin{pmatrix}\nu_\mu\\ \mu\end{pmatrix}_L, \begin{pmatrix}\nu_\tau\\ \tau\end{pmatrix}_L \text{ and } \begin{pmatrix}u\\ d'\end{pmatrix}_L, \begin{pmatrix}c\\ s'\end{pmatrix}_L, \begin{pmatrix}t\\ b'\end{pmatrix}_L \tag{2.11}$$

under $SU(2)_L$. Thus, in the picture of weak interaction, particles like the electron neutrino and the electron are not independent but the two sides of the same coin. By interacting with the W fields, these "coins" can be flipped, meaning they transform into each other.

Quarks are not eigenstates of the weak interaction and down-type quarks d_i' mix like

$$d_i' = \sum_{j=1}^{3} V_{ij} d_j \tag{2.12}$$

with V_{ij} being the Cabibbo-Kobayashi-Maskawa mixing matrix [34].

Right-handed fermion fields only transform as $SU(2)$ singlets

$$e_R \ , \ \mu_R \ , \ \tau_R \ \text{ and } \ u_R \ , \ d_R \ , \ c_R \ , \ s_R \ , \ t_R \ , \ b_R \ . \tag{2.13}$$

This theory does not include right-handed neutrinos. All of the fields in Eq. (2.11) and (2.13) transform under the hypercharge group $U(1)_Y$.

The conserved currents expected from those fields are the weak isospin and the hypercharge current, with its charges T and Y. The fields themselves are coupling to these charges by the couplings g and g', respectively. The specific quantum

Table 2.1: Quantum numbers of the leptons and quarks (taken from Ref. [31]). Listed are the weak isospin T, its third component T_3, the weak hypercharge Y and the electric charge Q.

			T	T_3	Y	Q
$\begin{pmatrix}\nu_e\\ e\end{pmatrix}_L$	$\begin{pmatrix}\nu_\mu\\ \mu\end{pmatrix}_L$	$\begin{pmatrix}\nu_\tau\\ \tau\end{pmatrix}_L$	$1/2$ $1/2$	$1/2$ $-1/2$	$-1/2$ $-1/2$	0 -1
e_R	μ_R	τ_R	0	0	-1	-1
$\begin{pmatrix}u\\ d'\end{pmatrix}_L$	$\begin{pmatrix}c\\ s'\end{pmatrix}_L$	$\begin{pmatrix}t\\ b'\end{pmatrix}_L$	$1/2$ $1/2$	$1/2$ $-1/2$	$1/6$ $1/6$	$2/3$ $-1/3$
u_R d_R	c_R s_R	t_R b_R	0 0	0 0	$2/3$ $-1/3$	$2/3$ $-1/3$

numbers for quarks and leptons are listed in Table 2.1.

The third component of the weak isospin is denoted as T_3. Together with the hypercharge, it satisfies the Gell-Mann–Nishijima relation

$$Q = T_3 + \frac{1}{2}Y \tag{2.14}$$

for the electric charge Q. This is because QED and electroweak interaction can be described as one unified interaction, as explained in a bit more detail in the next section.

Quarks transform as colour triplets under $SU(3)_C$. Thus, all quarks come in three different types, each type carrying one of the colour charges red, blue or green. Due to the strength of the strong interaction, no naked colour charges can be observed. This is called quark confinement.

2.2.3 The Higgs sector

The SM Higgs mechanism adds a scalar isospin doublet Φ to the Lagrangian, this doublet contains four real scalar fields. The Higgs mechanism introduces a potential on this doublet, denoted as $V(\Phi)$ in Eq. (2.2), and reads:

$$V(\Phi) = \mu^2\Phi^\dagger\Phi - \frac{1}{2}\lambda\left(\Phi^\dagger\Phi\right)^2 \quad , \quad \mu^2 > 0 \tag{2.15}$$

The vacuum expectation value is

$$v = \sqrt{2}\mu/\lambda \ , \tag{2.16}$$

and thus the ground state of the potential is not at the origin, leading to a spontaneously broken symmetry. Choosing a different basis decomposition results in one massless field (the photon γ) and three heavy fields, the Z and $W^{\pm}$ bosons, absorbing three of the four scalar fields of Φ in their mass terms. The residual degree of freedom is resulting in a scalar boson, the Higgs boson H. As a result the original $SU(2)$ symmetry is not visible anymore in the resulting SM Lagrangian, the leftover symmetry can be identified as the electromagnetic $U(1)$ symmetry [32].

The resulting masses of the heavy gauge bosons Z and $W^{\pm}$ as well as for the resulting Higgs particle H are

$$\begin{aligned} M_H &= \lambda v \\ M_W &= e\frac{v}{2}\sin\theta_W \\ M_Z &= \frac{M_W}{\cos\theta_W} \\ M_\gamma &= 0 \ . \end{aligned} \tag{2.17}$$

Here $\theta_W = \tan^{-1} g/g'$ is the Weinberg angle, defined by the coupling strengths of the original B and W fields [27], and e is the electric charge.

2.2.4 Yukawa couplings

The Higgs field also provides an explanation for the masses of the fermions to be non-zero – however not the masses themselves – via Yukawa interaction. For example the lepton term writes as

$$\mathcal{L}^{\ell}_{\text{Yukawa}} := \sum_i \bar{\psi}_i \left(i\gamma^\mu \partial_\mu - m_i - \frac{m_i}{v} H \right) \psi_i \tag{2.18}$$

Thus, also fermions gain mass, with the exception of neutrinos. The mass generation of the vector bosons can be expressed similarly [30]. Therefore one can say that "particles having mass" is equivalent to the statement "particles are coupling to the Higgs boson".

All the things discussed previously, are summarised in Figure 2.1. It shows a sketch of the full particle content of the SM, as well as the interactions between these particles. Particles are represented as circles while the reign of a force is

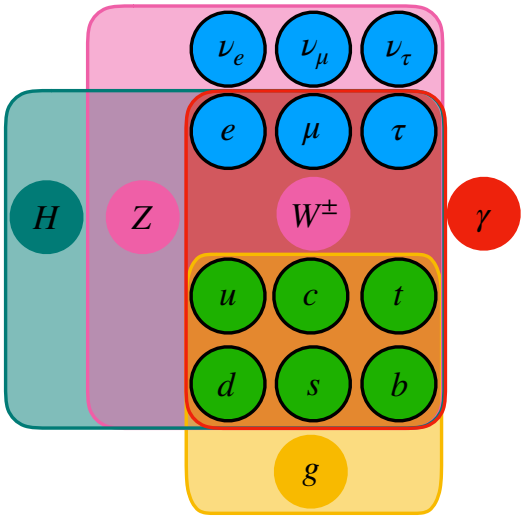

Figure 2.1: Overview over the Standard Model of particle physics (SM). The circles represent particles, the boxes represent the forces being able to act on them. Boson circles are coloured in the respective colour of the force boxes. Fermion circles are framed in black. Leptons are blue and quarks are green. The weak force is magenta, the electromagnetic force is represented in red. The eight gluons are shown in yellow. Colour charges are not represented. The Higgs boson is shown in a cyan colour. Every particle with mass is inside the Higgs box. Since the photon is not self-interacting, it is drawn outside its force box.

drawn as a box. Particles present within one force box can interact with each other through this force. Not represented are the different colour charges, the antiparticles and the fact that the weak force is only coupling to left-handed fermions.

2.3 Electroweak theory and triple gauge couplings

The SM Lagrangian contains many self coupling terms between the various vector bosons and the scalar Higgs boson. Of special interest in W^+W^- production is the triple gauge coupling (TGC) vertex. By writing down other possible operators of vector boson self couplings, new couplings denoted as anomalous triple gauge coupling (aTGC), can be introduced [35]:

$$\begin{aligned}\mathcal{L}_{WWV} = ig_{WWV}\Big[&g_1^V\left(W^+{}_{\mu\nu}W^{-\mu} - W^{+\mu}W^-{}_{\mu\nu}\right)V^\nu \\ &+ k^V W^+{}_\mu W^-{}_\nu V^{\mu\nu} + \frac{\lambda^V}{M_W^2}W^{+\nu}{}_\mu W^{-\rho}{}_\nu V_\rho^\mu\Big] \ ,\end{aligned} \tag{2.19}$$

where $V = Z, \gamma$, $g_{WWZ} = e\cos\theta_W$ and $g_{WW\gamma} = e$. In Eq. (2.19) only terms conserving charge conjugation (C) and parity (P) separately are considered. In the SM the couplings are $g^V = 1$, $k^V = 1$ and $\lambda^V = 0$, thus all deviations

$$\Delta g_1^Z = 1 - g_1^Z \ , \ \Delta k^Z = 1 - k^Z, \lambda^Z \ , \ \Delta g_1^\gamma = 1 - g_1^\gamma \ , \ \Delta k^\gamma = 1 - k^Z \text{ and } \lambda^\gamma \quad (2.20)$$

unequal to 0 are regarded as anomalous. In order to keep electromagnetic gauge invariance, it is necessary to fix Δg_1^γ to 0 [36]. It is also convenient to write this down in terms of an effective field theory (EFT) as an expansion of the SM by adding dimension-six operators [35]:

$$\mathcal{L} = \mathcal{L}_{WWV,\mathrm{SM}} + \sum_i \frac{c_i}{\Lambda^2}\mathcal{O}_i + ... \quad (2.21)$$

The relevant dimension-six operators $\mathcal{O}_i$ for the TGC vertex are

$$\begin{aligned} \mathcal{O}_{\mathrm{WWW}} =& \mathrm{Tr}\left[W_{\mu\nu}W^{\nu\rho}W_\rho^\mu\right] \\ \mathcal{O}_{\mathrm{W}} =& (D_\mu\Phi)^\dagger W^{\mu\nu}(D_\nu\Phi) \\ \mathcal{O}_{\mathrm{B}} =& (D_\mu\Phi)^\dagger B^{\mu\nu}(D_\nu\Phi) \ , \end{aligned} \quad (2.22)$$

mentioning only C and P conserving operators, with Φ being the Higgs doublet field and D_μ being the covariant derivative. It is possible to express the EFT couplings in terms of the deviations from Eq. (2.20 [35]:

$$\begin{aligned} \frac{c_{\mathrm{W}}}{\Lambda^2} &\equiv \frac{2}{m_{\mathrm{Z}}^2}\Delta g_1^{\mathrm{Z}} \\ \frac{c_{\mathrm{B}}}{\Lambda^2} &\equiv \frac{2}{m_{\mathrm{W}}^2}\Delta k^\gamma - \frac{2}{m_{\mathrm{Z}}^2}\Delta g_1^{\mathrm{Z}} = \frac{2}{m_{\mathrm{Z}}^2}\left(\Delta k^\gamma - \Delta k^{\mathrm{Z}}\right) \\ \frac{c_{\mathrm{WWW}}}{\Lambda^2} &\equiv \frac{2}{3g^2m_{\mathrm{W}}^2}\lambda^{\gamma,\mathrm{Z}} \end{aligned} \quad (2.23)$$

Obviously the EFT introduces a constraint on those in order to keep only three independent parameters.

In general these anomalous couplings do not have to be physical. Being formulated within an EFT implies they can be an approximation for underlying new physics phenomena (BSM). The actual shape of the new physics phenomena would only become apparent at higher energy but at low energies is parametrised in the couplings, similar to the Fermi theory of beta decay and the full formulation of electroweak theory. Therefore the aTGCs can be used for setting limits on the validity of the SM.

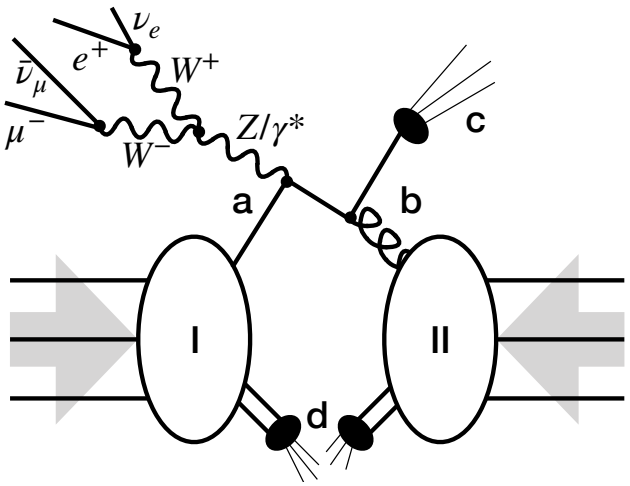

Figure 2.2: Schematic view of a proton-proton collision resulting in a W^+W^- event. The incoming protons **I** and **II** are represented by the three valence quarks drawn as three lines, while the bulge of sea quarks and gluon fields is shown as white ellipses. The hard scattering of a quark and antiquark is at **a**, where the antiquark is a result of initial state radiation (**b**). In this case, the initial state radiation is a gluon going to a quark antiquark pair. At **c** and **d** hadronisation processes are shown as black ellipses, while **d** is the underlying event. The thin lines coming from the black ellipses represent jets.

2.4 Hadron collisions and their results

Collider experiments provide an opportunity to test the predictions of the SM. While the experiment itself will be presented in Chapter 3, this section will focus on how the predictions are tested. Commonly this is done by measuring the cross section. The cross section σ is a measure for the probability that a process happens. It is defined as the area the particles need to hit such that the process occurs. In Figure 2.2 an example of a proton-proton collision leading to the production of two W bosons is sketched. Calculating the cross section of such an event is possible by calculating the probability of the initial state to go to the final state, given the couplings between particles described in the SM and taking into account their energies. However, at hadron colliders this is not straight forward, since hadrons are not elementary particles and therefore the initial state is not known.

2.4.1 The parton model

In Figure 2.2 the initial protons are drawn as three lines, indicating that a proton state is defined by two up and one down quark, the so called valence quarks. However, none of these might actually contribute to the shown interaction. In

fact, one of the initial state particles depicted in Figure 2.2 is a gluon.

The valence quarks are held together by gluon fields. The gluon fields can fluctuate into virtual quark-antiquark pairs by constant pair production and annihilation. These virtual quarks are the so-called sea quarks. At high energies the gluon fields and the sea quarks are carrying a significant fraction of the proton momentum.

At high energies the constituents of a proton become asymptotically free. This means one can regard them as independent particles, so called partons. Each parton carries a fraction x of the proton momentum p [37]:

$$x = \frac{p_{\text{parton}}}{p} \tag{2.24}$$

A parton can be any particle inside the proton, such as the valence and sea quarks, as well as the gluons.

In order to calculate a process like the one depicted in Figure 2.2 correctly, the x of the incoming partons need to be known. Since this is impossible using perturbative QCD, probability densities need to be fitted to experimental data. Figure 2.3 shows an example of the parton distribution function (PDF) for different types, like the valence quarks, gluons and sea quarks. The PDF is usually dependent on the energy scale μ^2:

$$\text{PDF} = \text{PDF}(x, \mu^2) \tag{2.25}$$

μ^2 is given by the sum of the four-momenta of the partons entering the scattering process and is therefore strongly related to the collision energy of the two protons. For energies around 13 TeV gluons carry most of the proton momentum. Thus gluon-gluon interactions are most likely.

At proton-proton collisions the initial states of the processes of interest have to be produced by breaking up the protons beforehand. The main interaction of two partons from different colliding protons is called the hard scattering. The remaining parts of the protons form the so-called underlying event.

2.4.2 Hadronisation

Particle collisions might result in final state quarks, but these cannot be directly detected. Bare quarks cannot exist because of colour confinement, which is why they undergo a hadronisation process.

From a theory perspective quark confinement makes it complicated to simulate events in which quarks are produced. Usually the process is split up into several steps after hard interaction. Afterwards, usually the so-called parton shower has

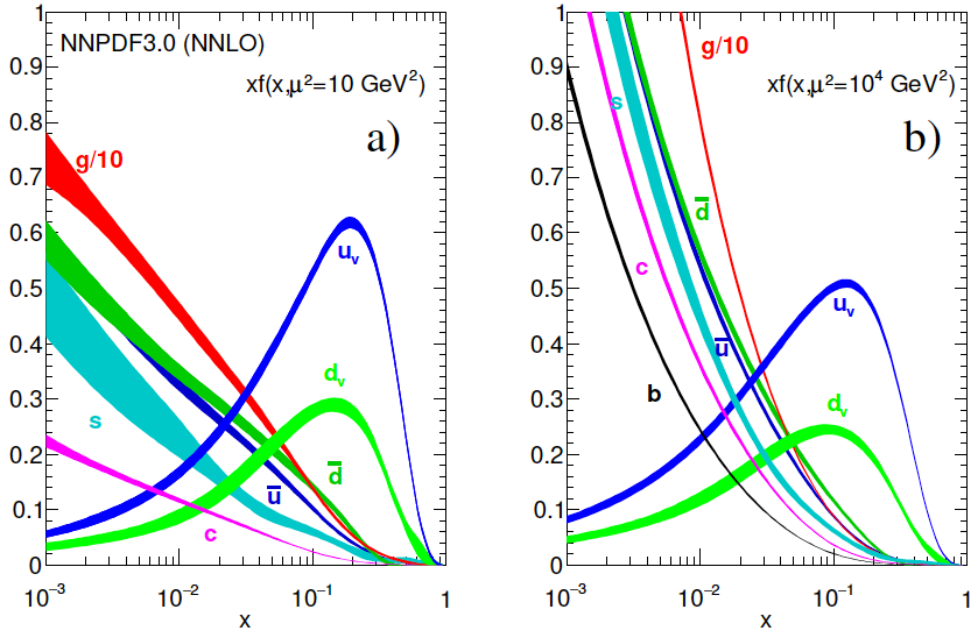

Figure 2.3: PDFs at two different energy scales μ^2 [38]. At low energy (a) the valence quarks carry most of the proton momentum. With higher energies the gluon fraction dominates more and more (b).

to be simulated, followed by the hadronisation. The latter one is the forming of actual final state particles visible in the detector. The parton shower is the intermediate step, connecting the hard scattering and the final hadrons with multiple QCD bremsstrahlung processes [39]. Due to the big gap between the hard scatter energy scale and the final state energy scale [40] a spray of accumulated particles is produced. Experimentally this is reconstructed as a so called jet using dedicated jet algorithms. Jet reconstruction is very important and algorithms are in general sensitive to QCD perturbation calculations [41]. Jets are further discussed in Chapter 4.

2.4.3 Predicting the cross section

The SM allows us to calculate the cross section, σ, of processes such as the one depicted in Figure 2.2. It sketches a proton-proton collision, resulting in the production of a W^+W^- pair. The W bosons decay further into a muon and a neutrino and an electron and a neutrino each, while also an underlying event is sketched.

In order to calculate the differential cross section of these kind of events, both the electroweak W^+W^- pair production as well as the underlying QCD processes have to be considered carefully. This process in particular is of special interest in Chapter 6, which is why it is used here as an example.

Matrix elements

Calculating a cross section means mapping incoming states $|i\rangle$ on final states $|f\rangle$. This is done by introducing a scattering matrix S. Thus, the probability to find a certain final state f in the incoming state i is given by the corresponding matrix element of S:

$$S_{fi} = \langle i|S|f\rangle \tag{2.26}$$

By taking only incoming states into account which actually change, one retrieves the scattering amplitude T_{fi} [30]. This is later in this thesis referred to as the matrix element $\mathcal{M}$ of a process. Because it gives the probability to retrieve a certain final state, it is directly linked to the (differential) cross section of the process:

$$\frac{\mathrm{d}\sigma}{\mathrm{d}\Omega} \propto |T_{fi}|^2 \ , \tag{2.27}$$

where $\mathrm{d}\Omega$ is the differential solid angle. One can say, predicting the cross section of a certain process is calculating the corresponding Feynman diagrams of the matrix element.

Precision of cross section predictions

Cross section results are usually calculated as an expansion in terms of coupling constants α, at hadron colliders usually the strong coupling constant α_s. The precision of a theoretical prediction usually is given in terms of the order of magnitude of the coupling constant. The leading order (LO) term of the calculation is the usually the born level (tree level) diagram, or the lowest order possible graph of a process. Processes of higher order thus are next-to-leading order (NLO), or even next-to-next-to-leading order (NNLO). Figure 2.4 shows the Feynman diagrams at LO contributing to the W^+W^- cross section. It consists of two main processes: A quark-induced cross section with two quarks being the incoming state and a gluon fusion process with two gluons as incoming state. While the quark process consists of two destructively interfering diagrams – a t- and a s-channel processes, with the latter containing a TGC graph – the gluon fusion process consists of a resonant Higgs production process and a non resonant "box diagram" process. Both of them are of higher order QCD, since both contain a quark loop and thus

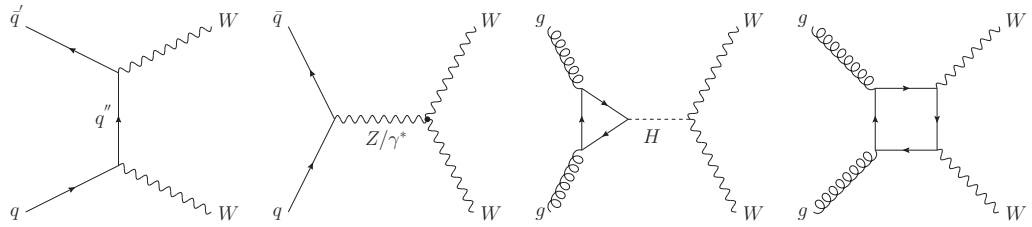

Figure 2.4: Feynman diagrams of contributions to the W^+W^- cross section. From left to right: The t-channel process, the s-channel process including the TGC vertex, the resonant gluon fusion process transmitted by Higgs production and the non-resonant gluon fusion process.

a higher number of vertices.

Besides of $\mathcal{O}(\alpha_s)$, the jet veto energy scale plays an important role in predicting cross sections. Usually measurements introduce cuts on the transverse jet momentum – a jet veto – in order to reduce processes resulting from top quark pair production. However, as the energy scale of the jet veto usually is different from the usual energy scale of W^+W^- production, which is around two times the mass of W boson, m_W. This means the cross section calculation receives larger contributions from leading logarithm (LL) that are usually neglected but need to be considered in this case in order to get accurate results [42]. In fact, theory predictions underestimated the measured cross section at $\sqrt{s} = 7$ TeV and 8 TeV [43, 44]. The gap could be closed by taking higher order QCD and perturbation theory into account [42, 45].

Figure 2.5 shows an example cross section prediction from Ref. [45] for two differential distributions at a centre of mass energy of $\sqrt{s} = 13$ TeV: The leading lepton transverse momentum p_T^{lead} and the polar angle difference of the two leptons $\Delta\phi_{\ell\ell}$. It is clearly visible, that the predicted cross section is very depended on the order of QCD: While the NLO prediction is slightly lower than the LO prediction, the NNLO is higher than the NLO. In general (differential) cross section predictions are now available for NNLO for $qq \to W^+W^-$ [45, 46] and NLO ($\mathcal{O}(\alpha_s^3)$) for $gg \to W^+W^-$ [47]. The interference between the resonant and non-resonant gluon fusion processes is known in LO. Also parton shower matched predictions of NNLO (NNLOPS) $qq \to W^+W^-$ are available [45, 48, 49].

Monte Carlo methods

Calculating the cross section including the PDFs, higher order perturbation theory matrix elements and parton showers analytically is impossible. This is done using Monte Carlo (MC) techniques, while the different steps such as the matrix element

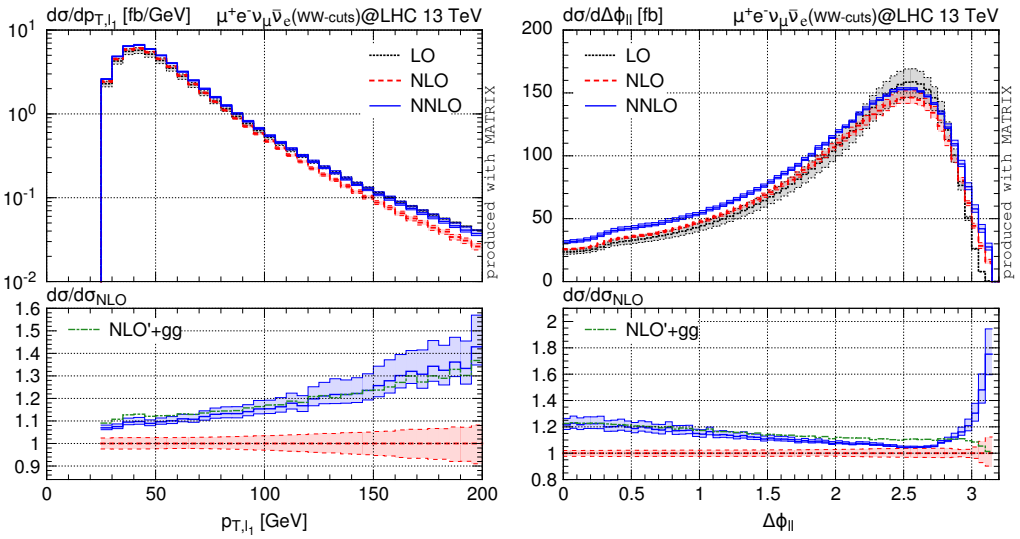

Figure 2.5: Differential cross section predictions of the leading lepton transverse momentum p_T^{lead} (left) and the polar angle difference of the two leptons $\Delta\phi_{\ell\ell}$ for $\sqrt{s} = 13$ TeV [45].

and the parton shower can be calculated independently. In addition it is possible to run a detector simulation on the resulting final state objects in order to get simulated data comparable with actual data taken at a collider experiment. In case of ATLAS (see next chapter), this is achieved by using the full GEANT4 simulation [50, 51]. The actual MC generator tools used for event generation or parton shower simulation is varying depending on the sample, they will be cited when needed in the corresponding chapters.

Chapter 3

The ATLAS detector at the Large Hadron Collider

The previous chapter gives some insight into how to obtain predictions from the SM for measurements at collider experiments. These predictions of course have to be verified experimentally at these kinds of experiments. Collisions of hadrons are provided by the Large Hadron Collider (LHC) at the Swiss-French boarder in Meyrin, Switzerland. The measurements in this thesis are based on collisions recorded using the ATLAS experiment which is situated at the LHC. Both of these technological facilities are to be discussed in this chapter.

3.1 The Large Hadron Collider

The LHC is a two-ring-superconducting hadron accelerator and collider [52] constructed within a 26.7 km tunnel near Geneva at the CERN laboratory. It replaced the previously installed Large Electron Positron Collider (LEP) which had been operated in the same tunnel from 1989 to 2000. At its four interaction points experiments are located, with the two biggest multipurpose experiments ATLAS [53] and CMS [54] being located at opposite sides of the ring, where ATLAS is located at Point 1 at the CERN site and CMS at Point 5. The other two main experiments are ALICE [55] which is dedicated to investigate heavy ion collisions, and LHCb [56], focusing on b-quark physics, located at Points 2 and 8, respectively. The numeration of interaction points stems from the eight interaction points of LEP. Further experiments are TOTEM [57], and LHCf [58], which are located as well at Points 1 and 5, respectively.

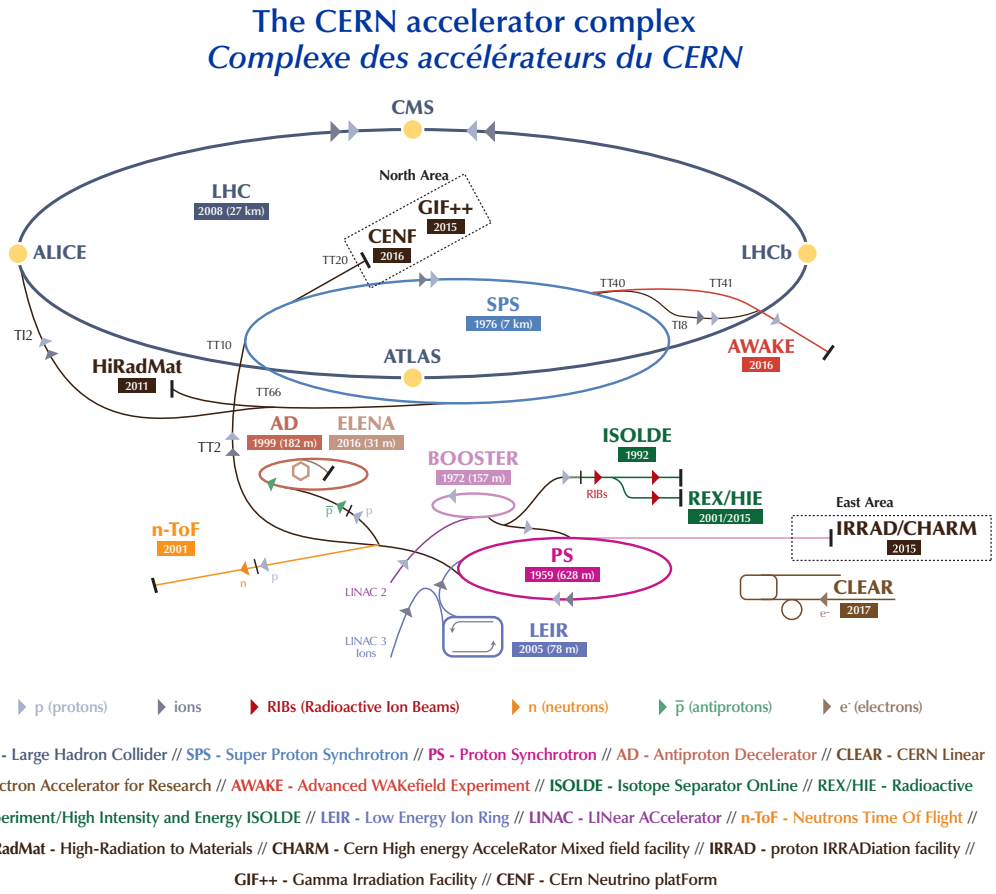

Figure 3.1: The CERN accelerator complex [59].

The path of a proton Figure 3.1 shows a graphical overview of the whole CERN accelerator complex. The LHC itself is bound into the complex of older accelerators, used as pre-accelerators. The starting point of the whole chain is a simple bottle of hydrogen. The hydrogen atoms are striped of their electrons using a duoplasmatron [60] and are then injected into Linac 2, a linear accelerator. After this step the protons have reached an energy of 50 MeV [61] and are injected into the Proton Synchrotron Booster (PSB), where they are accelerated up to 1.4 GeV [62]. Coming from the PSB, the protons then enter the Proton Synchrotron, a 628 m long synchrotron accelerator, where they gain an energy of up to 25 GeV [63]. After this, they are injected into the 7 km long Super Proton Synchrotron in order to gain 450 GeV, enough to be finally injected into the LHC [64]. For the peak energy of 7 TeV per beam a magnetic field of 8.33 T is needed to bend the charged particles into a circular orbit. This is achieved using super-conducting magnets,

cooled down to a temperature of only 1.9 K, making use of liquid helium [52]. The whole ring accommodates 1232 main dipole magnets. They are designed in a two-in-one design, containing both beam channels in a common cold mass and cryostat, and thus complying with the space limitation within the old LEP tunnel. The LHC also contains multiple quadrupole, sextupole and octopole magnets used for correcting and focusing the beam.

The beam is accelerated using a 400 MHz radio frequency (RF) system using niobium sputtered cavities. 16 of these cavities are operated, while each of them is driven by an individual klystron. Four of these system are stored together in one cryomodule, allowing them to work in a superconducting state [65]. Due to the nature of RF acceleration, the protons are spaced together in so-called bunches.

Centre of mass energy In each beam, protons are accelerated up to the same energy, resulting in a collision energy of twice the beam energy. Designed for colliding protons at a peak centre of mass energy of $\sqrt{s} = 14\,\text{TeV}$, the LHC was successfully operated at $\sqrt{s} = 7$ and 8 TeV during the LHC Run-1 from 2009 to 2012. Especially the year 2012 turned out to be a very successful year in its operation time, resulting in the discovery of the Higgs particle [5, 6]. During the LHC Run-2 from 2015 to 2018 the LHC was operated with a collision energy of 13 TeV.

Bunches and luminosity Protons are accelerated in bunches, containing about 1.1×10^{11} protons each. The distance of two bunches is 25 ns, resulting in a bunch crossing and thus also possible collisions every 25 ns. The number of events resulting from these collisions is

$$N_{\text{event}} = L\sigma_{\text{event}} \tag{3.1}$$

with L being the LHC luminosity, and σ_{event} the proton-proton cross section for a certain event. The luminosity is the amount of particle encounters per time and area and is a measure of the beam intensity. The L depends on beam parameters as well as on the number of bunches n_b and the number of protons per bunch N_b:

$$L \propto n_b N_b^2 \tag{3.2}$$

The LHC is designed to gain a peak luminosity of $L_0 = 10^{34}\ \text{cm}^{-2}\text{s}^{-1}$, while the highest peak luminosity recorded in ATLAS up to date was $1.9 \times 10^{34}\ \text{cm}^{-2}\text{s}^{-1}$ in May 2018 [66]. Usually more than one collision occurs per bunch crossing because of the large proton-proton interaction cross section. This is resulting in

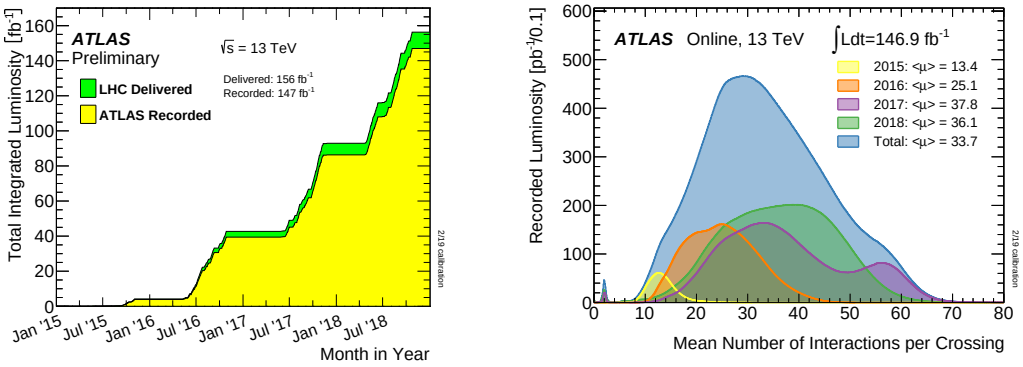

Figure 3.2: Integrated luminosity of LHC Run-2 vs. the time (left) and the recorded luminosity in ATLAS as a function of the mean number of interactions per bunch crossing, μ (right). Both graphics are taken from Ref. [67]. Over the time the instantaneous luminosity could be increased, resulting in higher average number of μ. The 2017 datasets has the highest average, due to some very high μ runs towards the end of that year (visible in a second peak in the corresponding distribution). ATLAS recorded a bit less than provided, due to data acquisition inefficiencies and delayed recording, as the inner detector systems are only switched on after the start of stable collisions.

overlapping so-called pile-up (PU) events which are in general not of interest. The right plot in 3.2 shows the recorded luminosity in ATLAS as a function of the mean number of interactions per bunch crossing*, μ. In average, the full Run-2 dataset had an average number of interactions of $\langle\mu\rangle = 33.7$, while the average increased over the years, due to a better understanding of LHC operation, which lead to a higher instantaneous luminosity.

In order to retrieve the total amount of events recorded during a span of time, a useful measure is the integrated luminosity, retrieved by integrating over the instantaneous luminosity L, which is a function of the time t:

$$L_{\text{int}} = \int_0^{T_{\text{run}}} L(t)\mathrm{d}t \quad , \tag{3.3}$$

with T_{run} being the length of the run. It can also be expressed as a function of the peak luminosity L_0 in the begin of the run:

$$L_{\text{int}} = L_0 \tau_L \left[1 - e^{-T_{\text{run}}/\tau_L}\right] \quad , \tag{3.4}$$

where τ_L is the luminosity lifetime [52]. This accounts for the fact, that during the time of run, the instantaneous luminosity decreases exponentially, similar to

*Not to be confused with the energy scale, μ^2, introduced in the previous chapter.

nuclear decay due to proton losses from the beam. Typical luminosity life times are $\tau_L = 14.9\ h$. The highest achievable total integrated luminosity per year is $80\,\text{fb}^{-1}$ to $120\,\text{fb}^{-1}$, depending on the average turnaround time of the machine [52]. The right plot in Figure 3.2 shows the recorded and provided integrated luminosity over the time of LHC Run-2. At the start of LHC Run-2, $4.2\,\text{fb}^{-1}$ was delivered in 2015, of which $3.9\,\text{fb}^{-1}$ was recorded by ATLAS. This was improved in the following years. In 2016 the LHC delivered $38.5\,\text{fb}^{-1}$ (recorded: $35.6\,\text{fb}^{-1}$), while in 2017 already $50.2\,\text{fb}^{-1}$ ($46.9\,\text{fb}^{-1}$) was delivered. In 2018, the last year of Run-2, $63.3\,\text{fb}^{-1}$ ($60.6\,\text{fb}^{-1}$) of collisions were provided [67].

3.2 The ATLAS detector

The ATLAS experiment is one of the two big LHC multipurpose detectors. It is designed symmetrically around the central interaction point, consisting of several sub-detector systems. These are layered around each other like the layers of an onion: The inner detector (ID) – the electromagnetic calorimeter (EM calorimeter) – the hadronic calorimeter – the muon spectrometer. For momentum measurements of charged particles, ATLAS also has two main magnetic systems, a central solenoid and an outer toroid. The full detector is divided into three main parts, the central barrel and two end-caps. For illustration, Figure 3.3 shows a computer-generated picture of the full detector, showing all subsystems, which will be discussed in more detail in the following sections. If not stated otherwise, the main source of information for this chapter is the technical ATLAS design report from 2008 [53]. The whole detector is about 44 m long and 25 m high, taking most of the space of the cavern it is located in.

The ATLAS coordinate system The ATLAS detector itself marks the laboratory rest frame throughout the rest of this thesis, hence its coordinate system nomenclature is introduced here. The nominal interaction point is defined as the origin of the coordinate system [53]. The proton beam direction defines the z-axis. Looking towards the centre of the LHC ring, the right side (side-A) defines the positive direction of z. The positive x-axis is pointing towards the centre of the LHC, while the y-axis is pointing upwards. Usually spheric-like coordinates are used. The azimuthal angle ϕ is measured around the beam axis. The pseudo-rapidity η is related to the polar angle θ (the angle from the z-axis) by

$$\eta = -\ln\tan\frac{\theta}{2} \tag{3.5}$$

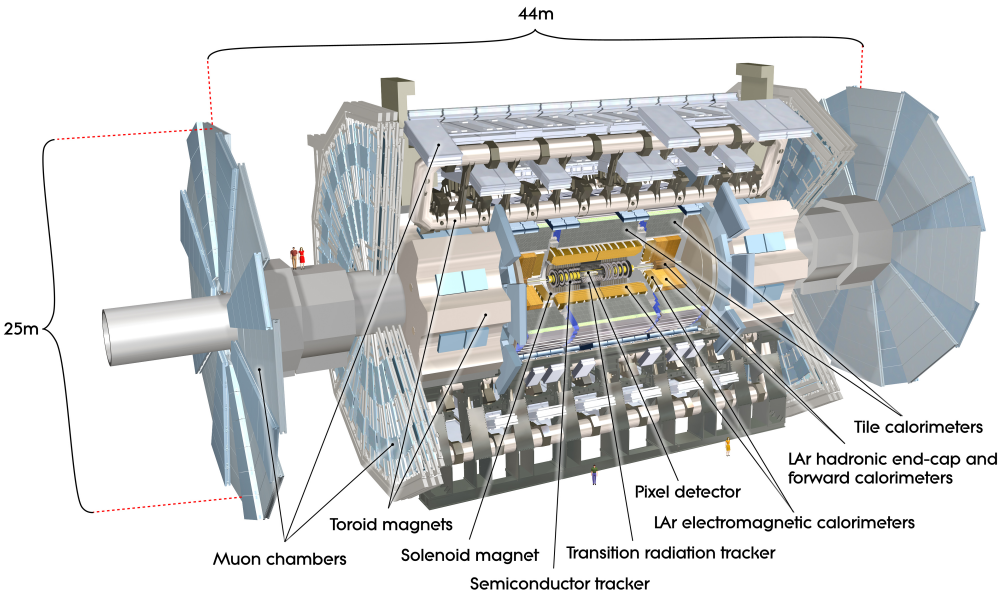

Figure 3.3: Computer generated picture of the full ATLAS detector (taken from Ref. [68]). All the main components – sub-detectors and magnetic systems – are labeled within the picture.

For $m \ll E$ this is a very good approximation of the rapidity

$$y = -\frac{1}{2} \ln \left(\frac{E + p_z}{E - p_z} \right) \quad . \tag{3.6}$$

Differences in η are Lorentz invariant, also particle production is roughly constant as a function of η [30]. Thus, the pseudo-rapidity is much more commonly used compared to the polar angle.

Usually one measures the transversal components of energy and momentum E_T and p_T, defined in the x-y-plane. This is due to the unknown z-components of the initial states. The missing transverse energy E_T^{miss} is the vectorial sum of non measured transverse energy, e.g. neutrinos escaping the detector undetected.

Distances are calculated in the pseudo-rapidity-azimuthal angle space, defined by the dimensionless distance parameter

$$\Delta R = \sqrt{\Delta\eta^2 + \Delta\phi^2} \quad . \tag{3.7}$$

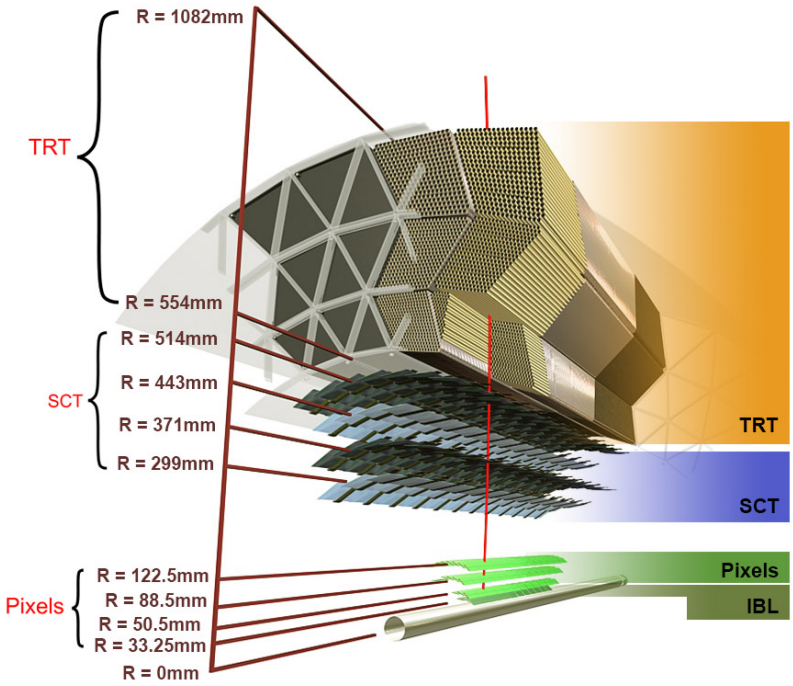

Figure 3.4: The ATLAS inner detector (taken from Ref. [69]). Shown are the main components, pixel tracker – SCT – TRT, as well as the distances from the beam.

3.2.1 The inner detector

The ID is the main tracking device of ATLAS [53]. It consists of three independent detector systems. Figure 3.4 shows a schematic sketch of the ID. All the ID technology is fitted within a cylindrical envelope, having a total length of roughly 7 m and a radius of 1.15 m. The ID covers a pseudo-rapidity range of $|\eta| < 2.5$. Besides good spacial resolution for a precise momentum measurement, requirements to the ID are good resolution of primary vertex reconstruction and separating PU interactions. Primary vertices are defined as the points in space where proton-proton interactions have occurred [70]. The average number of reconstructed vertices can go up to 70 in 2018 data. Thus a spatial resolution of the z coordinate with $\sigma(z) < 1\,\text{mm}$ is necessary. The shortest distance of a track to the z-axis the transverse plane is the so-called impact parameter d_0. The subsystems provide a spatial resolution of d_0 of $10\,\mu\text{m}$.

The pixel tracker Since Run-2, the innermost layer of the ID consists of the inner B-Layer (IBL), which is part of the pixel tracker [69, 71, 72]. The pixel detector is build up from 4 layers in the barrel and three disks in each end-cap. The typical pixel size of the original outer three pixel layers is $50\,\mu\text{m} \times 400\,\mu\text{m}$ with

a thickness of 250 μm. The IBL adds 12 million additional pixels with a typical size 50 μm $\times$ 250 μm to the 80 million previous pixels. The intrinsic accuracies in the barrel are 10 μm $(R-\phi)$ and 115 μm (z) and in the disks are 10 μm $(R-\phi)$ and 115 μm (R) [53].

The silicon microstrip detector The silicon strip detector (SCT) adds 4 additional cylindrical layers in the barrel and nine discs in each end-cap to the inner tracker. It completes the semiconductor based tracking technology using. Each of the layers actually consists of two layers of micro-strips, such that $R-\phi$ coordinates can be measured. In the barrel the one set of strips is parallel to the beam axis, while in the end-cap one set of strips runs radially. Every single strip is about 6.4 cm long, having a strip-width of 80 μm. The intrinsic accuracies per module in the barrel are 17 μm $(R-\phi))$ and 580 μm (z) and in the disks are 17 μm $(R-\phi))$ and 580 μm $(R))$ [53]. The SCT adds 6.3 million read out channels to the more than 80 million channels of the pixel detector.

The transition radiation tracker In addition to the silicon-based trackers a third layer of a straw-tube detector is added to the ID. The transition radiation tracker (TRT) adds a large number of hits per track to the event, about 36 per track. The TRT enables tracking up to $|\eta| = 2.0$, with an accuracy of about 130 μm for each of the 4 mm straws. It only provides $R-\phi$ information, with the 140 cm long straw tubes being parallel to the beam axis in the barrel. The number of readout channels is about 351000. In addition to its tracking capacities, it provides information useful for electron identification by reading out the transition radiation from the xenon based gas mixture in the tubes. Due to gas leaks, in some parts of the detector, the gas was replaced by a cheaper argon based mixture in some channels, reducing the identification performance in these regions [73].

The solenoid magnet The whole ID is embedded in a 2 T solenoidal field, provided by a 2.3 m in diameter and 5.3 m long solenoid [74]. It uses an indirectly cooled aluminium-stabilised superconductor, cooled down to 4.5 K. It allows, together with the precise tracking instruments, a wide range of momentum measurements, from 0.5 up to 150 GeV.

3.2.2 The calorimetric systems

Directly outside the inner solenoid, calorimetric measurements take place. The calorimetric system covers a range of $|\eta| < 4.9$. Inside the central regions the focus lays on fine granularity for precision measurements. The outer regions have

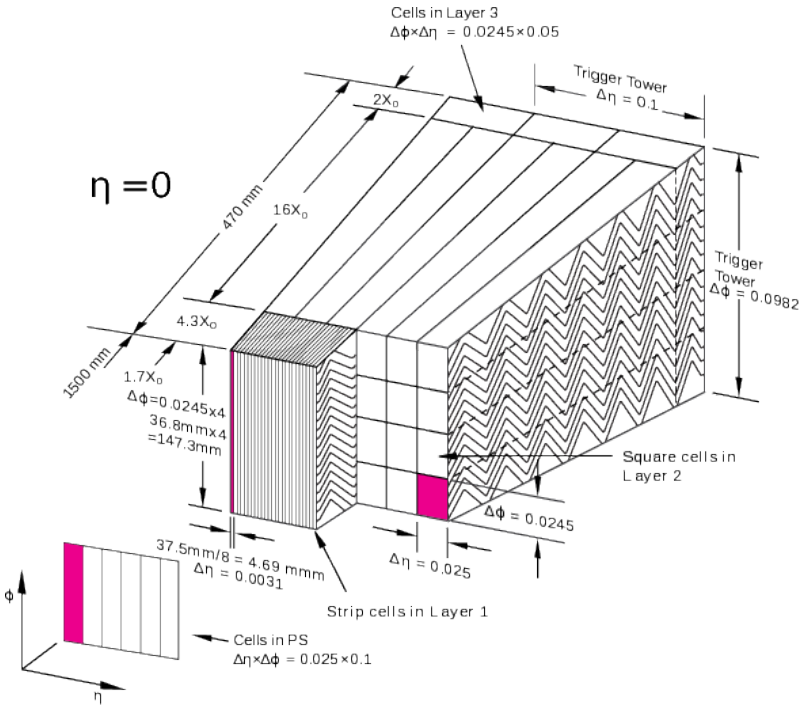

Figure 3.5: Sketch of a barrel module of the ATLAS LAr EM calorimeter [75]. Clearly visible are the three main layers divided into cells of different granularity. The pre-sampler shown as "PS". Beside of measures in millimetres, the depth of the calorimeter cells is also shown in radiation lengths X_0. The combination of more cells into trigger towers is illustrated.

a coarser coverage, but are still sufficient for jet reconstruction and E_T^{miss} measurements, with the focus on being radiation hard. The so-called transition region between the barrel end the end-cap detectors is filled with cables and services for the inner detector as well as power supplies and services for the barrel liquid-argon calorimeter [53].

The electromagnetic calorimeter The EM calorimeter is made up of a main barrel part ($|\eta| < 1.475$) and two end-cap parts ($1.375 < |\eta| < 3.2$). Its purpose is the calorimetry of electrons and photons. They result in electromagnetic showers in the accordion shaped lead-liquid argon structure. The lead is used as an absorber while the liquid argon (LAr) is ionised by shower electrons, with the ionisation read out by copper electrodes. For $|\eta| < 2.5$ the calorimeter is segmented into three layers, which can be seen in more detail in Figure 3.5. The different layers have different granularities in $\Delta\eta \times \Delta\phi$: $0.025/8 \times 0.1$ in the first layer, 0.025×0.025 in the second and 0.050×0.025 in the third. The exact granularity can differ in some η regions, and is listed in Table 1.3 of Ref. [53]. The design goal of these

layers is tracing the shower shape as accurately as possible, while the first layer needs high ϕ resolution for being able to rule out π^0 conversions. The third layer is needed to measure the depth of the shower.

For $|\eta| > 2.5$ the EM calorimeter is segmented in only two layers, having a granularity of $\Delta\eta \times \Delta\phi = 0.1 \times 0.1$. In the region of $|\eta| < 1.8$ an active 1.1 cm thick LAr layer is build before the main EM calorimeter, the pre-sampler. It is used to correct for lost energy of electrons and photons upstream the EM calorimeter. The total thickness of the EM calorimeter is more then 22 radiation lengths (X_0) in the barrel and more than 24 X_0 in the end-caps [53]. X_0 depends on the characteristics of the material: Z, the atomic number and A, the weight of the material. Starting from the inner radius $R = 1.5\,\text{m}$, the EM calorimeter has a total thickness of 0.47 m in the barrel. The EM calorimeter has about 173000 readout channels in total.

The uncertainty of the determined energy E is given by [76], adding the error terms in quadrature:

$$\left(\frac{\sigma(E)}{E}\right)^2 = \left(\frac{a}{\sqrt{E}}\right)^2 + \left(\frac{b}{E}\right)^2 + c^2 \quad . \tag{3.8}$$

The stochastic term a is determined to be $10\% \cdot \sqrt{E}$, while the constant term c is 17%. The noise term b is found to be linear, not exceeding $0.7\% \cdot E$ [53].

The hadronic calorimeter The ATLAS hadronic calorimeter is placed directly behind the EM calorimeter. In fact it consists of three different types of calorimeters, depending on the relative position inside of ATLAS. The tile calorimeter is to be found inside the (extended) barrel region covering $|\eta| < 1.0$ ($0.8 < |\eta| < 1.7$), while the LAr hadronic end-cap calorimeter (HEC) covers the region $1.5 < |\eta| < 3.2$. In addition there is a LAr forward calorimeter (FCal) covering the $|\eta|$ range of 3.1 up to 4.9. The tile and the FCal each have three layers, while the HEC has 4. The granularity of the tile and end-cap calorimeter is about 0.1×0.1 in $\Delta\eta \times \Delta\phi$., while it is $3.0 \times 2.6\,\text{cm}$in for $\Delta x \times \Delta y$ in the forward system. These values can differ in η, the exact listing is again to be found in table 1.3 in Ref. [53]. The tile calorimeter uses steel as the absorber and scintillating tiles as the active material. In the HEC and FCal copper plates are used for absorbing (tungsten in the last two layers of the FCal), end LAr as active material. The inner radius of the tile calorimeter is $R = 2.28\,\text{m}$. It exceeds to an outer radius of 4.25 m. The full hadronic calorimeter system has in total more than 19000 read out channels. Regarding Eq. (3.8), the combined performance of the tile and LAr calorimeters is found to have $a = (52.0 \pm 1.0)\% \cdot \sqrt{\text{GeV}}$, $b = 1.6\text{GeV} \pm 0.1\%$ and $c = (3.0 \pm 0.1)\%$ [53].

3.2.3 The muon spectrometer

Muons usually do not shower inside the calorimetric systems and only leave ionisation traces, due to their high mass. Therefore an additional spectroscopic system is needed, muon chambers, build around the rest of the previously described components. For precise momentum measurement an additional magnetic field from a toroid magnet is used.

Muon chambers As the other sub detector systems, the muon system is divided in three parts, the barrel and two end-caps ("muon wheels"). In the barrel ($|\eta| < 2.7$) it consists of three layers of monitored drift tubes (MDT) at radii of 5 m, 7.5 m, and 10 m. MDT are also used in the wheels, however for $2.0 < |\eta| < 2.7$ cathode strip chambers (CSC) are used in the innermost layer, since they provide higher granularity in this region of higher expected background rates. The distance of the four wheels in the end-cap from the interaction point are about 7.4 m, 10.8 m, 14 m, and 21.5 m.

The muon detector system comes with its own trigger system, covering $|\eta| < 2.4$. Therefore resistive plate chambers are used in the barrel ($|\eta| < 1.05$) and Thin gap chambers in the wheels ($1.05 < |\eta| < 2.7$). Beside serving as hardware trigger these detectors also provide a second coordinate to the MDT. The muon system has more than one million read out channels. The overall resolution of the MDT is about 35 μm in the z coordinate the CSC provide 40 μm accuracy in R. The ϕ resolution is in general better than 10 mm.

The toroid magnet The magnetic field is provided by superconducting air-core toroid magnets, providing a field of $0.5 - 1$ T. The system consists of one big barrel toroid with a length of about 25.3 m and two smaller end-cap toroids with a length of 5 m. Each of the toroids is made up from 8 coils, while the end-cap toroids are rotated by 22.5° with respect to the central toroid, in order to provide an optimal overlap between the single magnetic fields.

3.2.4 The trigger

From a 25 ns bunch-crossing one can assume a maximal event rate of 40 MHz. This is way too much to be processed, reconstructed and stored. Therefore a sophisticated trigger system is needed, in order to reduce the event rate to approximately 1 kHz to be written on disk, but at the same time keep high efficiencies on rare or new physics events [77]. For Run-2 the ATLAS trigger system was updated to a two-level trigger. An overview over this system can be seen in Fig-

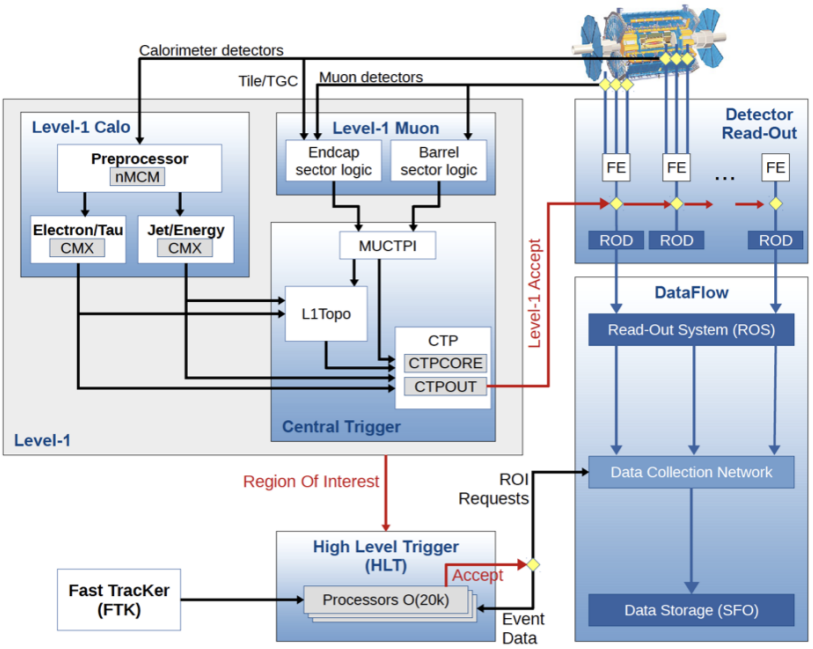

Figure 3.6: Overview over the ATLAS Run-2 trigger system [78]. The main components are the hardware based level-1 trigger (L1) (grey box), deciding based on hardware information. If it accepts, events are processed by the HLT. If both levels are passed, data is written out.

ure 3.6. The hardware based level-1 trigger (L1) takes input from the previously mentioned muon system trigger modules (L1Muon) and from coarse granularity calorimeter information (L1Calo) [79]. An additional new system is the topological trigger (L1Topo), selecting based on geometric or kinematic information received from L1Calo or L1Muon. This was commissioned in 2017. By defined regions-of-interest it reduces the event rate coming from the LHC to approximately 100 kHz with a decision time of 2.5 μs. The trigger decision is formed by the central trigger processor.

Events passing the L1 are input to the software based high level trigger (HLT). It consists of a large computing farm of about 40000 cores. It uses reconstruction algorithms, going into full reconstruction if necessary. It provides about 2500 independent trigger chains, triggering on single objects like electrons, τ leptons, or jets, up to full event topologies like the decay chain of a Higgs boson. The HLT decides within 300 ms with an output rate of 1 kHz. The full configuration of the L1 and HLT decision making process is called trigger menu.

The electron selection uses a likelihood-based identification, whereas photon identification relies only on cuts applied on variables [79]. The trigger identifica-

tion efficiency for these two objects reaches up to 100% after steep turn-on regions as a function of transverse momentum [79].

Chapter 4

Reconstruction and identification of particles

Particles cannot be observed directly, they need to be reconstructed from their combination of signals inside the detector.

4.1 Overview

In general, the reconstruction results from the combination of the signals they leave inside the sub-detector systems. Electrons mainly interact electromagnetically, they cause so-called hits within the ID tracking detectors and leave energy deposits inside the EM calorimeter. Photons as transmitters of the electromagnetic force also leave energy deposits inside the EM calorimeter, however leave no signals in the ID since they carry no charge, as long as they do not interact in the ID, forming electron-positron pairs. Muons stemming from a primary vertex can be distinguished from electrons since they hardly deposit any energy in the EM calorimeter, but instead propagate through the whole detector and leave signals in the ID as well as in the muon tracking chambers outside the calorimetric systems. Hadrons deposit the majority of their energy inside the hadronic calorimeter and in case they are charged, they also leave signals in the ID. Neutrinos interact only weakly and therefore are generally not detected, thus they can only be reconstructed indirectly by missing transverse energy. Figure 4.1 shows a sketch of these basic principles.

Single hadrons like protons, pions or kaons are used only in specific analysis, usually they are only considered as constituents of jets which are reconstructed from energy deposits as described below in Sec. 4.3. Therefore speaking of hadronic particles is usually referring to jets, since they point to an underlying

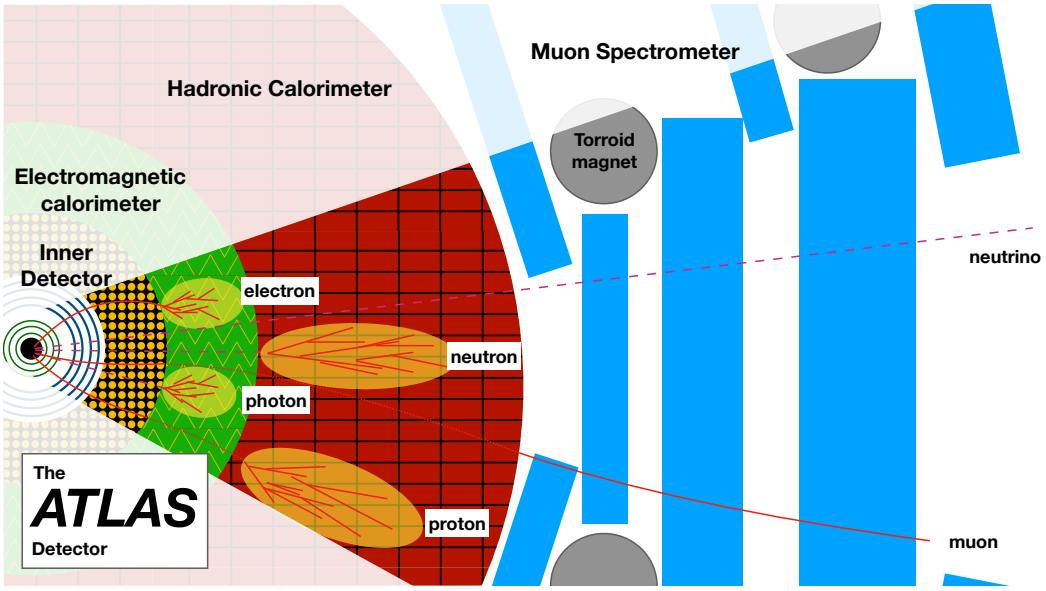

Figure 4.1: Particle identification in ATLAS. Shown are the basic components of the ATLAS detector and their role in particle detection. The inner detector is shown in green and blue circles representing the pixel and the silicon strip detectors, respectively, as well as a black area with yellow dots representing the TRT. The EM calorimeter is shown in green and the hadronic calorimeter in red. The muon chambers are represented by blue boxes. Particle Tracks are shown as red lines, showers in the calorimeters are underlined by yellow ellipses. Invisible particles are represented by purple dashed lines.

quark or gluon final state.

The reconstruction of objects like jets or electrons usually takes a lot measured information from the same tracking and calorimetric systems into account. In many cases it is not possible to unambiguously tell what the incident particle causing the signals was. In order to decrease this ambiguity and to improve the purity of the reconstructed objects, identification criteria are applied on top of the reconstruction. Therefore it is crucial to measure these efficiencies as precisely as possible, as their inverse is used in the calculation of detector independent cross sections.

Reconstruction, identification and the respective performance measurements are undertaken within specialised performance working groups within the ATLAS collaboration and are presented briefly in the following sections.

4.2 Lepton and photon reconstruction

4.2.1 Electrons and photons

Electrons and photons both produce similar electromagnetic showers inside the EM calorimeter. Therefore reconstruction of both kinds of objects is happening in parallel, starting from their EM calorimeter signature. In Run-2, two reconstruction algorithms are used. The seed-cluster reconstruction described in Ref. [1] was inherited from Run-1, and was the default algorithm until the end of 2016. The same algorithm is applied to photons [80]. It is used for the measurement described in Chapter 6. The super-cluster reconstruction replaced the previous seed-cluster reconstruction in 2017 for photons and electrons [2]. It is used in Chapter 5.

Seed-cluster reconstruction Clusters are build around cluster seeds, which are found using a sliding window algorithm. The window has a fixed size of 3×5 units of the EM calorimeter middle layer cell size. If a seed has more than 2.5 GeV of transverse energy in total within all three layers, clusters are build using a cluster algorithm [81]. Tracks are reconstructed in parallel from hits in the tracking detectors using the ATLAS Global χ^2 Track Fitter [82]. To account for energy losses due to bremsstrahlung a subsequent fitting procedure using a Gaussian Sum Filter method [83] is performed. Tracks are finally matched to seed clusters [1]. In case no matching track can be found, the cluster is taken to be a photon candidate. Matched track cluster candidates failing certain criteria such as the number of hits in the silicon detector are also considered photon candidates and therefore be an ambiguous candidate. The reason behind this is, that photons can convert into electron-positron pairs before reaching the calorimeter. If the cluster can be matched to a track, an electron candidate has been reconstructed.

Super-cluster reconstruction While the seed-cluster algorithm uses fixed sized calorimeter cell clusters as a basis, the super-cluster algorithm is using variable cluster sizes. This has the advantage of dynamically taking into account photons from bremsstrahlung or electron pairs from conversions within one supercluster. The new algorithm prepares topo-clusters as they are also used in jet reconstruction. Tracks in the ID are fitted as in the old algorithm, as well as possible photon conversion vertices. From tracks and topo-clusters the super clusters are build separately for photons and electrons. They are calibrated and finally tracks or conversion vertices are matched. After this step an ambiguity comparison takes place between photon and electron super clusters. This can result in ambiguous

photon and electron candidates, reconstructed from the same object.

After the reconstruction step, the identification step is performed by applying further quality criteria [2]. This step increases the purity of the selected electron and photon candidate sample and is crucial for rejecting other particles like hadrons or in the electron case from converted photons [1]. Identification working points are usually *Loose*, *Medium* and *Tight*, depending on how strict the applied criteria are. The electron identification procedure is based on a likelihood approach which will be described in more detail in the next chapter. Photon identification uses a cut based approach based on shower shapes and properties in the calorimeter [80]. In addition, the *Tight* identification selection makes use of a multivariate analysis approach [2].

4.2.2 Muons

Muon candidates are reconstructed by combining a track in the ID with a track in the muon spectrometer [84]. Tracks in the ID are constructed using the same method as in the electron case mentioned in the previous Section 4.2.1. Muon spectrometer tracks are found using a Hough transform algorithm [85] and fitted using a χ^2 fit. The matching of inner and outer tracks depends on the information available from the tracking and calorimeter detectors, described in more detail in Ref. [84]. Further identification is necessary to suppress muons from pion and kaon decays. It is based on the difference of measured properties like the transverse momentum in the ID and the muon spectrometer, the number of hits in the tracking devices and the χ^2 of the fit [84]. This results in four working points *Loose*, *Medium*, *Tight* and *High-p_T*, where the ATLAS default is the *Medium* working point.

4.2.3 τ leptons

τ leptons decay into lighter leptons or result in jets, thus their reconstruction is based on the reconstruction of these particles. Reconstruction and identification measurements are performed for these heavy leptons in ATLAS [86], however they are not further considered within this thesis.

4.3 Jet reconstruction

Jets are used to gain information about the underlying final state quark or gluon [87]. The basic principle of any jet algorithm is combining the calorimetric and tracking information in order to find a combined momentum of the particle spray which represents the underlying quark or gluon.

4.3.1 Jet algorithm and jet calibration

The anti-k_t algorithm In ATLAS the default jet algorithm is the anti-k_t algorithm* [89] with radius parameter $R = 0.4$. It is a sequential recombination algorithm, meaning it is based on pair-wise clustering particle momenta recursively. In more detail, the following d-values based on the transverse momenta $p_{T,i}$ and $p_{T,j}$ of two particles i and j, respectively, are calculated [90]:

$$d_{ij} = \min(p_{T,i}^{-2}, p_{T,j}^{-2}) \frac{(\Delta R_{ij})^2}{R} \tag{4.1}$$

$$d_{iB} = p_{T,i}^{-2} \tag{4.2}$$

ΔR_{ij} is the distance between two particles i and j. It is calculated as in Eq. (3.7):

$$(\Delta R_{ij})^2 = (\eta_i - \eta_j)^2 + (\phi_i - \phi_j)^2 \tag{4.3}$$

A list of all these d values is made. If the smallest value is a d_{ij} the i and j transverse momenta is combined and the list is remade. If the smallest value is a d_{iB}, i is considered as a complete jet and is removed from the list. In principle d_{iB} is a measure of distance between a particle i and the beam, while d_{ij} is a distance measure of the two objects i and j

The anti-k_t algorithm has the advantage that it has meaningful theoretical properties. The actual code for reconstruction is implemented into the ATLAS software† using the FastJet package [91].

Inputs to the jet algorithm The input for the jet algorithm are topologically connected calorimeter cell clusters in the hadronic calorimeter and EM calorimeter. These so-called topo-clusters are build from calorimeter cell signals, exploring the

*The name refers to the k_t algorithm [88]. k_t refers to the transverse momentum p_T, most interestingly this notation is not used in Ref. [88].

†Jet reconstruction techniques used in this thesis are very much automated and not implemented by the author.

three dimensional distribution and connecting neighbour cells in order to reconstruct energy and directions of the incoming particles, while disregarding cells below a certain threshold as noise [92]. Tracks are reconstructed using a series of various algorithms and a machine learning approach making use of neural networks [93, 94]. Properties of topo-clusters as well as tracks were compared with simulation, showing in general good agreement in most cases [95]. Track information is used to distinguish hard scatter from PU jets as described below.

Calibration Since the reconstructed jet four-momenta still can differ between data and simulation the latter needs to be calibrated to data. In addition also measured jet properties need to be understood well, as for example the performance of energy response in the detector. Therefore p_T and η dependent correction factors on the energy scale are calculated from data and MC and are applied to the MC simulation to correct the energy scale and the resolution [96]. This includes global corrections for MC and data, using p_T sensitive observables for improving energy and direction resolution. In-situ corrections for data are calculated using events with two jets (di-jets) for comparing central jets with respect to forward jets. In addition, correction factors can be obtained by using events with events were jets are recoiling against reference Z bosons or photons decaying into leptons.

Jet reconstruction is significantly influenced by PU, leading to a constant overlap of soft particles on hard scattering events. In this context, PU refers to the fact that during an LHC bunch crossing multiple interactions occur, usually one hard-scatter event of interest and several low-energy so-called minimum-bias interactions. This is why a subtraction technique based on an energy flow estimation inside the area of the jet candidates is employed [97]. In addition to removing the contribution of PU particles from hard-scatter jets, also PU jets need to be identified and removed when the physics measurements targets the hard-scatter event only. The PU jets stem from different interaction vertices and they can be separated using the jet-vertex-tagger technique [98] when the jets lie within the acceptance of the tracking detector. Outside the tracking acceptance a similar technique is applied, however making use only of calorimetric information [99].

4.3.2 b-jets

Jets originating from the fragmentation of b-quarks, so-called b-jets, are of special interest for many analysis. For the W^+W^- analysis presented in Chapter 6 they are of interest, because they are part of the top quark signature, and top quark production presents one of the largest backgrounds in this analysis. b-jets can be identified with so-called b-tagging algorithms. These are based on multivariate

analysis (MVA) techniques making use of boosted decision trees (BDTs). Inputs for this MV2c10 BDT algorithm are outputs from other algorithms based on the impact parameter, secondary vertices and the full decay chain of b-hadrons [100, 101]. The algorithm's operating point used for the measurement presented in this thesis has an efficiency of 85% for selecting b-jets.

4.4 Missing transverse energy computation

Within ATLAS it is not impossible to detect single neutrino momenta, since they do not leave any electronic signals in the detector. However it is possible to measure the vectorial sum of their transverse momentum stemming from a primary vertex by estimating the missing transverse energy E_T^{miss} . Because of E_T^{miss} is referring to massless neutrinos, it is synonymously called missing transverse momentum. It computed as the negative of the vectorial sum of the visible transverse momenta. In this sense the visible transverse momenta are momenta from tracks associated with jets, muons, electrons as well as tracks which are not linked to a reconstructed object [102]. For electrons the calibrated p_Ts measured using calorimeter information is used since this is more precise than the measurement using tracking information [103]. Taking only track information into account, makes this variable PU robust and takes advantage of the excellent vertex resolution of the ID [103]. Track momenta can be easily assigned to a primary vertex. However, the track based missing transverse momentum E_T^{miss} ($E_T^{\text{miss,track}}$) is limited then to the smaller ID coverage of $|\eta| < 2.5$ and cannot take neutral particles like neutrons into account, since they leave no tracks in the ID.

Another variant of E_T^{miss} calculation only takes calorimetric information into account, however is not further used in this thesis.

4.5 Overlap removal

The signals caused by one particle can pass simultaneously the reconstruction criteria of different physics objects. For example both, electron and jet reconstruction are based on calorimeter clusters. This makes an overlap removal indispensable, the recommended procedure is the following [104, 105].

- If an electron and a muon candidate share the same reconstructed track, the electron candidate is disregarded.
- Jet candidates are removed if they are within a cone of size $\Delta R = 0.2$ around an electron candidate or an muon candidate. The muon case only applies if

the jet candidate has fewer than three associated tracks.

- Muon candidates are disregarded when a jet candidate with three or more tracks is reconstructed around them within a cone of size $\Delta R = 0.4$.
- Electron candidates are ignored when jets are within a region of $0.2 < \Delta R < 0.4$ around them.

Chapter 5

Measurement of electron identification efficiencies

Electron identification describes the application of additional criteria on top of the reconstruction to further distinguish real electrons from photons or hadrons that can also be reconstructed as electron candidates. The first section describes how the likelihood is constructed that is used as identification criterion. The question of how efficiently one can identify electrons using this criterion will be discussed in the second section. The third section describes a measurement of electron identification efficiencies which was undertaken as a part of this thesis project. Its results are presented in in Section 5.4. The method is summarised in the last Section 5.5.

Parts of my work resulted in contributions to two publications on electron identification [1, 2], however, the presented results in this chapter result from an updated method which is not published yet.

5.1 Identification of electrons

Electrons are identified using a likelihood approach based on their signature in the calorimeters and tracking detectors [1, 2]. The most useful variables for identification are based on shower shapes.

The likelihood (LLH) L of an electron candidate to be signal (S) or background (B), can be calculated by the product of various probability density functions (Pdf) P_i:

$$L_{S/B}(x) = \prod_{i=1}^{n} P_{S/B,i}(x_i) \tag{5.1}$$

The Pdfs are encoding the probability of a candidate to be an electron based on a specific shower shape variable. Signal in this context means, that the electron

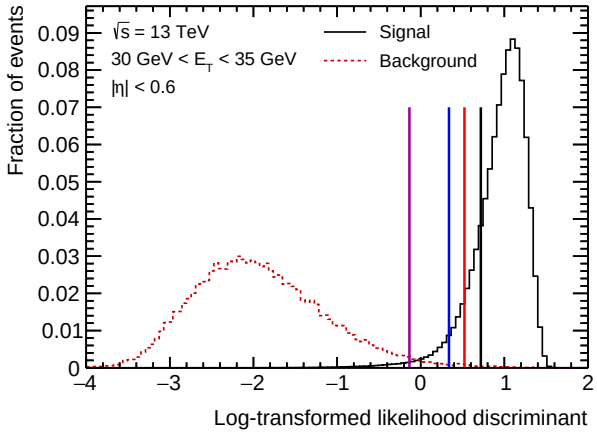

Figure 5.1: The transformed electron identification likelihood discriminant as discussed in the text. Signal from MC *Zee*, background is generic two-to-two process simulation sample. The four horizontal lines show the respective thresholds for *Very Loose*, *Loose*, *Medium* and *Tight* identification (from left to right). The shown plot is taken from [1] and was slightly modified.

is actually an electron, while background can for example be a misidentified jet. From the respective signal and background likelihoods one can construct then a discriminant d_L for every electron candidate

$$d_L = \frac{L_S}{L_S + L_B} \tag{5.2}$$

Since this discriminant peaks sharply at 1 for signal and 0 for background, which makes it inconvenient to select operating points, one transforms this discriminant using an inverse sigmoid function:

$$d'_L = -\tau^{-1} \ln \left(d_L^{-1} - 1 \right) \tag{5.3}$$

Figure 5.1 shows an example of the log-transformed discriminant d'_L. Signal and background can be separated easily by eye. Pdfs used as input for the signal and background likelihoods $L_{S,B}$ use quantities gained from the calorimeters, the trackers and consider in addition the quality of the track-cluster-matching.

From the hadronic calorimeter one can retrieve the variables R_{had} and R_{had1}, which are ratios of the E_T measured in the hadronic calorimeter and the E_T from the EM cluster. The EM calorimeter provides several Pdfs originating from the three calorimeter layers, like shower widths or ratios of the energy deposit in one layer compared to the total EM cluster.

One of the track parameters used in the identification of electrons is the significance of the transverse impact parameter $d_0/\sigma(d_0)$. The transverse impact parameter d_0 is defined as the shortest distance of a track to the proton beam. Also the transition radiation of the TRT is used to reject light flavour jet background. Light flavour refers gluons and *u*-, *d*-, or *s*-quarks. The number of hits within one of the trackers is used as further rejection variables, however as direct cuts and without building Pdfs. The exact definitions of the multiple Pdfs going into the calculation are found in Tab. 5.1.

The transformed discriminant d_L' is used to separate electrons from background by choosing a certain threshold value. Above this threshold electron candidates can be regarded as signal electrons. Different values of this threshold are used in order to define several operating points. These operating points are called *Very Loose*, *Loose*, *Medium* and *Tight*. The exact cut value of the discriminant d_L' depends on η and E_T. An example can be seen in Fig. 5.1. In this order, their background rejection is increasing and their signal efficiency decreasing. In addition to the likelihood requirements, the operation points have further criteria based on their track information: *Loose*, *Medium* and *Tight* operating points require at least two hits in the pixel detector and seven hits total in the pixel and SCT combined. This is called the *Pass Track Quality* criterion. All operation points except *Very Loose* require a hit in the innermost pixel layer in order to reduce background from photon conversions. The *Very Loose* operating point requires only one hit in the pixel detector [1].

5.2 Measurement of identification efficiencies

One of the key questions in physics measurements with electrons at ATLAS is how well can electrons be identified and how well does data and simulation agree in that matter. This section will focus on efficiency measurements of electron identification and introduces the so-called tag-and-probe method that is used to this end.

The measurement starts from a dataset which most likely consists of real, prompt electrons. This can be ensured by using signatures of well known processes like the decay of heavy particles such as the J/Ψ meson or the Z boson. These particles can decay into two electrons with opposite charge. A pair of electrons is selected by requiring one electron to pass the *Tight* identification criteria – the tag electron – whilst there are no identification requirements on the other electron – the probe electron. Imposing a mass constraints on the invariant mass of the two electrons (the di-lepton mass), ensures the probe is most likely a real

Table 5.1: Type and description of the quantities used in the electron identification. This table is copied from Ref. [1]. Discrimination power against certain kinds of backgrounds are listed in the column "Rejects". LF and HF are referring to light flavour and heavy flavour jets, respectively, while γ refers to photon conversions. HF in this context refers to b- or c-quarks, while LF refers to jets stemming from gluons and u-, d-, or s-quarks. Usage as likelihood indicates that the quantity is used to form a Pdfs as in Eq. (5.1). "C" indicates that this quantity is used as a direct cut.

Type	Description	Name	Rejects			Usage
			LF	γ	HF	
Hadronic leakage	Ratio of E_T in the first layer of the hadronic calorimeter to E_T of the EM cluster (used over the range $\lvert\eta\rvert < 0.8$ or $\lvert\eta\rvert > 1.37$)	R_{had1}	x	x		LLH
	Ratio of E_T in the hadronic calorimeter to E_T of the EM cluster (used over the range $0.8 < \lvert\eta\rvert < 1.37$)	R_{had}	x	x		LLH
Third layer of EM calorimeter	Ratio of the energy in the third layer to the total energy in the EM calorimeter. This variable is only used for $E_T < 80\,\text{GeV}$, due to inefficiencies at high E_T, and is also removed from the LLH for $\lvert\eta\rvert > 2.37$, where it is poorly modelled by the simulation.	f_3	x			LLH
Second layer of EM calorimeter	Lateral shower width, $\sqrt{(\Sigma E_i\eta_i^2)/(\Sigma E_i) - ((\Sigma E_i\eta_i)/(\Sigma E_i))^2}$, where E_i is the energy and η_i is the pseudorapidity of cell i and the sum is calculated within a window of 3×5 cells	$w_{\eta 2}$	x	x		LLH
	Ratio of the energy in 3×3 cells over the energy in 3×7 cells centred at the electron cluster position	R_ϕ	x	x		LLH
	Ratio of the energy in 3×7 cells over the energy in 7×7 cells centred at the electron cluster position	R_η	x	x	x	LLH
First layer of EM calorimeter	Shower width, $\sqrt{(\Sigma E_i(i - i_{\text{max}})^2)/(\Sigma E_i)}$, where i runs over all strips in a window of $\Delta\eta \times \Delta\phi \approx 0.0625 \times 0.2$, corresponding typically to 20 strips in η, and i_{max} is the index of the highest-energy strip, used for $E_T > 150\,\text{GeV}$ only	w_{stot}	x	x	x	C
	Ratio of the energy difference between the maximum energy deposit and the energy deposit in a secondary maximum in the cluster to the sum of these energies	E_{ratio}	x	x		LLH
	Ratio of the energy in the first layer to the total energy in the EM calorimeter	f_1	x			LLH
Track conditions	Number of hits in the innermost pixel layer	n_{Blayer}		x		C
	Number of hits in the pixel detector	n_{Pixel}		x		C
	Total number of hits in the pixel and SCT detectors	n_{Si}		x		C
	Transverse impact parameter relative to the beam-line	d_0		x	x	LLH
	Significance of transverse impact parameter defined as the ratio of d_0 to its uncertainty	$\lvert d_0/\sigma(d_0)\rvert$		x	x	LLH
	Momentum lost by the track between the perigee and the last measurement point divided by the momentum at perigee	$\Delta p/p$	x			LLH
TRT	Likelihood probability based on transition radiation in the TRT	eProbabilityHT	x			LLH
Track–cluster matching	$\Delta\eta$ between the cluster position in the first layer and the extrapolated track	$\Delta\eta_1$	x	x		LLH
	$\Delta\phi$ between the cluster position in the second layer of the EM calorimeter and the momentum-rescaled track, extrapolated from the perigee, times the charge q	$\Delta\phi_{\text{res}}$	x	x		LLH
	Ratio of the cluster energy to the track momentum, used for $E_T > 150$ GeV only	E/p	x	x		C

signal electron.

The electron identification efficiency ε_{id} is measured by counting how many probe electrons pass a certain identification criterion out of all available probe electrons:

$$\varepsilon_{\text{id}} = \frac{N_{\text{probe electrons passing identification criteria}}}{N_{\text{all probe electrons}}} \tag{5.4}$$

Usually the efficiencies are measured as a function of $\eta - E_T$ of the electron.

ATLAS is using J/Ψ meson and Z boson decays for identification measurements. In case of using the Z boson resonance, there are two methods measuring ε_{id} called Z_{mass} and Z_{iso}, respectively [106]. The difference between these two Z methods is how the residual background is estimated.

The background under the Z peak is expected to be lower than 2%, when both electrons pass the identification criteria. This however still results in a small but significant effect on the final efficiency. Furthermore, when the probe electron only passes track quality criteria, i.e. in the determination of the denominator of Eq. (5.4), the background can become even larger than the signal $Z \to ee$ (Zee) contribution. Thus, backgrounds have to be be estimated carefully and subtracted beforehand calculating the identification efficiency in data. Therefore, the efficiency from Eq. (5.4) is to be written as

$$\varepsilon_{\text{id}} = \frac{N_{\text{probes pass identification}} - N_{\text{bkg,num}}}{N_{\text{all probes}} - N_{\text{bkg,den}}} \,. \tag{5.5}$$

This equation accounts for the residual background which is to be subtracted from all probes in both the denominator and numerator terms. Background events in the numerator also have to pass the identification criteria, therefore it is expected that the number of background events in the numerator, $N_{\text{bkg,num}}$, is significantly lower than in the denominator ($N_{\text{bkg,den}}$). Background can be for example mis-identified photons, secondary electrons, or mis-identified hadrons as well as electrons in jets. The background is difficult to estimate using MC simulation, because only a small fraction of the produced hadronic particles is expected to pass the electron reconstruction and identification criteria, such that a larger event sample would have to be generated than is computationally feasible. In addition, the modelling of the background using MC simulation is difficult as it is a mixture of instrumental backgrounds as well as backgrounds that depend on the hadronisation models.

Both methods take advantage of the fact, that signal electrons cluster or peak in certain distributions. Therefore the background can be estimated in a data-driven way using the sidebands around the peak region in these distributions. The Z_{mass}

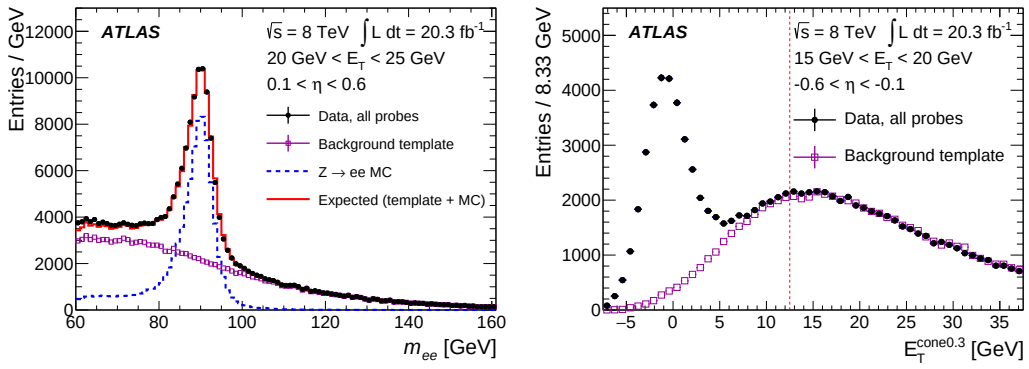

Figure 5.2: Examples for two different Z based tag-and-probe methods in order to estimate the background using 2012 data, taken from Ref. [106]. The left plot shows the m_{ee} distribution of the tag-and-probe electrons in data as well as the expected background and a MC signal estimate. The right one shows the $\Delta E_T^{\text{cone0.3}}$ distribution of the probe election in data and a background estimate.

method uses the peak of the Z boson directly for background subtraction and signal extraction.The Z_{iso} method on the other hand uses the isolation variable $\Delta E_T^{\text{cone}\Delta R}$. The transverse cone energy $\Delta E_T^{\text{cone}\Delta R}$ is defined as the sum of the transverse energy deposited in the calorimeter cells in a cone of size ΔR around the electron, excluding the contribution within $\Delta\eta \times \Delta\phi = 0.125 \times 0.175$ around the electron cluster barycentre [106]. Real electrons have usually very small isolation values as opposed to hadronic backgrounds.Examples of the Z_{mass} and Z_{iso} signal and background estimates using Run-1 data are shown in the left and right plot, respectively, of Figure 5.2.

Previous measurements using these methods are e.g. documented in Ref. [1] using data collected in 2015 and 2016 and in Ref. [2] using the dataset collected between 2015 and 2017, respectively. In both references the Run-1 algorithm was used with only minimal changes applied. However, the centre of mass energy was increased from 8 TeV to 13 TeV in Run-2. In addition the average PU rate is significantly higher in Run-2 with respect to Run-1. Because of these new data taking conditions and also the higher statistics, some of the methods' premises have to be questioned. Here the Z_{mass} case is discussed.

In case of probe electrons having a transverse energy lower than 30 GeV, the systematic errors have increased drastically in newer datasets. This could be tracked down to the definition of background templates and as well as their normalisation procedure. The latter is based on doing sideband normalisation using tag-and-probe electrons with the same charge instead of opposite charge. The

normalisation factors are then transferred to the opposite charge background template, which then is subtracted. Using two different normalisation regions – one below the Z mass peak and one above – introduces very large systematic uncertainties and indicated that the shape of the background template is not optimally describing the data. A reason for this might be, that the template itself is defined too far away from the signal region definition. In addition the background templates usually contain some residual background which has to be subtracted. The old algorithm might not estimate this signal contamination correctly. Moreover, systematic errors are calculated using a root-means-square approach, combining all possible combinations of variations, making it hard to track down sources of uncertainties. The final result of the efficiency measurement is a combination of the Z_{mass} and Z_{iso} results. In the region of probe electron $E_T < 30$ GeV, a huge discrepancy between the two methods was observed. Its origin might as well lie in the above described problems.

In the following an update to the mentioned Z_{mass} method using the full ATLAS Run-2 dataset collected in the years 2015 to 2018 is presented, facing the listed challenges. It makes use of a new likelihood based background template definition and optimises the signal contamination estimate of these templates. In addition the background normalisation is obtained by a template fit, taking the full expected signal and background shapes into account and drops the usage of same-sign normalisation. The calculation of systematic errors is updated as well.

5.3 The Z_{mass} method

As the electron efficiencies are determined in bins of η and E_T, for the Z_{mass} method the m_{ee} data distributions are considered separately in each η-E_T bin. Because of Eq. (5.5) in the following, the number of all probe electrons passing the *Track Quality* requirement are referred to as the denominator, while the number of probe electrons passing the identification requirements (*Tight*, *Medium*, *Loose*) is referred to as the numerator. The full Z_{mass} algorithm is sketched in Figure 5.3, it is implemented making use of the ROOT framework [107] and consists of five steps, with each of these steps being discussed in a dedicated subsection following the same numbering as in fig. 5.3:

1. Subsection **5.3.1 Input preparation** lays out the steps of retrieving the input histograms for the method. This includes the used data and MC samples, as well as the event selection. The construction of a data-driven background template is by inverting the probe identification requirements is explained.

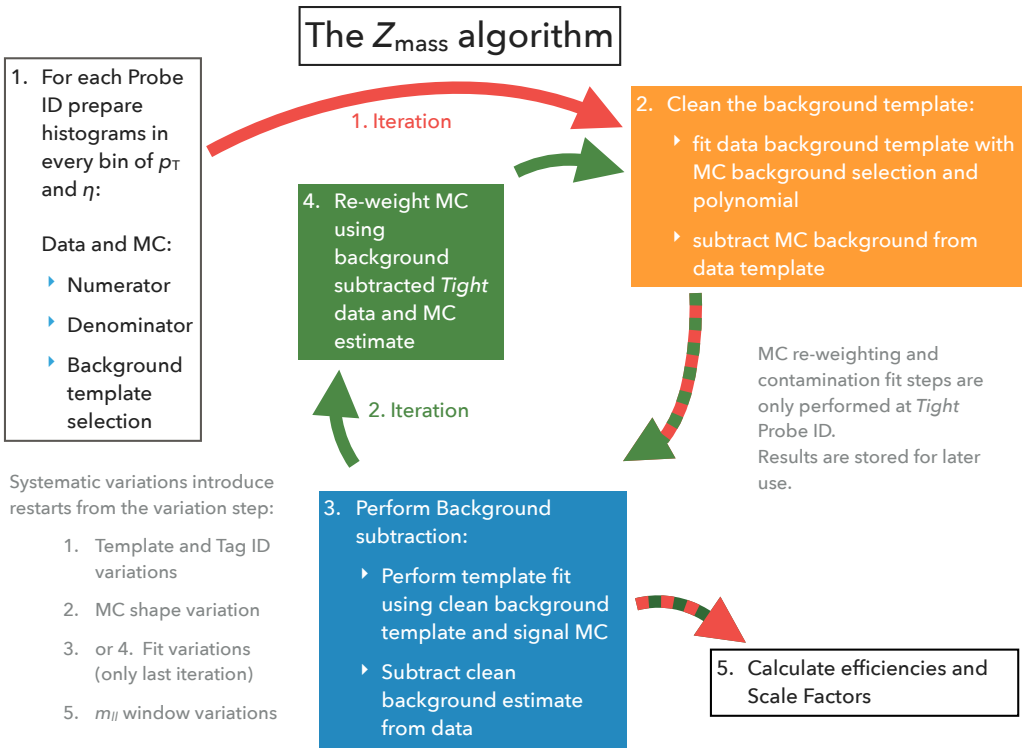

Figure 5.3: Sketch of the Z_{mass} algorithm. It consists of five steps: 1. Input – 2. Background cleaning – 3. Background estimation – 4. Re-weighting – 5. Calculation. The re-weighting step depends on the background estimations steps two and three. After the re-weighting step, the second, third and fifth step are repeated.

The same background template definition is used for numerator and denominator background estimates.

2. Background templates usually contain residual signal contamination. For optimal results this has to be subtracted, otherwise the background contribution would be overestimated. This is achieved using a signal contamination estimation fit, discussed in more detail in Subsection **5.3.2 Template cleaning**. The data background template is fitted using a polynomial function and a template obtained from a *Zee* MC sample having the same background selection criteria applied as the data driven background template. Using the MC driven signal contamination estimate ensures the shape of the signal contamination is estimated correctly, this is hard to achieve doing a purely analytical fit.

3. To obtain the background estimates, a template fit of the data is performed

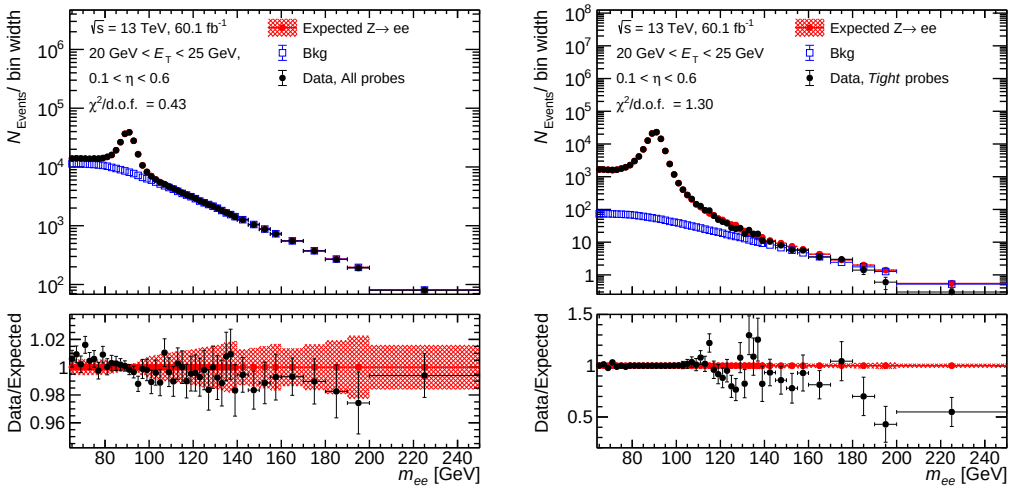

Figure 5.4: Exemplary distributions used in the Z_{mass} method. Shown is the tag-and-probe mass distribution for $20\,\text{GeV} < E_T < 25\,\text{GeV}$ and $0.1 < \eta < 0.6$. Data is represented using black dots. The left plot shows a denominator distribution, which means no identification criteria are applied to the probe electrons, while the right plot shows the same distribution with *Tight* likelihood criteria applied to the probes. Also shown is the prediction consisting of MC simulation + background template (red). The background template is shown in blue. The shown distributions are post-fit and have all corrections described in the text applied.

using the background template obtained in 2. and a MC Zee signal template. This is explained in detail in Subsection **5.3.3 Background fit**. Figure 5.4 shows a post-fit example of these m_{ee} distributions in one η-E_T bin. The background estimate is obtained for the numerator and the denominator case independently.

4. Since MC predictions are used in both fits, it is important to ensure their shape is not biasing the fit results due to mis-modelling detector effects. This is why a re-weighting technique is introduced in Subsection **5.3.4 MC re-weighting**. It is applied in a second iteration of the method, using the results of the previous steps.

5. After background fits are performed using the optimised background and signal templates, data efficiencies can be calculated for data, accordingly to Eq. (5.5). This is done in Subsection **5.3.5 Calculation of efficiencies and scale factors**. MC efficiencies are easy to calculate, since no background subtraction needs to be performed. To account for differences in data and

simulation, scale factors (SFs)

$$\text{SF} = \frac{\varepsilon_{\text{id,data}}}{\varepsilon_{\text{id,MC}}} \tag{5.6}$$

for MC efficiencies are calculated.

Systematic variations

Each of the steps introduces systematic uncertainties. These are estimated by systematic variations. This means, the procedure is repeated with a change in the method, resulting in a different result. The difference between these alternative results and the result from the default procedure is used for calculating the systematic uncertainties. Systematic variations are highlighted in the text, whenever they are undertaken.

5.3.1 Input preparation

The full ATLAS Run-2 dataset is used, i.e. data collected in the years 2015 to 2018 with the LHC operating at a centre-of-mass energy of $\sqrt{s} = 13$ TeV and a bunch spacing of 25 ns.

The used *Zee* MC samples were generated using NLO in QCD using Powheg [108] interfaced to the Pythia8 [109] parton shower model using the CT10 PDF [110] in the matrix element. The sample production used the AZNLO set of tuned parameters [111] for modelling non-perturbative effects in the QCD parton shower, making use of the CTEQ6L1 PDF set [112]. QED emissions from electroweak vertices and charged leptons were simulated using Photos++ 3.52 [113].

Additional PU events were generated with the soft QCD processes of Pythia8, in order to match the high PU conditions of the LHC environment. These additional events use the A3 set of tuned parameters [114] and the NNPDF23LO PDF [115]. These tuned parameters overestimate the underlying event activity by around 3% [2], which is why simulated events were scaled down by this factor when matching them to the data PU profile. Three different MC sample sets were produced to better match the different data taking conditions of the years 2015/2016, 2017 and 2018. These different conditions are e.g. PU conditions, varying TRT gas mixtures and different LAr temperature settings as well as different trigger menus.

For matching reconstructed and generated electrons, an ID track based algorithm [116] is used. This matching is needed in order to separate simulated electrons from bremsstrahlung in the selection step.

Event selection

All events recorded have to pass an event cleaning cut and a good-run-list requirement, ensuring that all detector components are functioning as expected [117]. At least one reconstructed primary vertex has to be in the event. The electrons and are selected by a single electron trigger with a minimum E_T threshold of 24 to 26 GeV and requires *Tight* trigger identification. The exact trigger requirements changed with the year of data taking.

Events passing these basic selection requirements furthermore need to contain at least two electron candidates passing the η and E_T requirements: Both electrons need to lie within $|\eta| < 2.47$, while tag electrons are not to be reconstructed within the transition region $1.37 < |\eta| < 1.52$. In addition tag electrons need to be reconstructed with a minimum transverse energy $E_T > 25\,\text{GeV}$, probes need to suffice at least 15 GeV. In case of simulated electrons, none of the electrons must originate from background processes, this is ensured by matching generated and reconstructed electrons.

Tag electrons need to be matched to a trigger electron object within $\Delta R < 0.07$, suffice a track isolation requirement of $E_T^{\text{cone0.3}}/E_T) < 0.1$ and pass the *Tight* tag identification requirement.

Systematic variation: Even though the tag electron selection criteria are very strict, it cannot be ruled out, that some background objects still pass these criteria. In order to estimate the possible bias, an additional isolation cut is applied by requiring the tag electron to pass $E_T^{\text{cone40}} < 5\,\text{GeV}$. The whole Z_{mass} method is repeated with this tag selection criteria as a systematic variation.

Signal selection

Probe electrons need to pass the *Track Quality* criteria. Tag-and-probe electrons need to be of opposite charge, their combined mass needs to lie within a certain mass window around the Z peak.

For the numerator term, the probe electrons need to pass also the identification requirement whose efficiency is to be measured, i.e. *Loose*, *Medium*, or *Tight*.

One event can contain more than one tag-and-probe pair and any combination of tags and probes is used as long as the electron candidates fulfil the respective requirements. Thus, an electron can be used as a tag as well as probe electron in the measurement.

Background selection

Background events are selected by inverting the likelihood requirement of the probe electrons but keeping the *Pass Track Quality* criterion. Two inverted likelihood requirements are defined: *Fail Very Loose* and *Fail Ultra-Loose*. The *Fail Ultra-Loose* requirement is based on a custom likelihood identification criterion, the *Ultra-Loose* identification. It is defined by a discriminant cut being twice as far from the *Loose* discriminant value as the *Very Loose* discriminant value.

Further reducing signal electrons within this selection, isolation cuts are defined by the ratio of the transverse cone energy and the transverse energy

$$\frac{E_T^{\text{cone}\Delta R}}{E_T} > x, \tag{5.7}$$

where x can be an arbitrary number and ΔR is either 0.3 or 0.4. This is an inversion of the isolation requirement of signal electrons. Before a value of the isolation cut was chosen, values in the range between $x = 0.01$ and $x = 0.2$ were tested in combination with the two different identification cuts.

A quantity for measuring the quality of background templates is introduced as the sum of all post-fit χ^2 values:

$$\chi^2_{\text{total}} = \sum_{\eta, E_T} \frac{\chi^2}{\text{d.o.f.}} \tag{5.8}$$

These are calculated in all bins of η and E_T from the post-fit results as for examples already shown in Figure 5.4. It is assumed, that a low value of χ^2_{total} reflects an overall reasonable estimation of background events. Tab. 5.2 lists the resulting χ^2_{total} values for various background template definitions going into the Z_{mass} method.

It is found that, likelihood cuts closer to the signal regions result in lower values of χ^2_{total}. That is *Fail Very Loose* is performing better than *Fail Ultra-Loose*. The same is true for the ΔR value and the ratio x: Reducing the ratio, is getting closer to the signal region, which has the requirement of $E_T^{\text{cone0.3}}/E_T < 0.1$.

Getting close to the signal region has the advantage of having a less biased background template, since it contains events that are more similar to those that are likely to be mis-identified as signal. On the other hand more signal events are passing the background selection, resulting in signal contamination of the templates. Therefore, no values of $x < 0.01$ are considered, since too much signal contamination also might bias the final result too much. The signal contamination needs to be removed, as described in Section 5.3.2. It is found that this signal

contamination cleaning is performing well, therefore the *Fail Very Loose* template with an isolation requirement of $E_T^{\text{cone0.3}}/E_T > 0.1$ is chosen to be the default background selection.

Systematic variation: The default background selection leads to very good fit results and a solid background estimate. However it cannot be excluded the default selection is still introducing a bias on the shape of the background. This can be introduced by either of the two selection criteria, therefore both are varied as systematic variations:

- The likelihood requirement is varied to be *Ultra-Loose* instead of *Very Loose*, while keeping the isolation requirement.
- Another variation is targeting the isolation cut: The cone size and the isolation ratio is varied, requiring $E_T^{\text{cone0.4}}/E_T > 0.7$.

Table 5.2: The calculated values of $\chi^2_{\text{total}} = \sum_{\eta,E_T} \chi^2/\text{d.o.f.}$ for different background selections calculated at the denominator distributions. The lower χ^2_{total}, the better the general final fit result, and the better the template. Looser background selection cuts are resulting as expected in a lower χ^2_{total}. The isolation cut is defined by $E_T^{\text{cone}\Delta R}/E_T$ being greater than a certain value of x. The table lists the choice of ΔR, x, as well as the likelihood cut. In general lower values of x result in a better performance of the template regarding χ^2_{total}, however they also result in a higher number of signal events in the background templates.

ΔR	x	χ^2_{total} (*Fail Very Loose*)	χ^2_{total} (*Fail Ultra-Loose*)
0.3	0.01	489.72	595.93
	0.02	497.81	603.23
	0.03	506.57	612.22
	0.04	516.18	621.65
	0.05	527.49	632.74
	0.07	552.26	657.89
	0.10	601.79	706.46
	0.20	872.58	976.9
0.4	0.01	523.11	633.76
	0.02	530.86	641.37
	0.03	539.43	650.22
	0.04	548.92	659.93
	0.05	559.11	670.38
	0.07	583.40	694.21
	0.10	621.82	734.29
	0.20	833.71	949.23

Input histograms

As input for the further Z_{mass} algorithm histograms of the m_{ee} distribution are filled with those tag-and-probe pairs that fulfil the selection criteria defined in the previous section. This is done in bins of η and E_T of the probe electron, with the exact binning being listed in Tab. 5.3.

Efficiencies are also calculated as a function of the mean number of interactions per bunch crossing μ, in this case, no η binning is applied. Signal templates are build from MC events passing the numerator or denominator requirements. Background templates are constructed from data and MC, where the MC is used as an estimate for the signal contamination in the data background template. All histograms are binned in 1 GeV in m_{ee}. This makes it easy to apply re-binning algorithms when needed.

Table 5.3: Binning used for the calculation of histograms. By default efficiencies are calculated in bins of $E_T - \eta$, where a default and a fine binning in η is provided. Note that in the highest bin of E_T efficiencies are binned in the absolute value of η due to low statistics. When efficiencies are calculated in bins of the mean number of interactions per bunch crossing μ, the whole η and E_T range is considered.

variable	bin edges
E_T [GeV]	$15, 20, 25, 30, 35, 40, 45, 50, 60, 80, 150, 250$
η	$-2.47, -2.37, -2.01, -1.81, -1.52, -1.37, -1.15, -0.8, -0.6, -0.1,$ $0, 0.1, 0.6, 0.8, 1.15, 1.37, 1.52, 1.81, 2.01, 2.37, 2.47$
fine η	$-2.47, -2.4, -2.3, -2.2, -2.1, -2.0, -1.9, -1.8, -1.7, -1.65, -1.6,$ $-1.52, -1.37, -1.3, -1.2, -1.1, -1.0, -0.9, -0.8, -0.7, -0.6, -0.5,$ $-0.4, -0.3, -0.2, -0.1, 0.0, 0.1, 0.2, 0.3, 0.4, 0.5, 0.6, 0.7, 0.8, 0.9, 1.0,$ $1.1, 1.2, 1.3, 1.37, 1.52, 1.6, 1.65, 1.7, 1.8, 1.9, 2.0, 2.1, 2.2, 2.3, 2.4, 2.47$
μ	$0, 2, 4, 6, ..., 100$

5.3.2 Template cleaning

The scaling of the contamination estimate s_{cont} can be approximated by the fraction of probe electrons passing *Tight* criteria in data and MC in the Z peak region:

$$s_{\text{cont,start}} = \left. \frac{N_{\textit{Tight}\text{ probes, data}}}{N_{\textit{Tight}\text{ probes, MC}}} \right|_{m_{ee} \in [80,100]\,\text{GeV}} \tag{5.9}$$

Neglecting the residual background in *Tight* data and assuming data and simulation have the same efficiency of passing the background selection, this is expected to be a solid estimate in $E_T < 30\,\text{GeV}$. This is the old method to estimate it, used

in the measurements in the References [1, 2]. However, for higher energies this simple approach is overestimating the signal contamination using the previously defined new likelihood-based templates. Therefore a new way to estimate the signal contamination of the background templates has to be developed.

This is done using a likelihood fit, making use of the RooFit package [118]. In each η-E_T-bin the m_{ee} distribution of the background template is regarded. Both, the shape of the pure background, as well as the shape of the signal contamination are hard to parametrise using analytic functions, especially since the background composition changes within the energy range.

The safest estimate is using the *Zee* MC sample and applying the same background selection as on data. The resulting template is used then as an estimate of the signal contamination.

Histograms with background selection have a smoothing algorithm [119] applied, using $N = 3$ iterations. This helps to improve the stability of the fits, since statistical fluctuations in the shape are smoothed out. No influence of the smoothing algorithm on the final result is expected, this was also tested by comparing results retrieved using the smoothing algorithm and results retrieved not using it. The effect of the smoothing on the background templates is demonstrated in fig. 5.5. Only local fluctuations on the shape are smoothed out, the general shape of the templates are not affected.

As an estimate of the "true" background a simple polynomial function is used as approximation. This might not be very accurate on the full m_{ee} spectrum, which is why the fit region is restricted to the Z peak region, with $70\,\text{GeV} < m_{ee} < 115\,\text{GeV}$. To reduce the impact of statistical fluctuations inside the MC estimate and the data background template, the input histograms have a bin-width in m_{ee} of 3 GeV. In almost all E_T bins a 2nd degree polynomial is used as default for estimating the "true" background. The background shape is similar to a falling spectrum for $E_T < 20\,\text{GeV}$, therefore the fit function is restricted to have positive curvature* in this bin. For $E_T < 20\,\text{GeV}$ higher transverse energy, the background shape is expected to have negative curvature. An exception is the $20\,\text{GeV} < E_T < 25\,\text{GeV}$ bin: It marks a transition region in terms of background shape. The spectrum in low m_{ee} has a shoulder, meaning the curvature is expected to have positive curvature, while for higher m_{ee} it still has the shape of a falling spectrum. Therefore a 3rd degree polynomial is chosen in this bin as default. Because of the difficult shape of the background in $E_T < 35\,\text{GeV}$, a lower level on the resulting scaling is chosen to be $s_{\text{cont,low}} = 90\% \cdot s_{\text{cont,start}}$. The effect of this on the resulting fit result

*Positive curvature means, that the corresponding parameter in the used RooChebychev fit function is restricted to positive values. This corresponds to a positive second derivative of the function within the fit region. The RooChebychev pdfs are Chebychev polynomials of first kind.

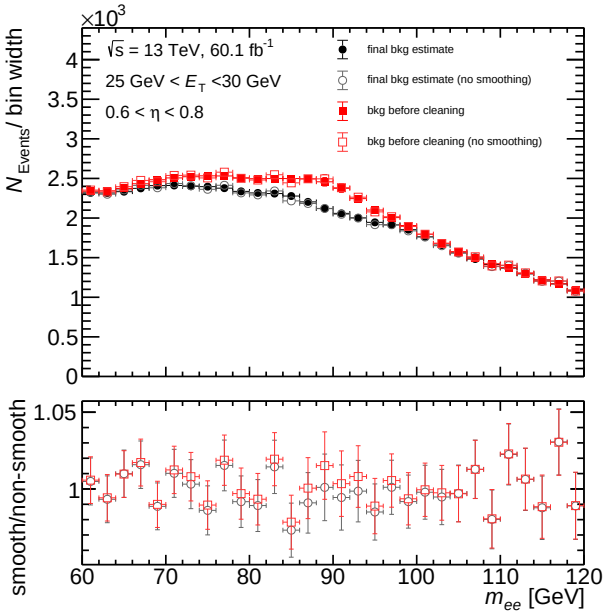

Figure 5.5: Background template distributions in the 25 GeV $< E_T <$ 30 GeV bin for $0.6 < \eta < 0.8$. The black points show the final background estimate, having the smoothing algorithm applied. The red full square points show the "raw" data template before the signal contamination removal. In comparison the final estimate without any smoothing (grey circles) and the non-smoothed "raw" template are shown (empty red squares). The corresponding ratios of the smoothed/non-smoothed distributions show only statistical fluctuations around 1, the general shape of the background estimate is not affected. Therefore it also can be expected, that the smoothing has no effect on the efficiency estimate.

is shown in Figure 5.6.

Especially in the 15 GeV $< E_T <$ 20 GeV bin, the fit result is dominated by the lower fit bound. However in this region, the overall efficiency result is less dependent on the signal contamination due to the background shape. Fit results using data collected in 2018 for three bins of low transverse energy and one bin of high E_T are shown in Figure 5.7.

Systematic variations: Three systematic variations are performed for estimating the bias introduced by this method. Variations target the possible bias introduced by the lower limit on the MC scale $s_{\text{cont,low}}$, the binning and the fit function:

- A binning variation, shifts the fit region in m_{ee} by 5 GeV, using the range 65 GeV $< m_{ee} <$ 110 GeV, in bins of 5 GeV. In $E_T <$ 35 GeV, the lower limit on the fit result, $s_{\text{cont,low}}$, is reduced by 20%.
- The fit function is varied, using a linear function, targeting a background

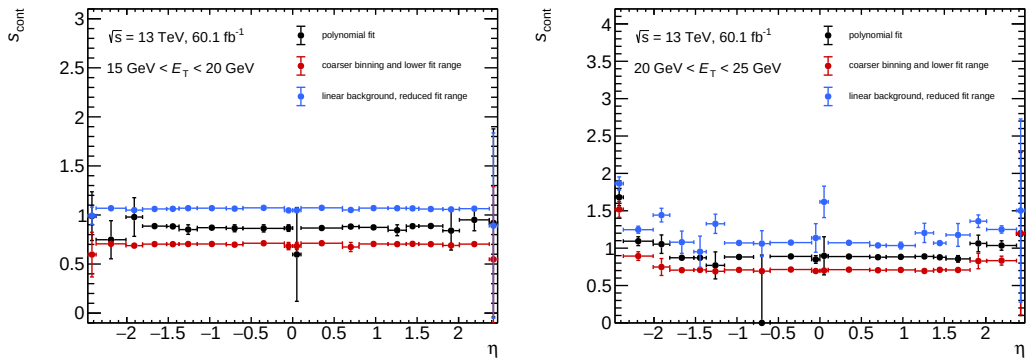

Figure 5.6: Fit results for the value of s_{cont} in the two lowest bins of E_T using the 2018 dataset. Shown are the nominal fit results (black), as well as the systematic variations where $s_{\text{cont,low}}$ is reduced and increased by 20% (red and blue, respectively). The shown errors are the resulting HESSE errors on the fit result. Especially in the 15 GeV $< E_T <$ 20 GeV bin, the fit result is dominated by the lower fit bound.

shape variation. The fit region is restricted to the Z peak (76 GeV $< m_{ee} <$ 103 GeV) in order to make up for this coarse shape estimate. In $E_T <$ 35 GeV, the lower limit on the fit result is increased by 20% with respect to the nominal.

- Symmetric fit uncertainties calculated using the HESSE method [120] are used as a third variation. These errors take parameter correlations and non-linearities. In some bins the resulting scaling would become negative doing this variation. In this (unphysical) case the variation is restricted, thus the minimal scaling is set to be 0 to make sure no signal contamination would be added in this case.

Figure 5.8 shows examples of these variations.

5.3.3 Background fit

The actual background estimate is done by doing a template fit using the cleaned data background template and the MC *Zee* signal prediction. Again the fit is performed making use of the RooFit package.

The m_{ee} data distributions are fitted independently for the numerator and denominator case, referring to Eq. (5.5). In this context, the term numerator has the meaning of tag and probe electron pairs, where the probe electron passes the identification criteria, while the term denominator refers to all possible tag and probe electron pairs. For avoiding any shape bias from the Z mass peak, a re-binning is applied. To enhance the influence of the tails on the final fit result, three bins

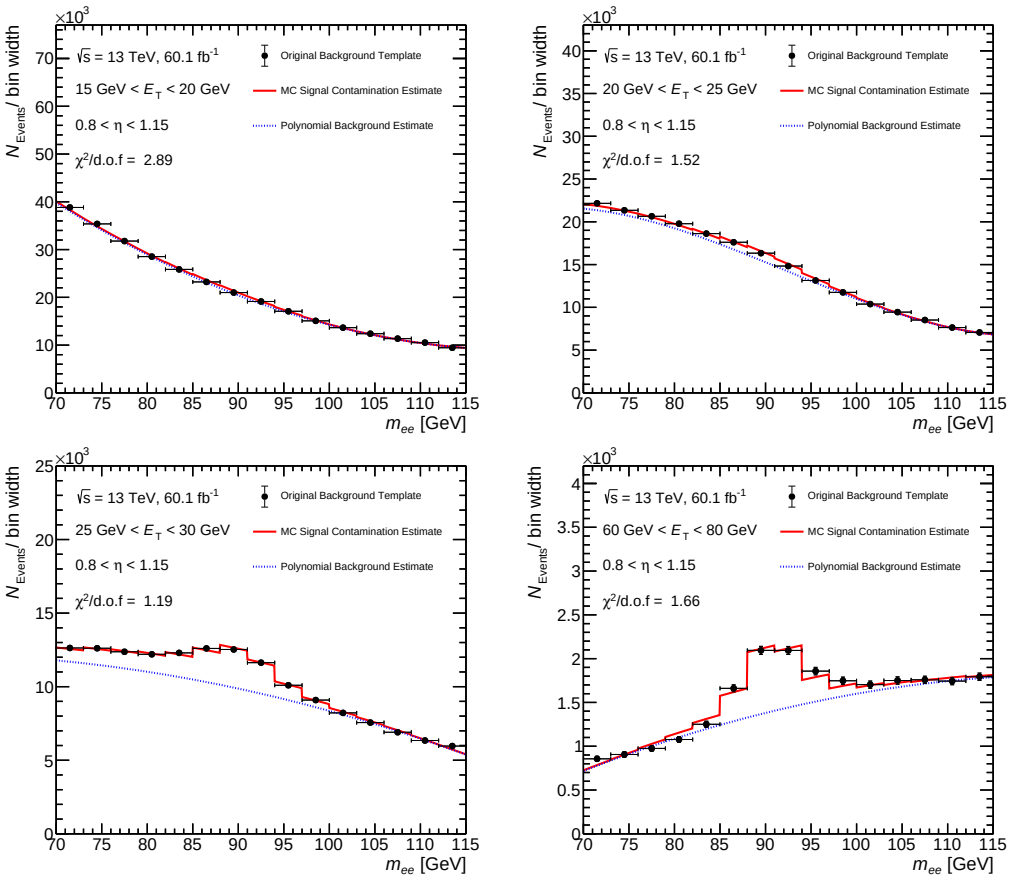

Figure 5.7: Fit results in four different bins of E_T. The top left plot shows the fit result for $E_T < 20\,\text{GeV}$. The lower limit on the signal contamination estimate is crucial here, otherwise all fits would converge to 0. The top right shows the estimate for $20\,\text{GeV} < E_T < 25\,\text{GeV}$, the shape of the background is more complicated here, also compared to $25\,\text{GeV} < E_T < 30\,\text{GeV}$ (bottom left) and higher transverse energy ($60\,\text{GeV} < E_T < 80\,\text{GeV}$, bottom right). For higher transverse energy the expected shape has a negative curvature, making it easier to fit the residual Z peak. The raw data background template is plotted in black. The red line in the plots actually represents the sum of the signal contamination estimate and the polynomial background. The polynomial background itself is shown in blue.

below and above the peak are chosen for the denominator case. Because the tails might suffer from low statistics, only one bin below and above is implemented in the numerator case. The exact m_{ee} bin edges in GeV used in the fit are the following:

$$\text{Numerator} : \{65, 80, 100, 250\}$$

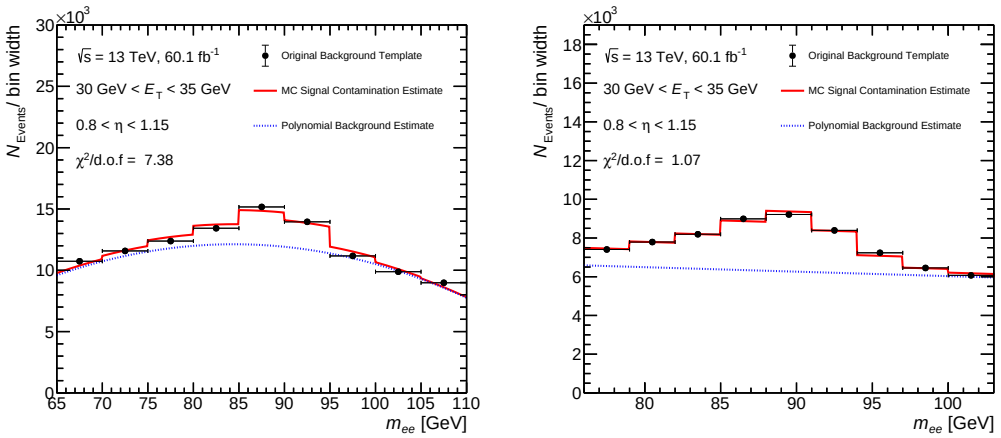

Figure 5.8: Fit variations of the template cleaning method in the 30 GeV $< E_T <$ 35 GeV bin for $0.8 < \eta < 1.15$, the same bin shown previously in Figure 5.5. The left plot shows the variation using a coarser binning in m_{ee} in addition to a shifted fit range. The right shows the use of a linear function combined with a fit range beneath the Z peak. The raw data background template is plotted in black. The red line in the plots actually represents the sum of the signal contamination estimate and the polynomial background. The polynomial background itself is shown in blue.

$$\text{Denominator} : \{65, 70, 75, 80, 100, 120, 150, 250\}$$

Numerator and denominator are referring to Eq. (5.5). Figure 5.9 shows an example of the fit result from the described method.

Systematic variations: The background fit introduces additional uncertainties on the background shape. To account for possible biases from the fit, the fit region is varied to be only on the low mass tail of the Z mass distribution, or only on the high mass tail. Regarding e.g. Fig. 5.4, the low mass tail is the region $m_{ee} < 80$ GeV, the high mass tail is referring to the region $m_{ee} > 120$ GeV. Thus, either the three lowest or highest bins are removed from the nominal binning. The numerator fit is not very sensitive to shape variations due to the low residual background. Therefore numerator fits keep at least three bins, ensuring each bins has enough statistics.

- The low mass tail variation consists of fitting three bins below the Z peak and one bin on the peak. The numerator case uses three bins, with the highest bin restricted to 120 GeV:

$$\text{Low tail numerator} : \{65, 80, 100, 120\}$$

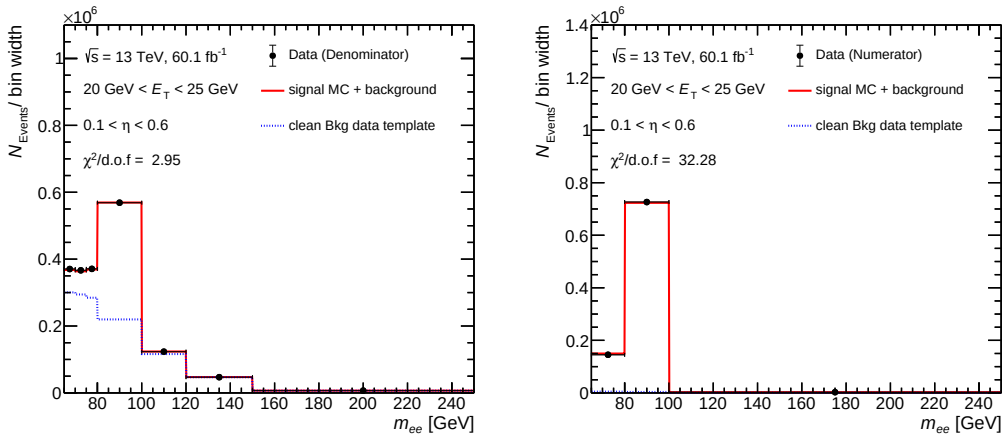

Figure 5.9: Fit output from the background fit in the $20\,\text{GeV} < E_T < 25\,\text{GeV}$ and $0.1 < \eta < 0.6$ bin. Shown is the fit result using re-binned data, background and signal MC templates. On the left the denominator result is shown, while on the right the fit result of the *Loose* numerator is illustrated. Numerator and denominator are referring to Eq. (5.5).

$$\text{Low tail denominator} : \{65, 70, 75, 80, 100\}$$

- Similar the high mass tail variation cuts of the low m_{ee} bins of the nominal binning:

$$\text{Numerator} : \{80, 100, 120, 250\}$$
$$\text{Denominator} : \{80, 100, 120, 150, 250\}$$

- As in the template cleaning fit, the error from the HESSE method is applied to the background estimate as systematic variation.

Numerator and denominator are referring to Eq. (5.5). Figure 5.10 shows example plots of the two fit range variations.

5.3.4 MC re-weighting

The described background template fit and the signal cleaning fit both take MC predictions as input. Thus, the MC modelling needs to be accounted for and corrected where necessary. This is particularly the case for the modelling of the electron energies in the transition regions $1.37 < |\eta| < 1.52$ and the outermost bins of eta $|\eta| > 2.37$. In the transition region, a lot of material inside the detector is leading to additional bremsstrahlung. This might not have been accounted for correctly in the detector simulation, leading to differences of the Z peak shape

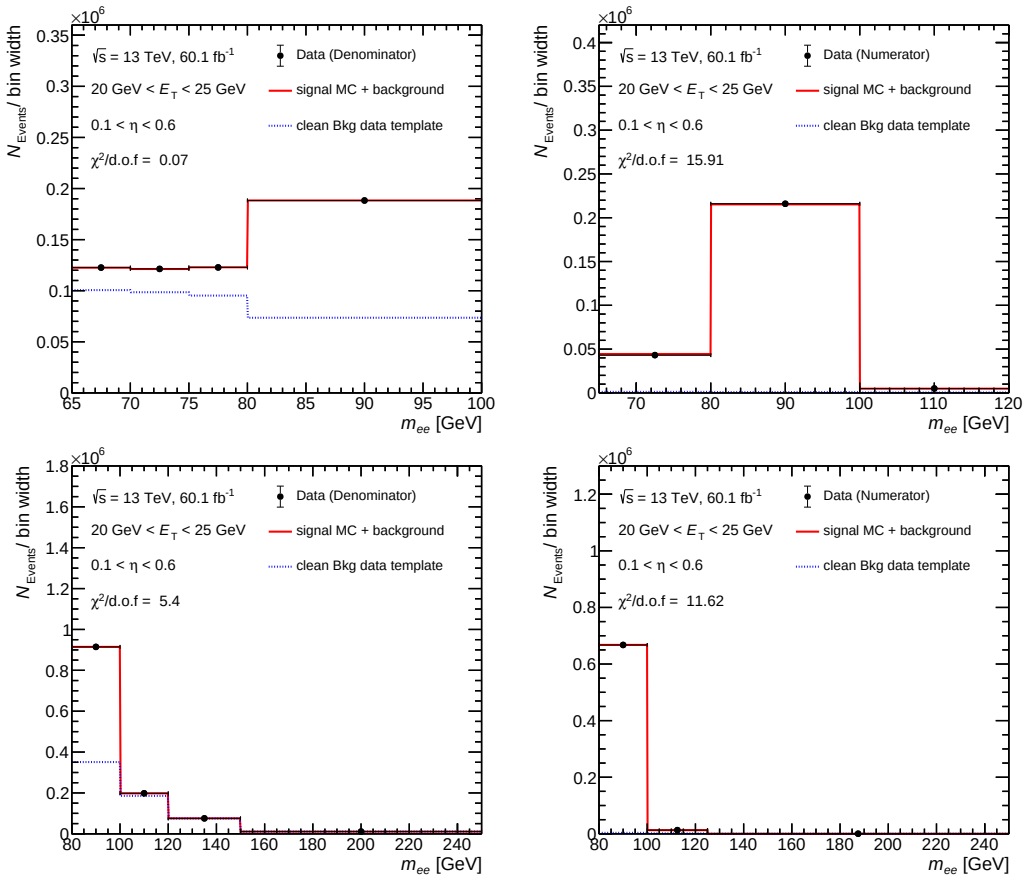

Figure 5.10: Fit output from the background fit in the 20 GeV $< E_T <$ 25 GeV and $0.1 < \eta < 0.6$ bin. The top plots show denominator (left) and *Loose* numerator (right) fit results for the low mass tail fit range variation described in the text. Numerator and denominator are referring to Eq. (5.5). Similarly, the bottom plots show an example of the high mass tail variation.

between data and simulation. The outermost bins of η suffer from losses in the energy reconstruction and also mark the outer edge of the tracking capabilities, which might lead to discrepancies of electron reconstruction efficiencies. This can lead to differences of the observed signal contamination inside the templates and the predicted estimate of simulated electrons failing the identification cuts, resulting in an unsound signal contamination estimation. Both of these effects are illustrated in Figure 5.11. Additionally, the modelling of the Z peak and its tails is not perfect due to the MC generator being only NLO and not including electroweak effects.

To account for these effects, an iterative re-weighting method is introduced. This method calculates "re-weighting functions" as the ratio of the number of tag-

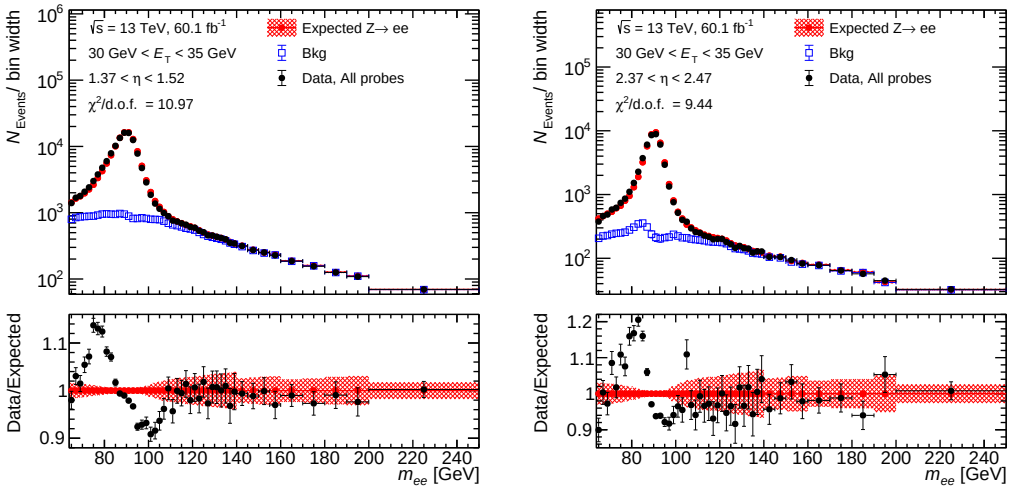

Figure 5.11: m_{ee} distributions in Z_{mass} with no re-weighting correction applied. Two cases of MC mis-modelling leading to suboptimal fit results. The left plot shows the post-fit denominator distributions inside the transition region. The MC shape does not fit the data peak, leading to a wiggle in the ratio. The right plot shows a similar distribution, but in an outermost bin of η. The uneven background shape beneath the peak is a result of poor modelling of signal contamination. In addition to signal MC shape issues this is leading to huge discrepancies in the ratio observed/expected.

and-probe electrons passing the *Tight* identification requirements. This achieved by the division of the Eq. (5.5) numerator data m_{ee} histograms by the corresponding numerator MC m_{ee} histograms. The term numerator is used again with the meaning of probe electrons passing the identification criteria.

Since the *Tight* numerator m_{ee} distribution still contains residual background, this has to be subtracted before the ratio is calculated. However, the exact background is not known, when the re-weighting functions are calculated the first time. This is why the function is obtained after the Z_{mass} algorithm already calculated the background estimate, using the "raw" MC inputs. The first iteration makes use of non re-weighted MC templates. The scalings s_{bkg} and s_{cont} for the signal contamination and the background template, respectively, are stored. A second iteration of the method then can make use of these fit results and subtract the cleaned background from the data numerator before the reweighing functions are calculated as a function of m_{ee}:

$$f_{\text{rew}}(m_{ee}) = \frac{N_{\text{data},tight}(m_{ee}) - s_{\text{bkg}} \cdot (N_{\text{data,bkg}}(m_{ee}) - s_{\text{cont}} \cdot N_{\text{MC,bkg}}(m_{ee}))}{N_{\text{MC},tight}(m_{ee})} \tag{5.10}$$

To account for low statistics in the input histograms, the resulting functions have a coarser binning in m_{ee}, using

$$m_{ee} = \{65, 70, 75, 78, 80, 82, 84, 86, 88, 90, 92, 94, 96, 98, 100, 102, 105, 130, 250\}\,\text{GeV}.$$

The MC templates used for signal contamination and background fits are multiplied with the corresponding value of the reweighting function. This achieves mainly that the peaks in data and MC are matching better.

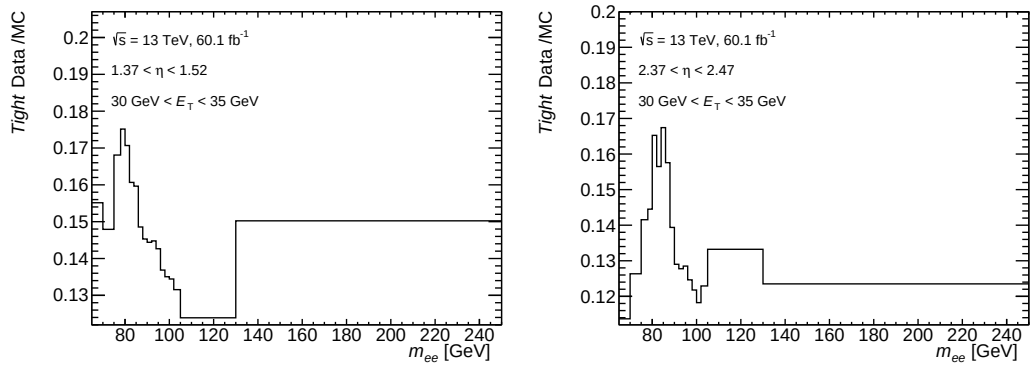

Figure 5.12: Two examples of reweighting correction functions as a function of m_{ee}. The left is gained in the transition region, while the right in an outermost eta bin. Both distributions show a peak structure below the Z mass, leading in a shift of the Z peak when applied to a MC distribution. The relatively high flat bin in the right plot results from low statistics and has no big effect on the result, since MC statistics is expected to be low in all applied histograms.

Figure 5.12 shows two examples of re-weighing functions as a function of m_{ee}, calculated in the same $\eta - E_T$ bin as the distributions shown in Fig. 5.11. The result of applying these functions on the raw MC signal templates (shown in fig. 5.11) is shown in fig. 5.13.

The procedure results in smoother background distributions as well as better data-MC agreement in the peak.

Applying this reweighting procedure leads to better fit results in the sense that the calculated χ^2/d.o.f. is lower for every bin of $\eta - E_T$. Fig. 5.14 shows the ratios of calculated χ^2/d.o.f. for fits with the reweighting function applied on MC to fits without these functions applied. In almost all bins, the ratio is smaller than 1, implying the method is resulting in a better description of the data. The procedure is used for all $\eta - E_T$ bins by default, because it is assumed that this procedure removes a possible bias from the MC generator.

Fig. 5.15 shows the corresponding absolute values of χ^2/d.o.f., using the default of the procedure, and thus also the re-weighting method. The values of

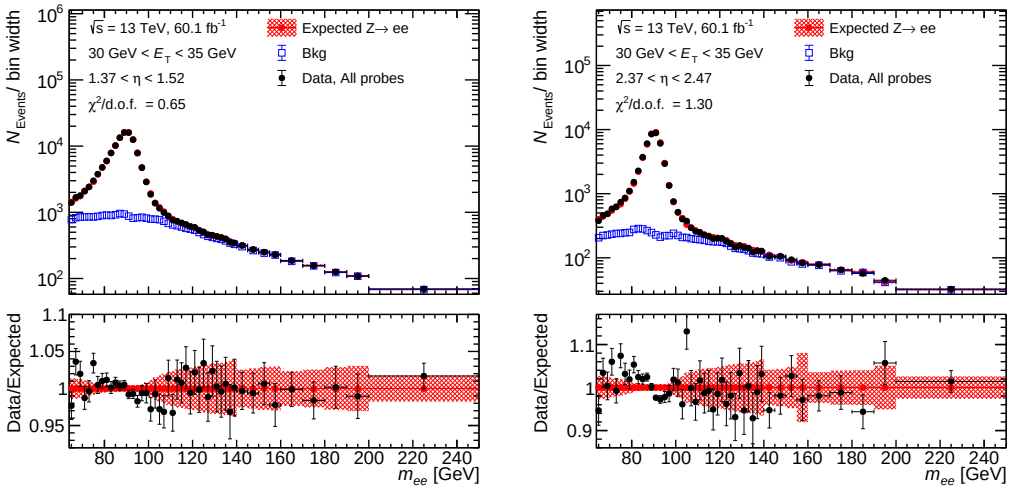

Figure 5.13: m_{ee} distributions in Z_{mass} with re-weighting correction is applied. The same data distributions as in Fig. 5.11 are shown. The functions, shown in Fig. 5.12 are applied to MC signal contamination and signal predictions. The resulting ratios, have improved drastically in the sense that the wiggles in the data/MC ratios are gone. Also the background template in the righthand plot is smoothed out now.

χ^2/d.o.f. are lower than 6 throughout the whole $\eta - E_T$ range, in average is even lower than 1, indicating excellent agreement of the predicted and measured denominator m_{ee} distributions.

Before introducing the re-weighting method, a rescaling method was tested as a shape MC shape variation for covering shape uncertainties of the tails. The basic idea of it was, to introduce linear reweighting functions, which are scaling up the low mass tail of the Z mass distribution with respect to the high mass tail and the peak. This linear function is defined as scaling up the 60 GeV bin in m_{ee} by s% while applying no scaling at 91 GeV. It was found that rescaling all MC distributions that way using a scaling factor of $s = 4\%$ leads to consistently lower values of the post-fit χ^2 , very similar to the results of the re-weighting technique. This implies that in fact there might be some bias from the MC shape. However, the re-weighting seems to be better motivated, since it is based on data. Therefore the method was disregarded with the choice of having the re-weighting applied as default.

Systematic variation As a systematic variation, the re-weighting method is not used, only using "raw" MC templates. This makes directly use of the first iteration of the method. The variation should cover the shape uncertainty estimated by

introducing the re-weighting method.

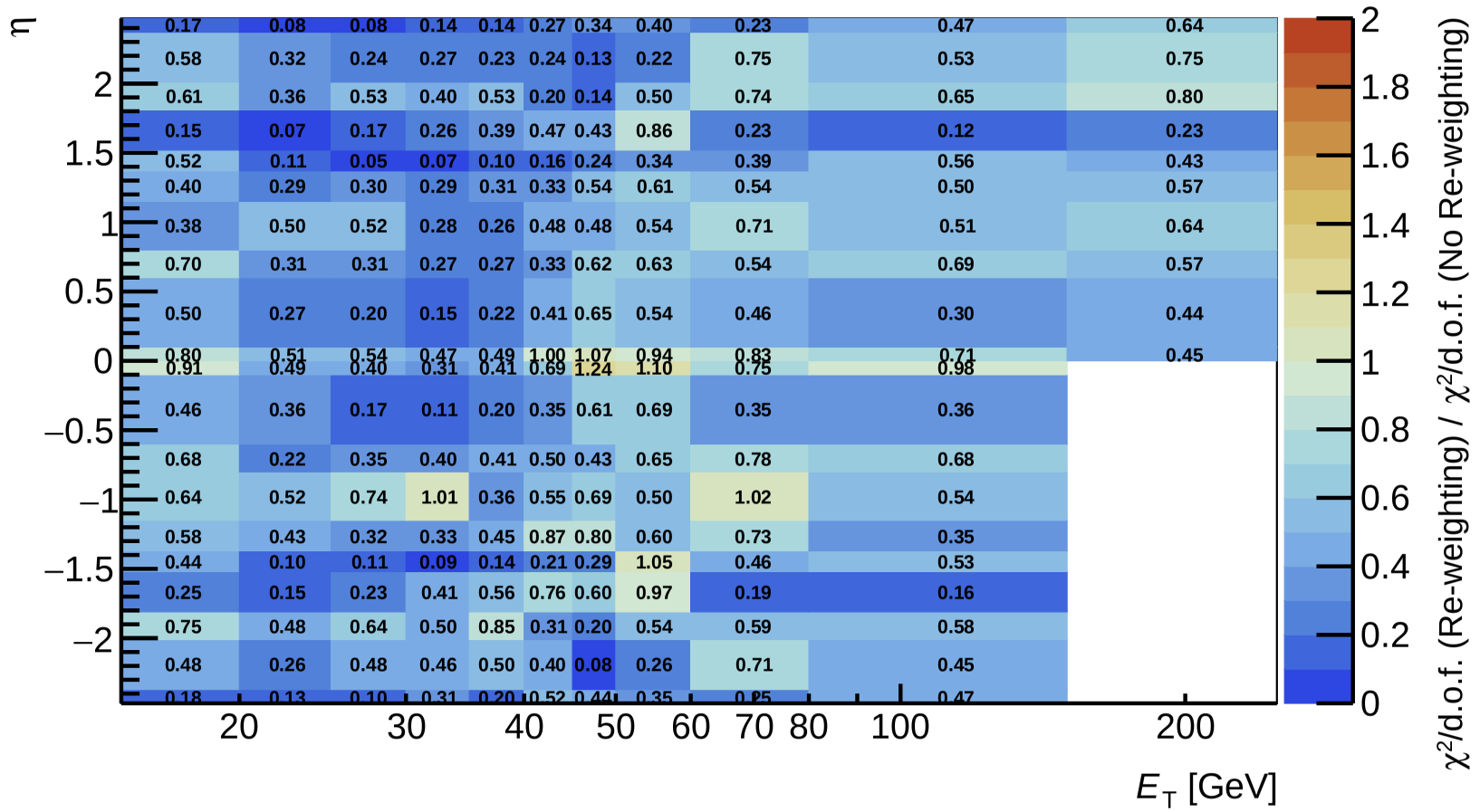

Figure 5.14: Ratio of the calculated post-fit χ^2/d.o.f of 2018 data and prediction when MC is not reweighted according to the text and when it is. The ratio is almost always smaller than 1.

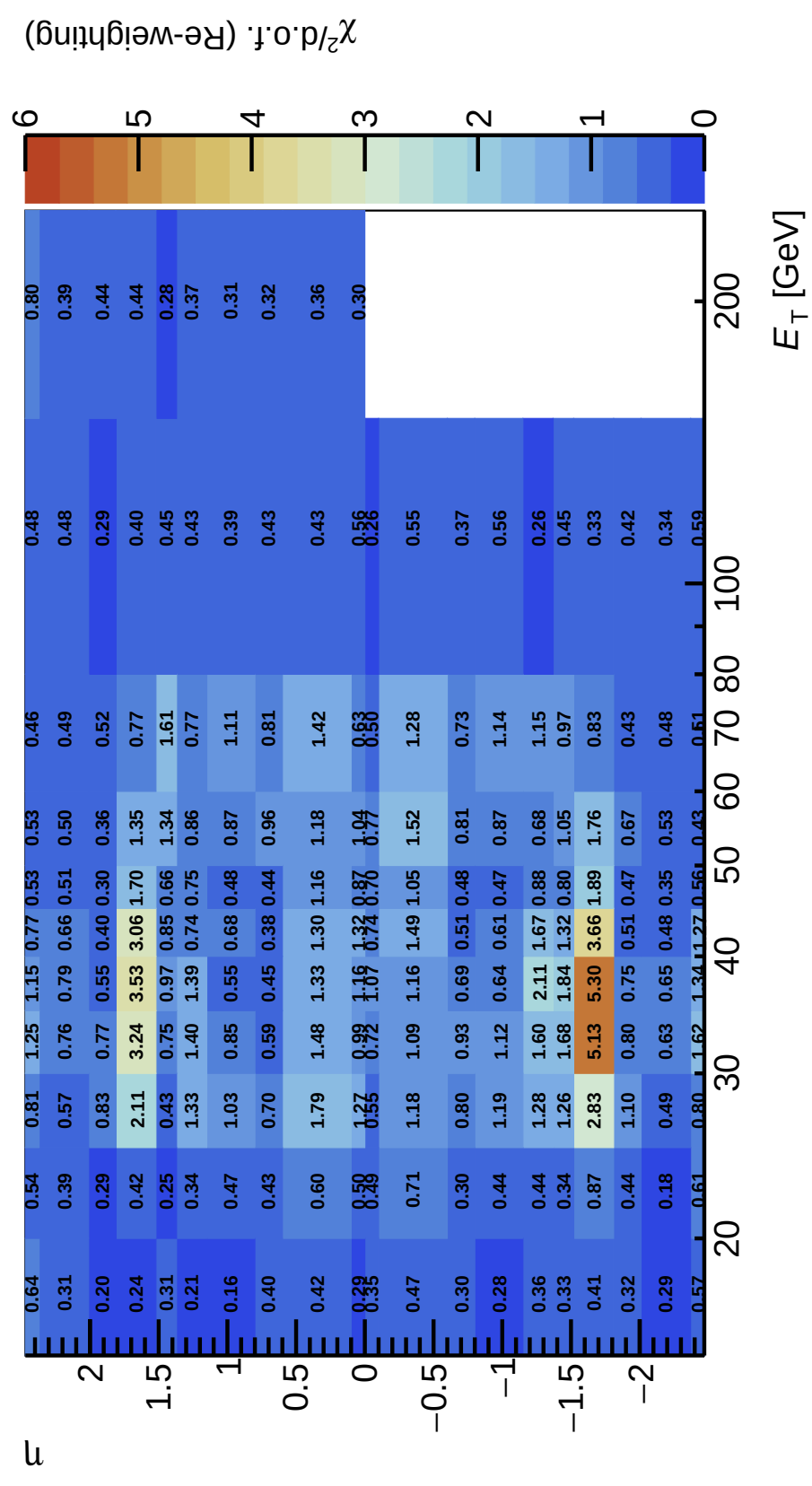

Figure 5.15: The calculated post-fit χ^2/d.o.f of 2018 data and prediction when MC reweighted according to the text. The presented method results in a very good agreement of predicted and measured in terms of χ^2/d.o.f for all $\eta - E_T$ bins.

5.3.5 Calculation of efficiencies and scale factors

The method described above is implemented as an algorithm looping over all bins of $\eta - E_T$. After the successful background estimate calculation finally the electron identification efficiencies can be calculated:

$$\varepsilon_{\text{data}}^{\eta,E_T} = \frac{\sum_{m_{ee}^{\text{down}}}^{m_{ee}^{\text{up}}} (N_{\text{data,probes pass id.}} - N_{\text{bkg,probes pass id.}})}{\sum_{m_{ee}^{\text{down}}}^{m_{ee}^{\text{up}}} (N_{\text{data,all probes}} - N_{\text{bkg,all probes}})} \tag{5.11}$$

The sums indicate, that the post-fit bins within the Z mass peak are integrated. The index id. is referring to the identification criteria. The default value for $m_{ee}^{\text{down}}, m_{ee}^{\text{up}}$ are 75 and 105 GeV, respectively. The calculation in MC is straight forward, since no background subtraction needs to be applied:

$$\varepsilon_{\text{MC}}^{\eta,E_T} = \frac{\sum_{m_{ee}^{\text{down}}}^{m_{ee}^{\text{up}}} N_{\text{MC,probes pass id.}}}{\sum_{m_{ee}^{\text{down}}}^{m_{ee}^{\text{up}}} N_{\text{MC,all probes}}} \tag{5.12}$$

Since in the end, no efficiencies are provided but SFs, these have to be calculated as the ratio of the efficiencies in the multiple bins of η and E_T:

$$\text{SF}^{\eta,E_T} = \frac{\varepsilon_{\text{data}}^{\eta,E_T}}{\varepsilon_{\text{MC}}^{\eta,E_T}} \tag{5.13}$$

The reason behind this is, SF can simply be applied to any electron from MC depending only on its η and E_T and independent of the signal process it was produced in. Bare efficiencies however can differ between processes.

The errors for data and MC efficiencies are calculated following [121], assuming correlated errors of the numerator and denominator:

$$\Delta\varepsilon_{\text{data/MC}}^{\eta,E_T} = \frac{\sqrt{(1 - 2\varepsilon_{\text{data/MC}}^{\eta,E_T})\Delta N_{\text{data/MC,Numerator}^2} + \varepsilon_{\text{data/MC}}^{\eta,E_T}\Delta N_{\text{data/MC,Denominator}}^2}}{N_{\text{data/MC,Denominator}}} \tag{5.14}$$

In here the integral over the m_{ee} bins is already assumed, thus ΔN is already referring to the statistical error for the full peak region in between $m_{ee}^{\text{down}}, m_{ee}^{\text{up}}$.

Finally the SF error is to be calculated as

$$\Delta\text{SF}^{\eta,E_T} = \text{SF}^{\eta,E_T}\sqrt{\left(\frac{\Delta\varepsilon_{\text{data}}^{\eta,E_T}}{\varepsilon_{\text{data}}^{\eta,E_T}}\right)^2 + \left(\frac{\Delta\varepsilon_{\text{MC}}^{\eta,E_T}}{\varepsilon_{\text{MC}}^{\eta,E_T}}\right)^2}\,. \tag{5.15}$$

Systematic variations: The size of the m_{ee} window is arbitrary, because there can not be given an exact lower and higher mass of the peak to be sure that the tag and the probe electron are in fact originating from a Z boson. Especially for lower E_T, there are contributions from $\gamma^* \rightarrow ee$ to the signal, making it difficult to choose a reasonable lower end of the mass window. To estimate the bias introduced by the window size, two window size variations are made.

- One variation reduces the window size such that $m_{ee}^{\text{down}}, m_{ee}^{\text{up}} = 80, 100\,\text{GeV}$.
- The other expands it to $m_{ee}^{\text{down}}, m_{ee}^{\text{up}} = 70, 110\,\text{GeV}$.

Total uncertainties

In order to estimate possible bias introduced from the described method, a systematic error has to be introduced and applied to the total error, which is calculated as

$$\Delta X_{\text{total}} = \sqrt{(\Delta X_{\text{syst}})^2 + (\Delta X_{\text{stat}})^2}\,, \tag{5.16}$$

where X is either the efficiency or the scale factor. In Eq. (5.16) the systematic error is calculated as the quadratic sum of errors arising from single error sources:

$$\Delta X_{\text{syst}} = \sqrt{\sum_{i \in \text{sources}} (\Delta X_i)^2} \tag{5.17}$$

The single error sources are targeting the single steps of the Z_{mass} algorithms and were already discussed above: The selection of tag electrons, the background selection, the signal contamination, the background fit and the m_{ee} window. For each error source systematic variations around a default were introduced. The systematic error of each source ΔX_i is calculated as from the envelope of all possible variations, to ensure the largest variation is covered by the uncertainty:

$$\Delta X_i = \max_{j \in \text{variations}} |X_{\text{default}} - X_j| \tag{5.18}$$

Figures 5.16, 5.17 and 5.18 show the data efficiencies calculated for the default configuration and for all variations of the different sources in transverse energy bins of $15-20$ GeV, $20-25$ GeV and $25-30$ GeV. In general the resulting uncertainties of each source lie within 2%.

In the two fit methods, usually the symmetric fit uncertainties (HESSE) variations are dominating the fit variations. However, in the $20-30\,\text{GeV}$ bins, the method is very sensitive to fit range variations. The resulting increased uncertainty reflects the difficulty to model the background correctly in these energy regions, because both variations are sensitive to the background shape. As a com-

parison for higher energy, Fig. 5.19 shows the same variations for $50 - 60$ GeV. Here, the results of systematic variation are fluctuating less because of decreased background in the low tail in m_{ee} of the Z_{mass} distribution.

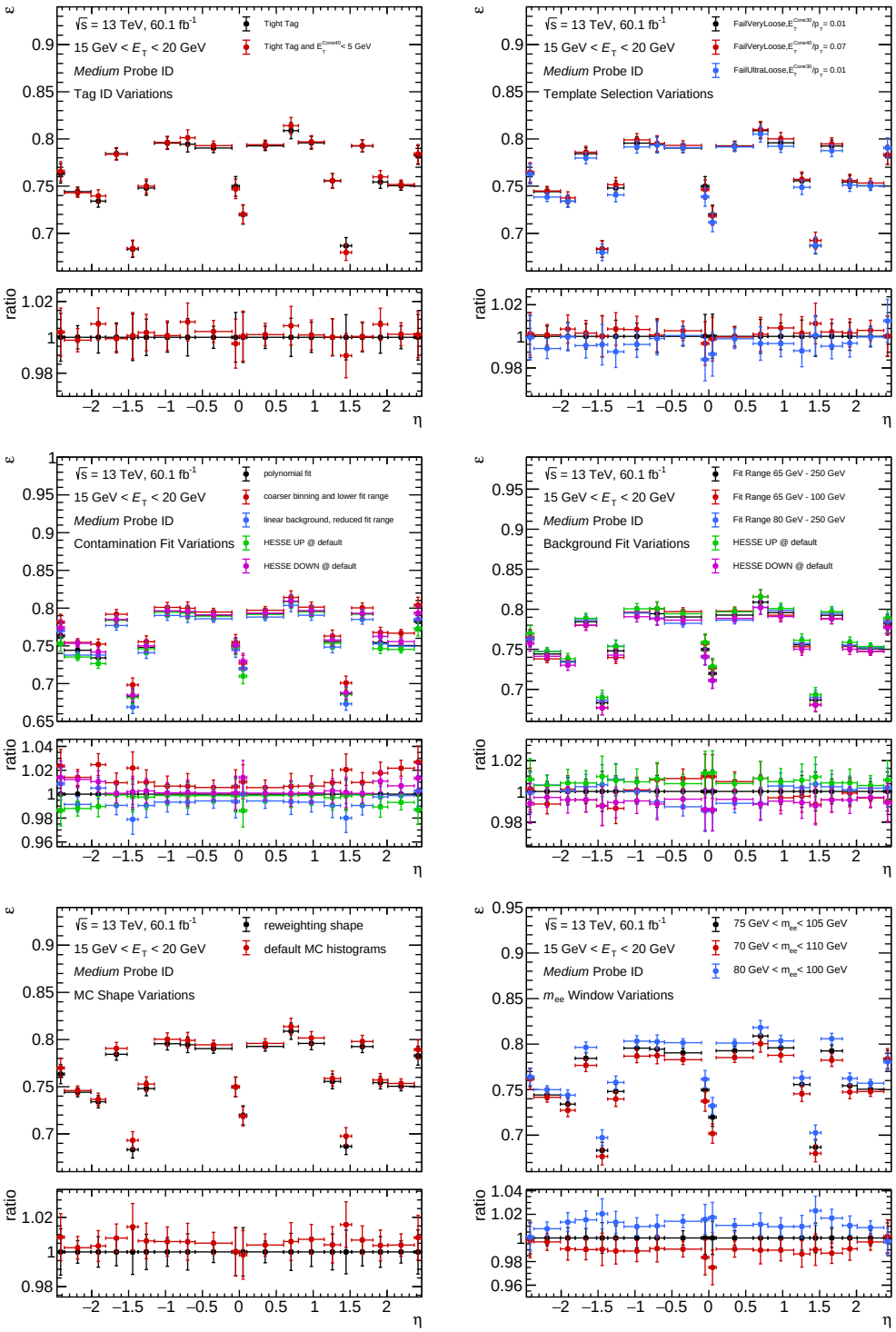

Figure 5.16: Data efficiencies $\varepsilon_{\text{data}}$ for the *Medium* working point of electron identification calculated as default and applying the various systematic variations for $15\,\text{GeV} < E_T < 20\,\text{GeV}$.

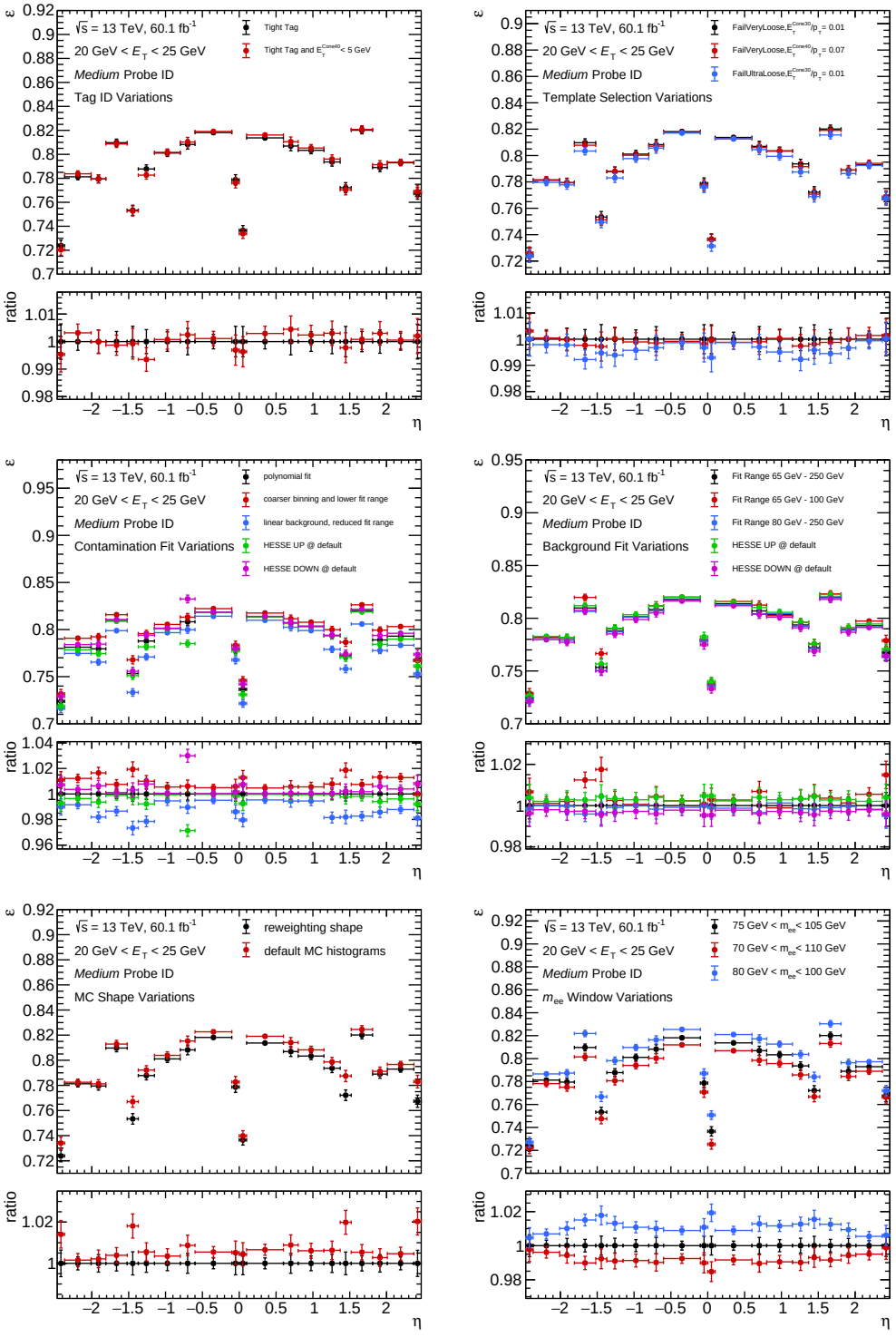

Figure 5.17: Data efficiencies $\varepsilon_{\text{data}}$ for the *Medium* working point of electron identification calculated as default and applying the various systematic variations for $20\,\text{GeV} < E_T < 25\,\text{GeV}$.

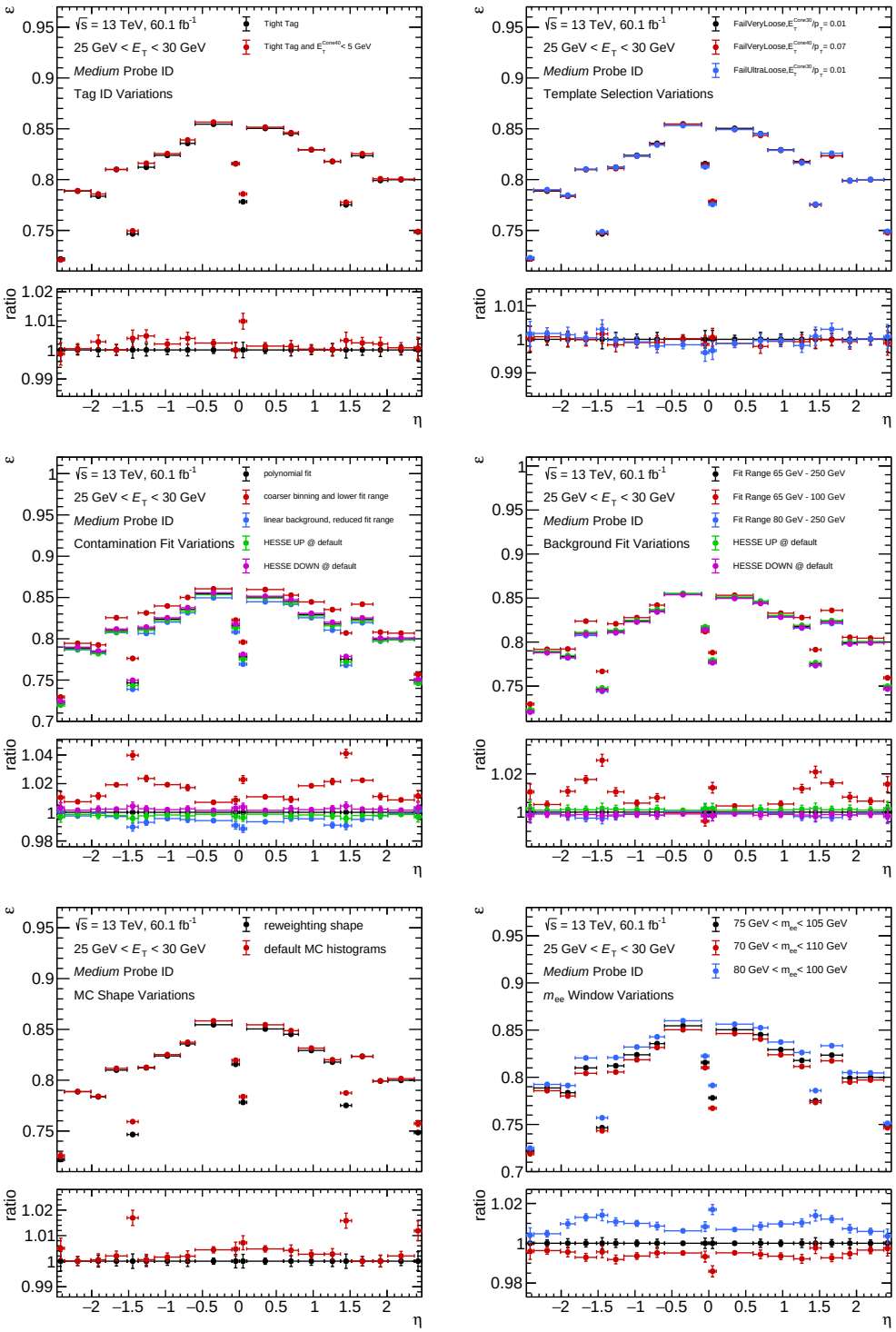

Figure 5.18: Data efficiencies $\varepsilon_{\text{data}}$ for the *Medium* working point of electron identification calculated as default and applying the various systematic variations for $25\,\text{GeV} < E_T < 30\,\text{GeV}$.

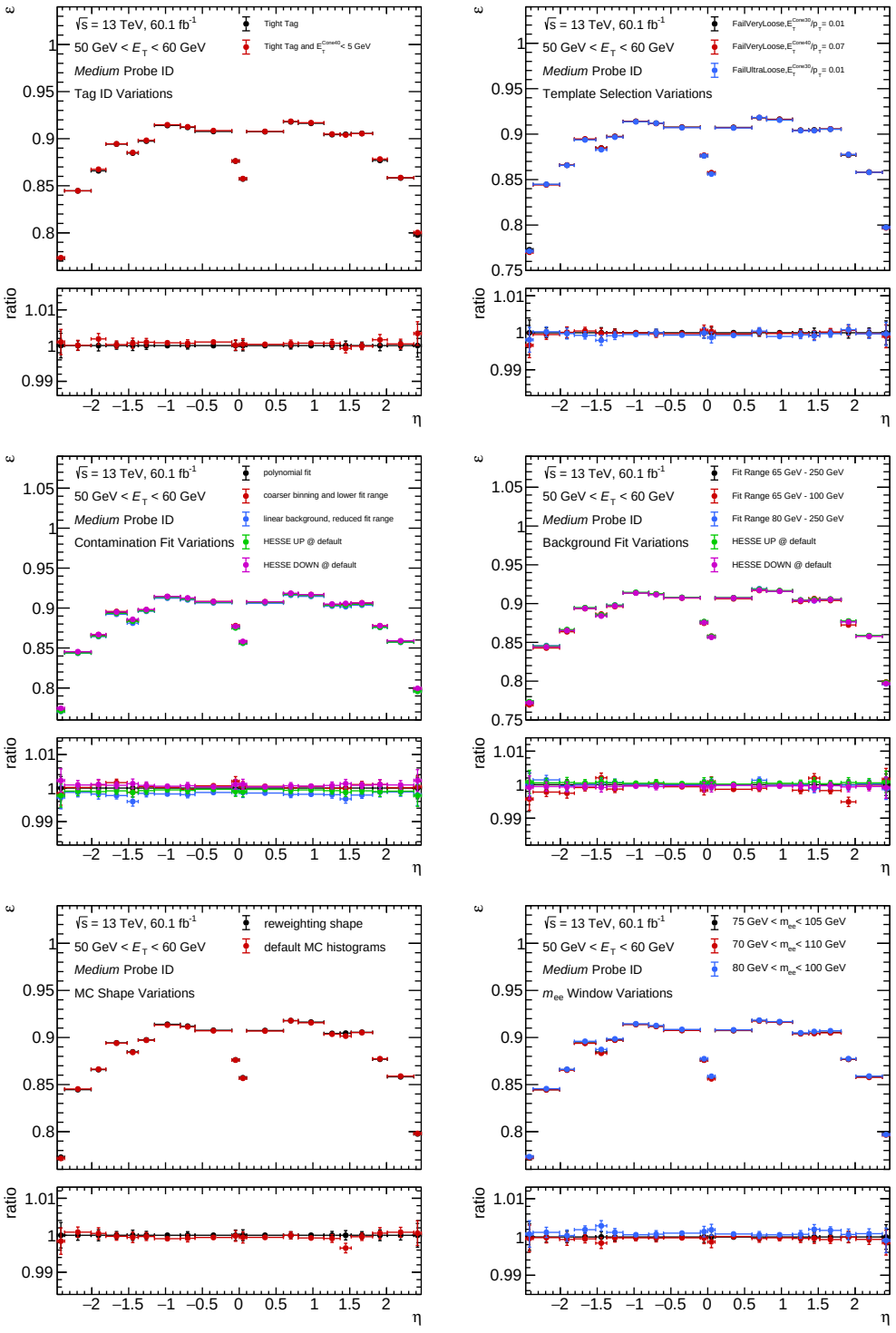

Figure 5.19: Data efficiencies $\varepsilon_{\text{data}}$ for the *Medium* electron identification working point of electron identification calculated as default and applying the various systematic variations for $50\,\text{GeV} < E_T < 60\,\text{GeV}$.

5.4 Results

Efficiencies and scale factors are calculated independently for each year of data taking. On the following pages data efficiencies, MC efficiencies and their scale factors in all bins of $\eta - E_T$ for the data-taking years 2015 (figures 5.20 and 5.21), 2016 (figs. 5.22, 5.23), 2017 (figs. 5.24, 5.25) and 2018 (figs. 5.26, 5.27) are shown as a function of η. In general scale factors are smaller than 1, indicating that data efficiencies are lower than MC efficiencies. The bottom last plot of the figures 5.21, 5.23, 5.25 and 5.27 shows the efficiencies as a function of E_T, calculated in an inclusive bin of $|\eta| < 2.47$. From these plots one can clearly see, that the efficiency rises with a higher transverse energy of the electron.

The sources of systematic uncertainty ΔX_i in data 2018 are summarised in the figures 5.28 and 5.29, as a function of η. In general they have the same magnitude. In some bins $E_T < 45\,\text{GeV}$ the dominating error source is most likely either the background fit range or the signal contamination estimate. The latter was not even considered as a source of systematic uncertainty in previous measurements.

Fig 5.30 shows the data and MC efficiencies, as well as the scale factors plotted versus the average number of interactions per bunch-crossing μ. MC efficiencies follow a linear trend calculated vs. μ. So do data efficiencies and scale factors, this can be interpreted as a hint, that the presented method is working reliably and gives reasonable results.

In some bins of high μ the data efficiency is higher than expected. This is due to background mis-modelling of the m_{ee} data histograms, where the probes have to pass the identification criteria. In these high-μ bins, this leads to an underestimation of the background. This is assumed to be correlated with the inclusive bin of $|\eta| < 2.47$ and E_T, respectively, since similar behaviour is seen in these bins with no special μ selection applied. Because the efficiencies vs. μ serve mainly a demonstration purpose and since the contribution of these events to the total event sample in Run-2 is negligible, this issue was not inspected further.

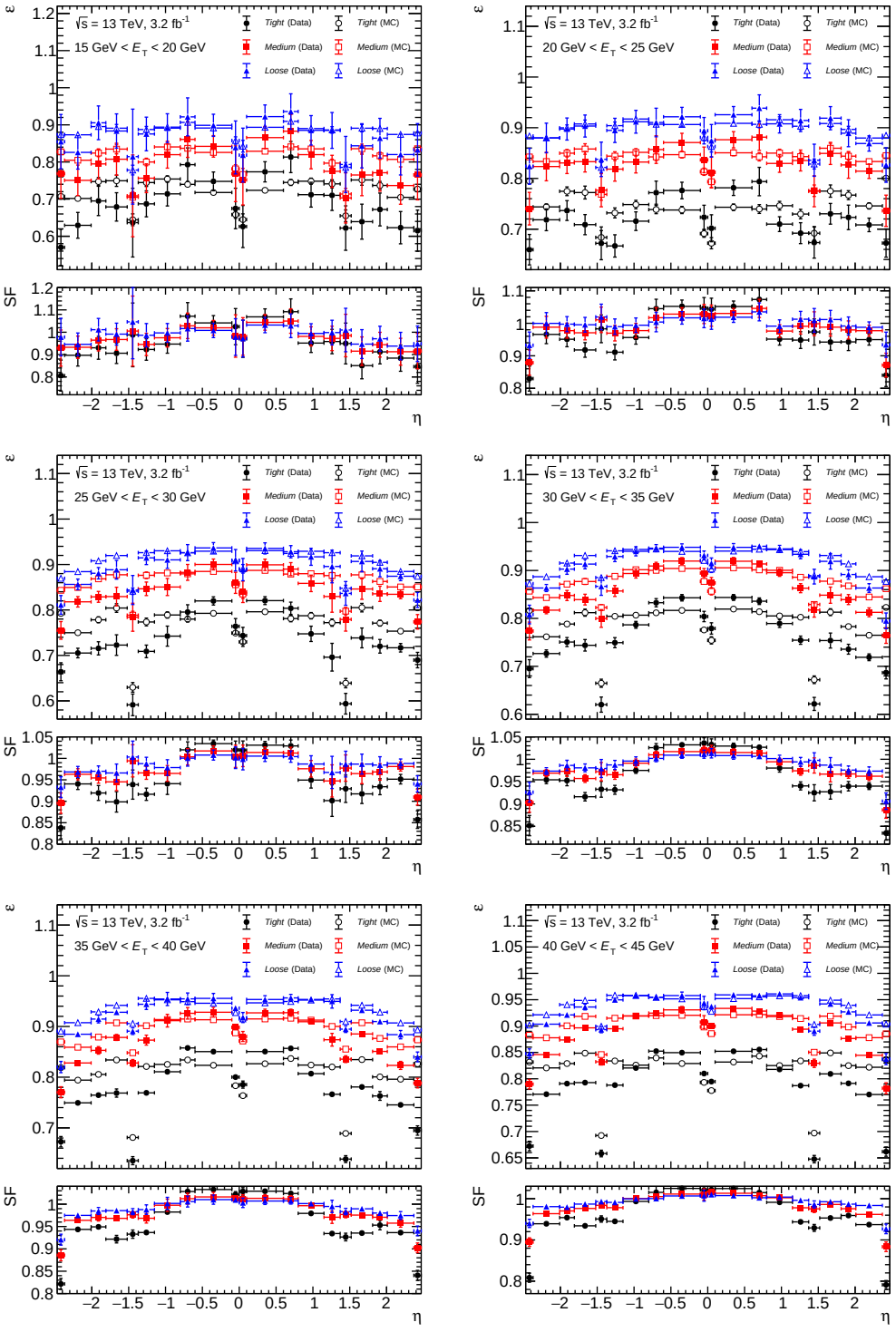

Figure 5.20: Z_{mass} efficiencies ε_{data} (filled markers), ε_{MC} (empty markers) and SFs (lower plots) using the 2015 dataset for 15 GeV $< E_T <$ 45 GeV. Efficiencies and SF are shown for *Tight* (black, circles), *Medium* (red, boxes) and *Loose* (blue, triangles) identification.

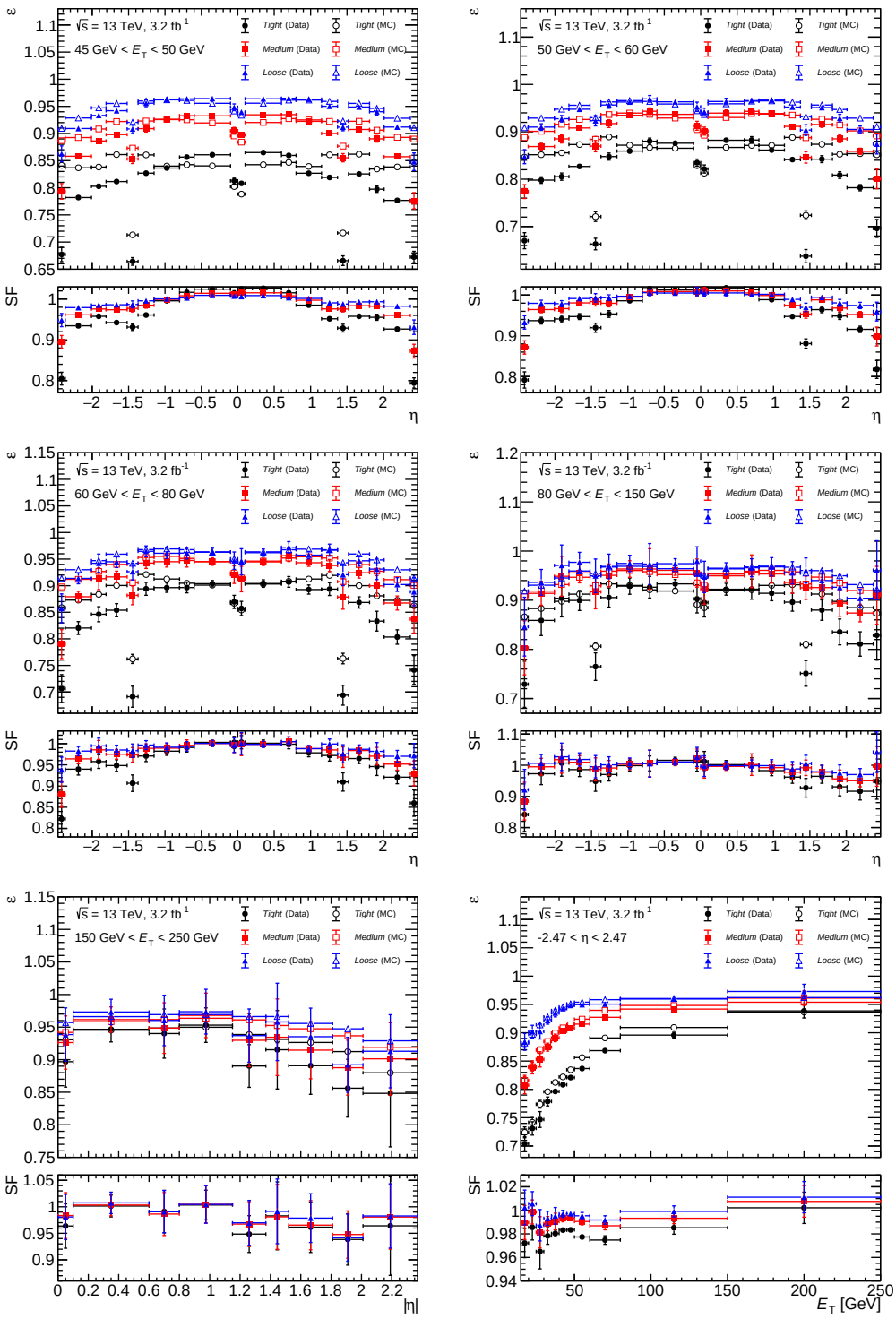

Figure 5.21: Z_{mass} efficiencies ε_{data} (filled markers), ε_{MC} (empty markers) and SFs (lower plots) using the 2015 dataset for $45\,\text{GeV} < E_T < 250\,\text{GeV}$. Efficiencies and SF are shown for *Tight* (black, circles), *Medium* (red, boxes) and *Loose* (blue, triangles) identification. The bottom right plot shows the efficiencies calculated in an inclusive bin of $|\eta| < 2.47$, projected against E_T.

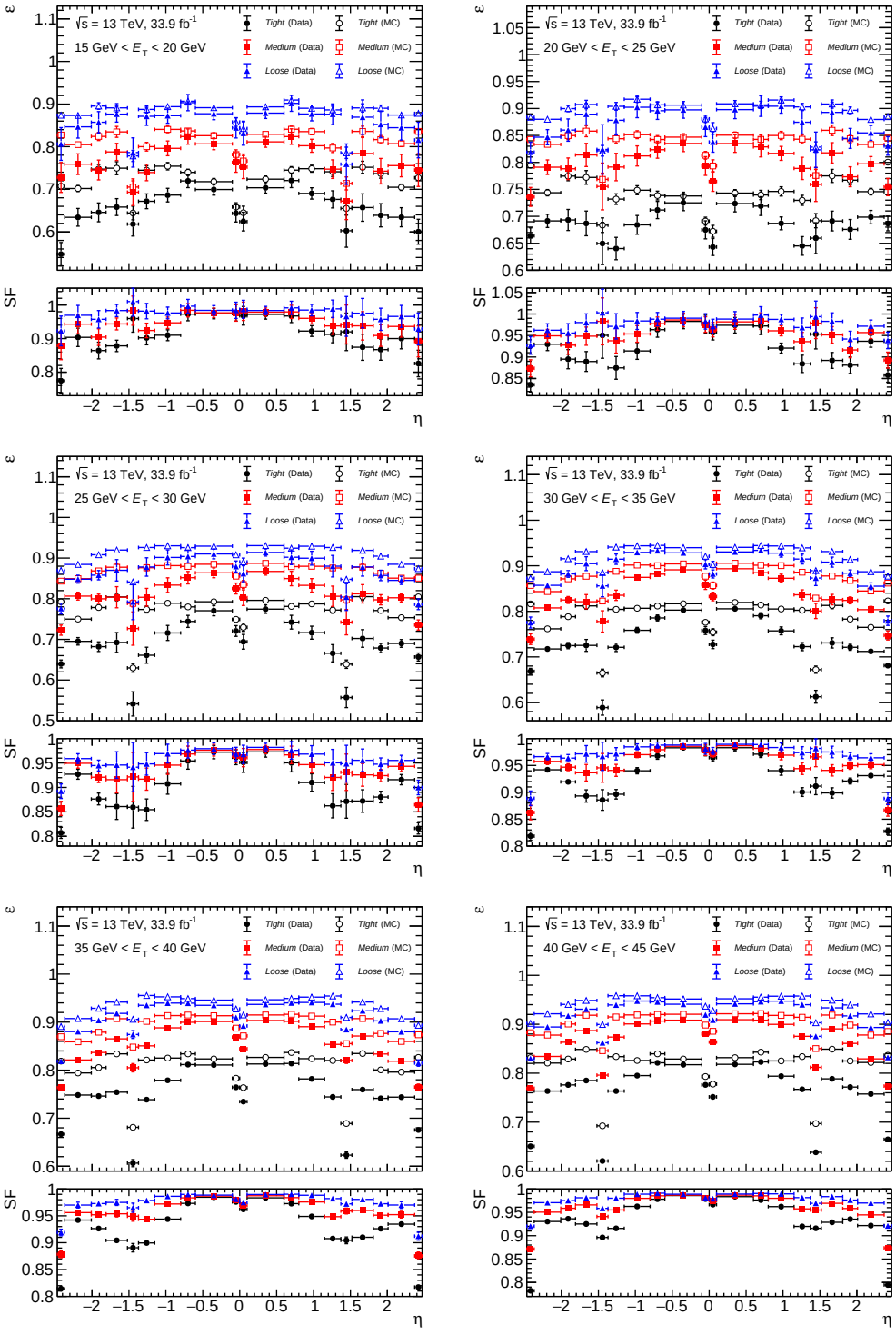

Figure 5.22: Z_{mass} efficiencies ε_{data} (filled markers), ε_{MC} (empty markers) and SFs (lower plots) using the 2016 dataset for 45 GeV $< E_T <$ 250 GeV. Efficiencies and SF are shown for *Tight* (black, circles), *Medium* (red, boxes) and *Loose* (blue, triangles) identification.

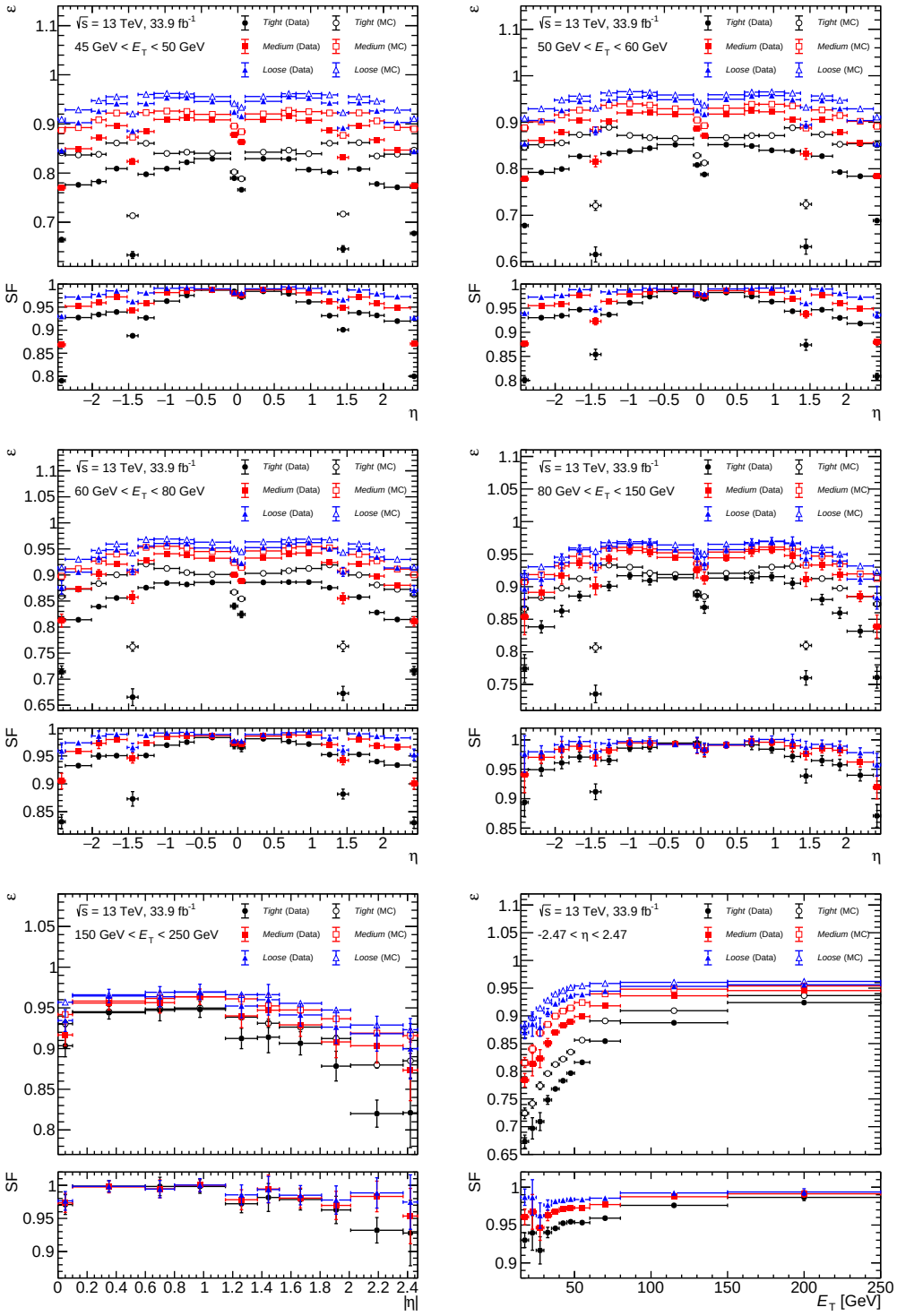

Figure 5.23: Z_{mass} efficiencies ε_{data} (filled markers), ε_{MC} (empty markers) and SFs (lower plots) using the 2016 dataset for $45\,\text{GeV} < E_T < 250\,\text{GeV}$. Efficiencies and SF are shown for *Tight* (black, circles), *Medium* (red, boxes) and *Loose* (blue, triangles) identification. The bottom right plot shows the efficiencies calculated in an inclusive bin of $|\eta| < 2.47$, projected against E_T.

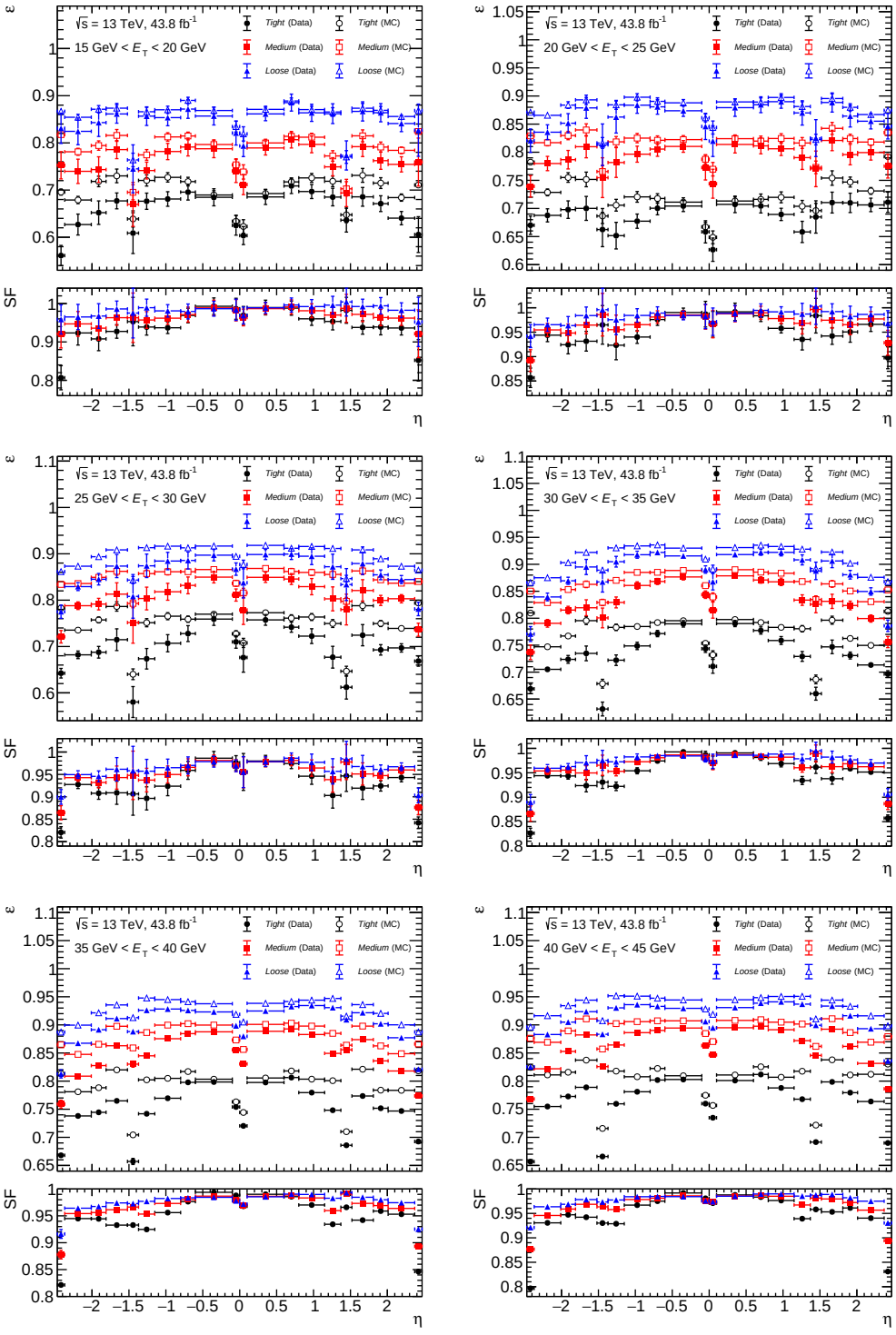

Figure 5.24: Z_{mass} efficiencies ε_{data} (filled markers), ε_{MC} (empty markers) and SFs (lower plots) using the 2017 dataset for 15 GeV $< E_T <$ 45 GeV. Efficiencies and SF are shown for *Tight* (black, circles), *Medium* (red, boxes) and *Loose* (blue, triangles) identification.

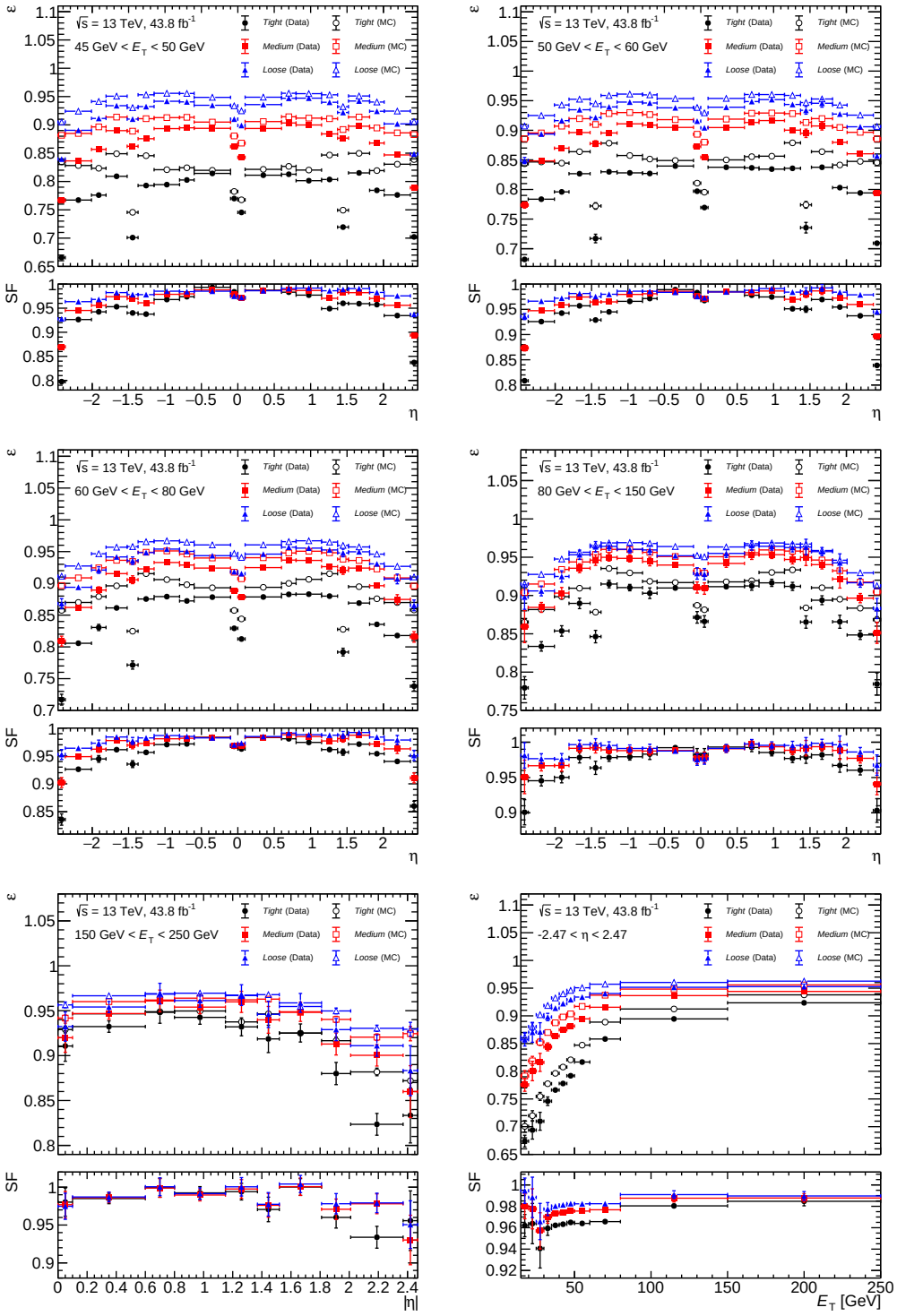

Figure 5.25: Z_{mass} efficiencies ε_{data} (filled markers), ε_{MC} (empty markers) and SFs (lower plots) using the 2017 dataset for $45\,\text{GeV} < E_T < 250\,\text{GeV}$. Efficiencies and SF are shown for *Tight* (black, circles), *Medium* (red, boxes) and *Loose* (blue, triangles) identification. The bottom right plot shows the efficiencies calculated in an inclusive bin of $|\eta| < 2.47$, projected against E_T.

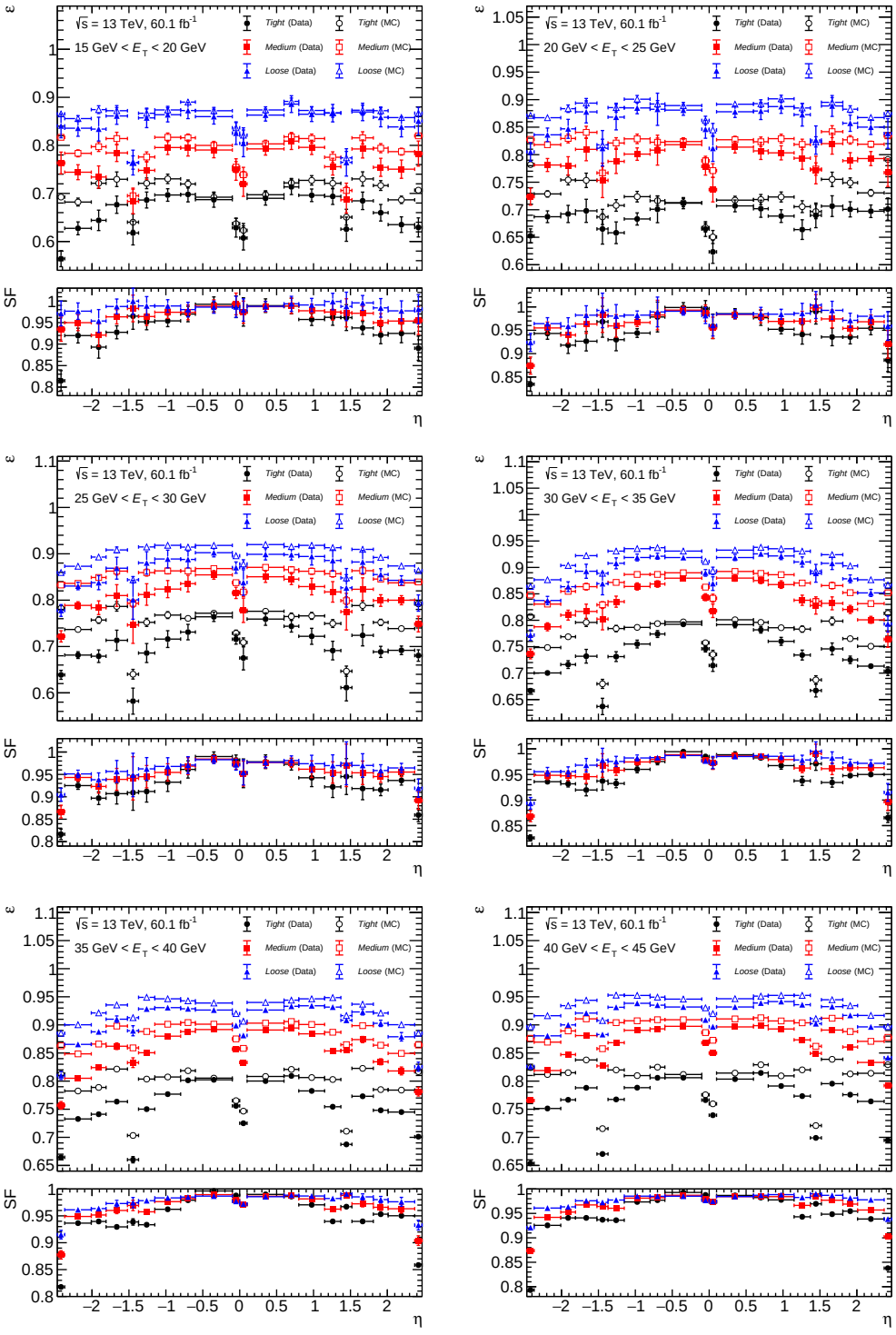

Figure 5.26: Z_{mass} efficiencies ε_{data} (filled markers), ε_{MC} (empty markers) and SFs (lower plots) using the 2018 dataset for 15 GeV $< E_T <$ 45 GeV. Efficiencies and SF are shown for *Tight* (black, circles), *Medium* (red, boxes) and *Loose* (blue, triangles) identification.

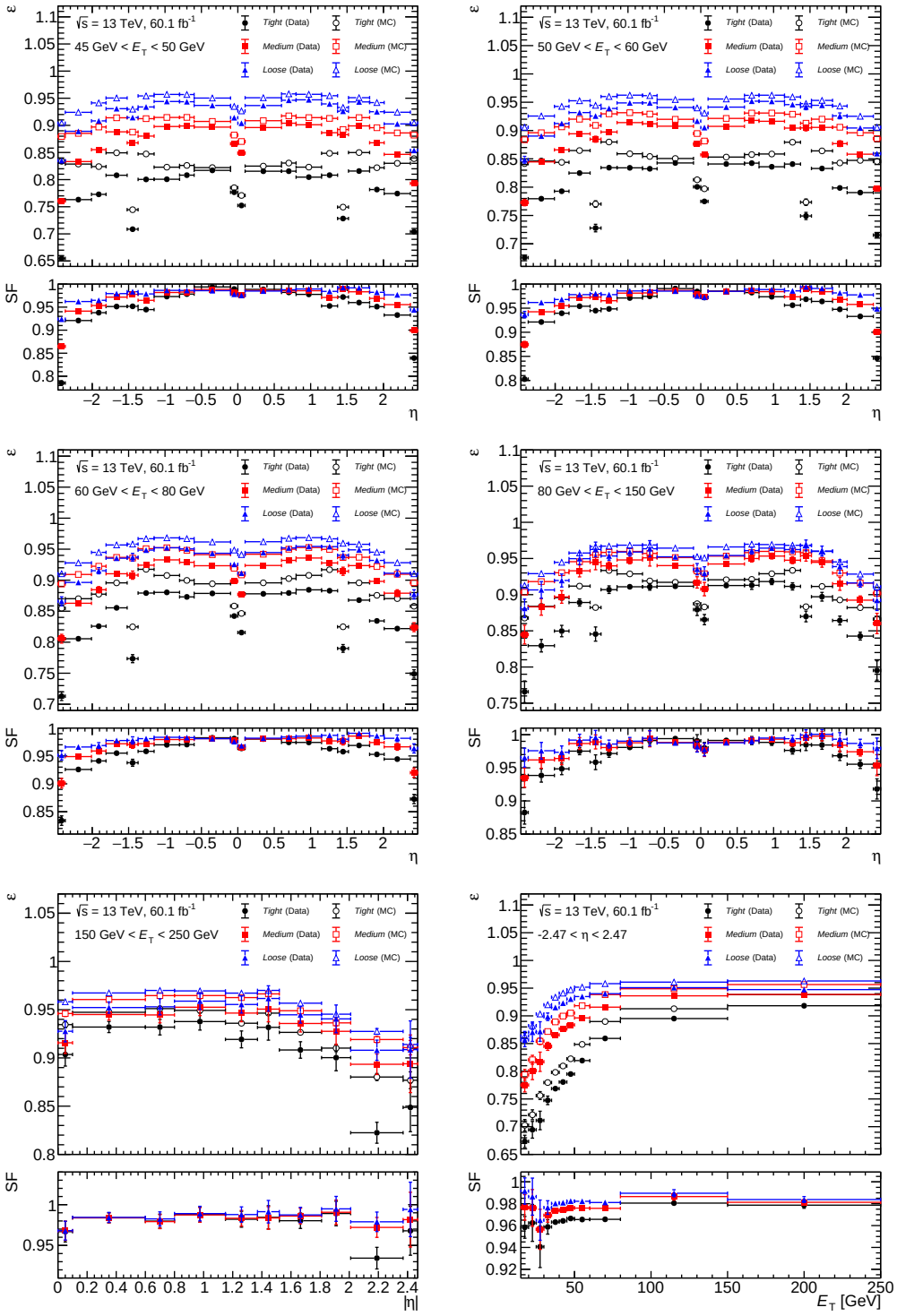

Figure 5.27: Z_{mass} efficiencies ε_{data} (filled markers), ε_{MC} (empty markers) and SFs (lower plots) using the 2018 dataset for $45\,\text{GeV} < E_T < 250\,\text{GeV}$. Efficiencies and SF are shown for *Tight* (black, circles), *Medium* (red, boxes) and *Loose* (blue, triangles) identification. The bottom right plot shows the efficiencies calculated in an inclusive bin of $|\eta| < 2.47$, projected against E_T.

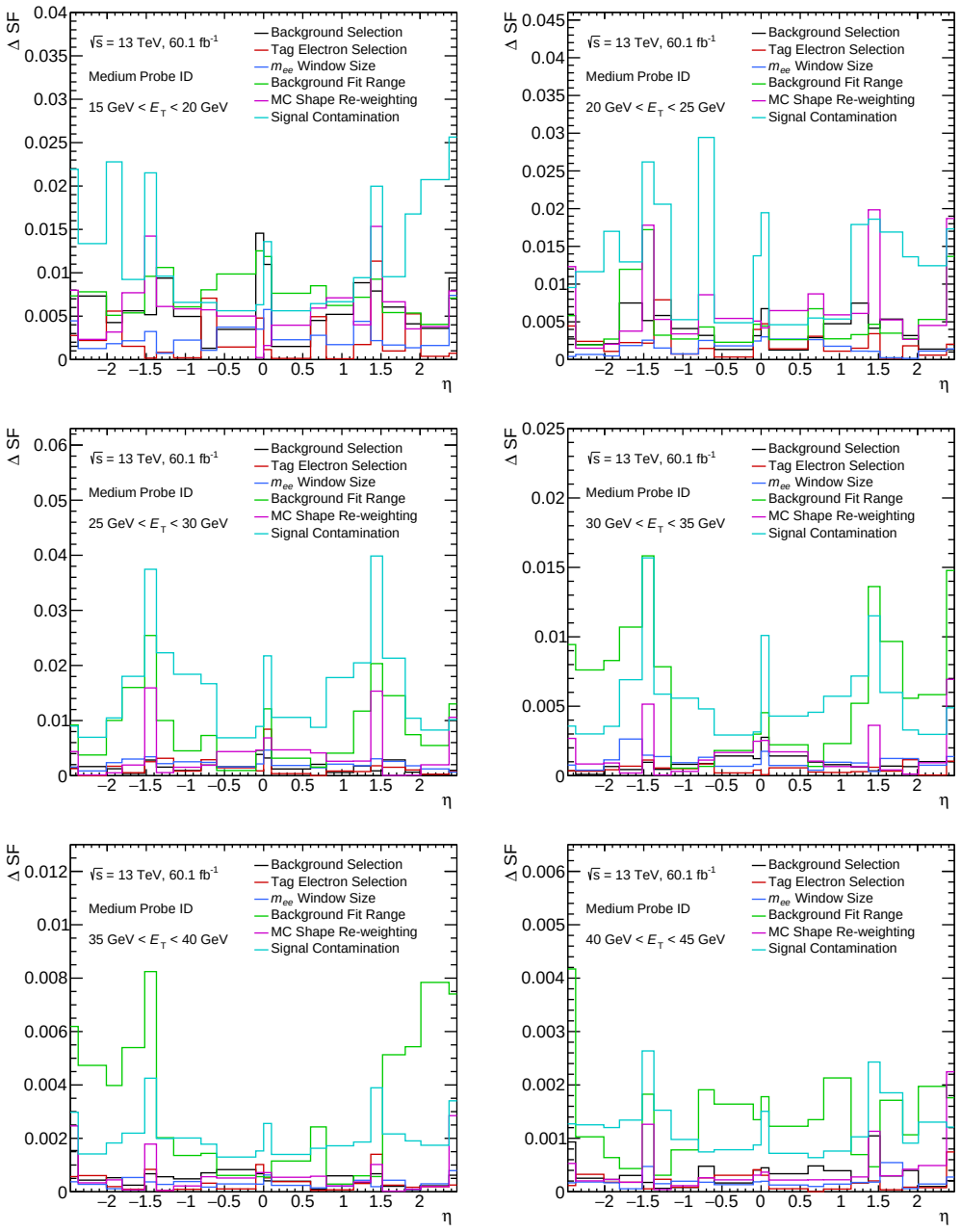

Figure 5.28: Z_{mass} sources of systematic uncertainties in 2018 SFs for $15\,\text{GeV} < E_T < 45\,\text{GeV}$. Each plot shows the uncertainty ΔX_i for each of the six sources of uncertainty as a function of η.

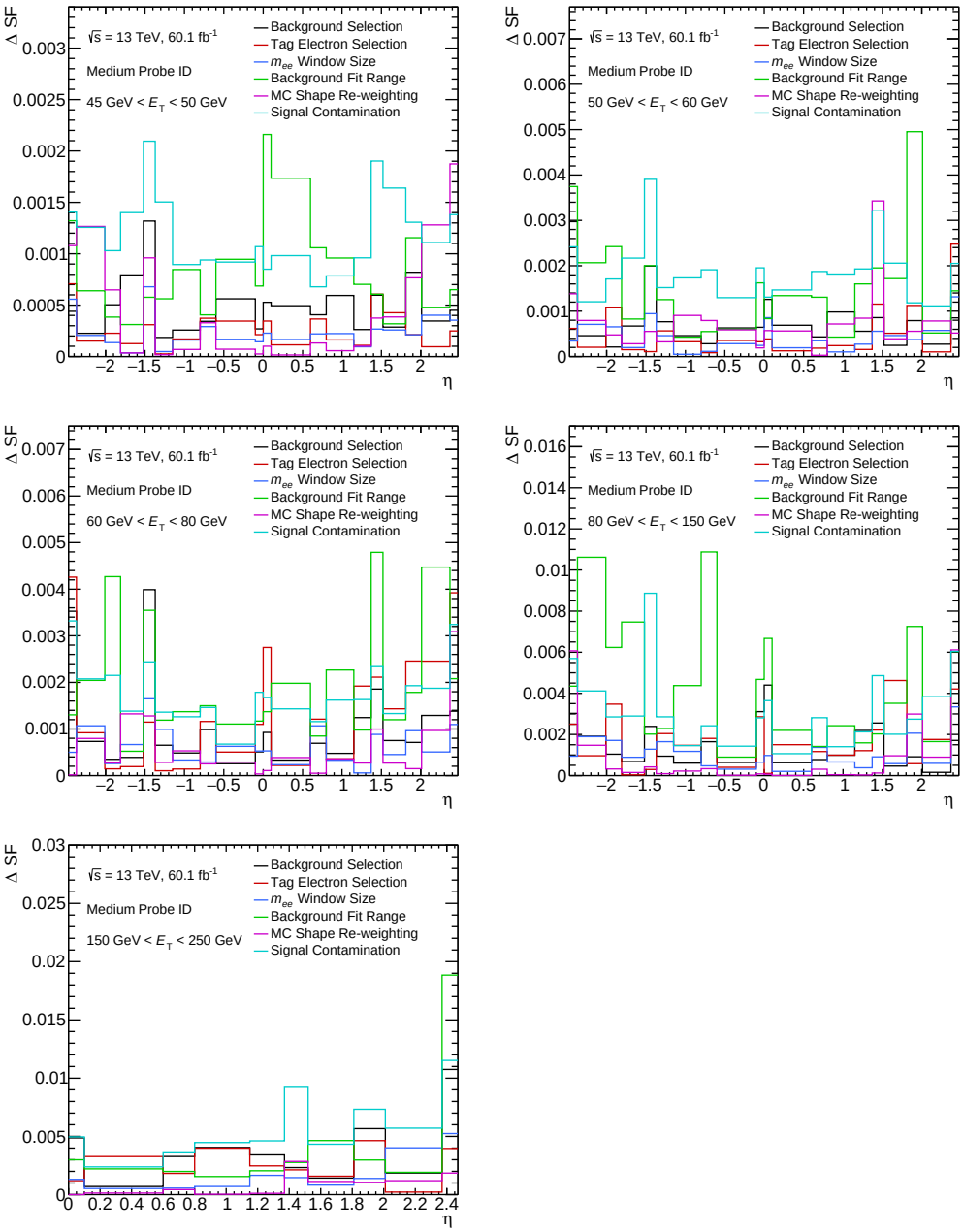

Figure 5.29: Z_{mass} sources of systematic uncertainties in 2018 SFs for $45\,\text{GeV} < E_T < 250\,\text{GeV}$. Each plot shows the uncertainty ΔX_i for each of the six sources of uncertainty as a function of η.

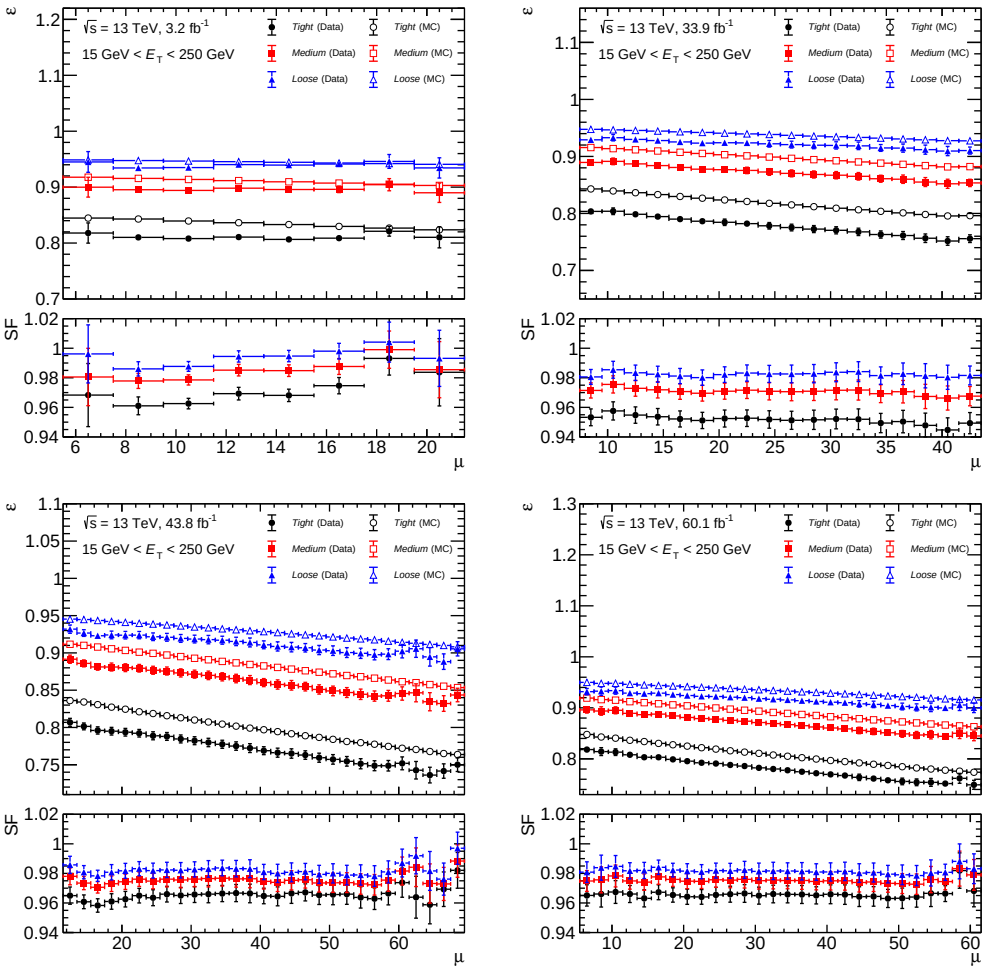

Figure 5.30: Z_{mass} efficiencies and SFs for the 2015, 2016, 2017 and 2018 datasets projected against the average number of bunch crossings μ calculated in a combined E_T bin. The identification efficiencies are shown for the identification working points *Tight* (black), *Medium* (red) and *Loose* (blue). The MC and data efficiencies show a very clear linear trend.

5.5 Conclusion

A method of calculating data efficiencies using a tag-and-probe method was presented. It makes use of the distribution of the tag-and-probe pairs around the Z mass peak, providing a clean sample of real electrons. The background is estimated using a data-driven method by inverting *Very Loose* likelihood identification cuts and in addition requiring non-isolated electron candidates. The resulting templates are cleaned from signal contamination using a simulated estimate of signal contamination. Finally the background is estimated by doing a template fit of the resulting clean data background sample and MC signal prediction to data. In order to reduce the bias which might be introduced by the MC template going into the background template fit, it is weighted to data, making use of *Tight* tag-and-probe mass distributions. The resulting efficiencies are presented for 2015, 2016, 2017 and 2018 data separately.

The update of the Z_{mass} measurement presented here has helped to improve the agreement between the Z_{mass} and the Z_{iso} method. Fig. 5.31 shows the scale factor results of Z_{mass} compared to the corresponding results from Z_{iso}. In addition, both are compared to Z_{mass} results provided for the Moriond 2018 conference [123], calculated using the old method published in Ref. [2]. The Z_{iso} method did not change as drastically since then and still gives similar results.

The discrepancies between the Z_{mass} and Z_{iso} methods are reduced significantly using the updated Z_{mass} algorithm presented in this thesis. Systematic errors in Z_{mass} are also reduced with respect to previous measurements in $E_T < 25\,\text{GeV}$, as well to the Z_{iso} method. For $E_T > 25\,\text{GeV}$ the errors actually increased with respect to 2018. For $25\,\text{GeV} < E_T < 35\,\text{GeV}$ this is taking account for the difficult background modelling in the corresponding bins. On top of that, the systematic error calculation changed, introducing error sources and also using the largest contribution in each source, leading to slightly higher systematic errors in bins with higher transverse energy. In general, the new Z_{mass} results show a lower total error than the Z_{iso} results.

Fig. 5.32 shows the final combination of Z_{iso} and Z_{mass} results, making use of the results calculated within this chapter. The measurements of the two methods are combined in a χ^2 minimisation. The statistical uncertainties of the probe electrons in the signal region in data and MC, and the systematic uncertainties stemming from the Tag identification and m_{ee} window size variations are correlated between the methods. Statistical uncertainties in the side bands and the background templates, and systematic uncertainties in the background estimation are treated as uncorrelated.

The previously mentioned increased Z_{mass} uncertainties in some bins are not leading to a worse combination result. This is in general improved, due to the better agreement of the two methods. The total error is reduced by at least 40%, in the lowest bins of E_T the error is reduced by a factor up to 70%.

Future methods could improve the measurement by including additional systematic variations targeting the composition of the background like hadrons or bremsstrahlung. Early studies in the context of this thesis were undertaken by using MC samples with additional simulated material inside the detector, resulting in higher bremsstrahlung. However, these kind of studies were not followed up further because of limited resources in terms of man-power.

Another idea is affecting the background subtraction estimate. It is not ideal, that the same distributions are used for measuring the efficiencies and estimating the background. Therefore a combination of the Z_{iso} and Z_{mass} methods is proposed, making use of each other as control region and unifying their background selection. This idea could be followed up by future students in the upcoming LHC Run-3.

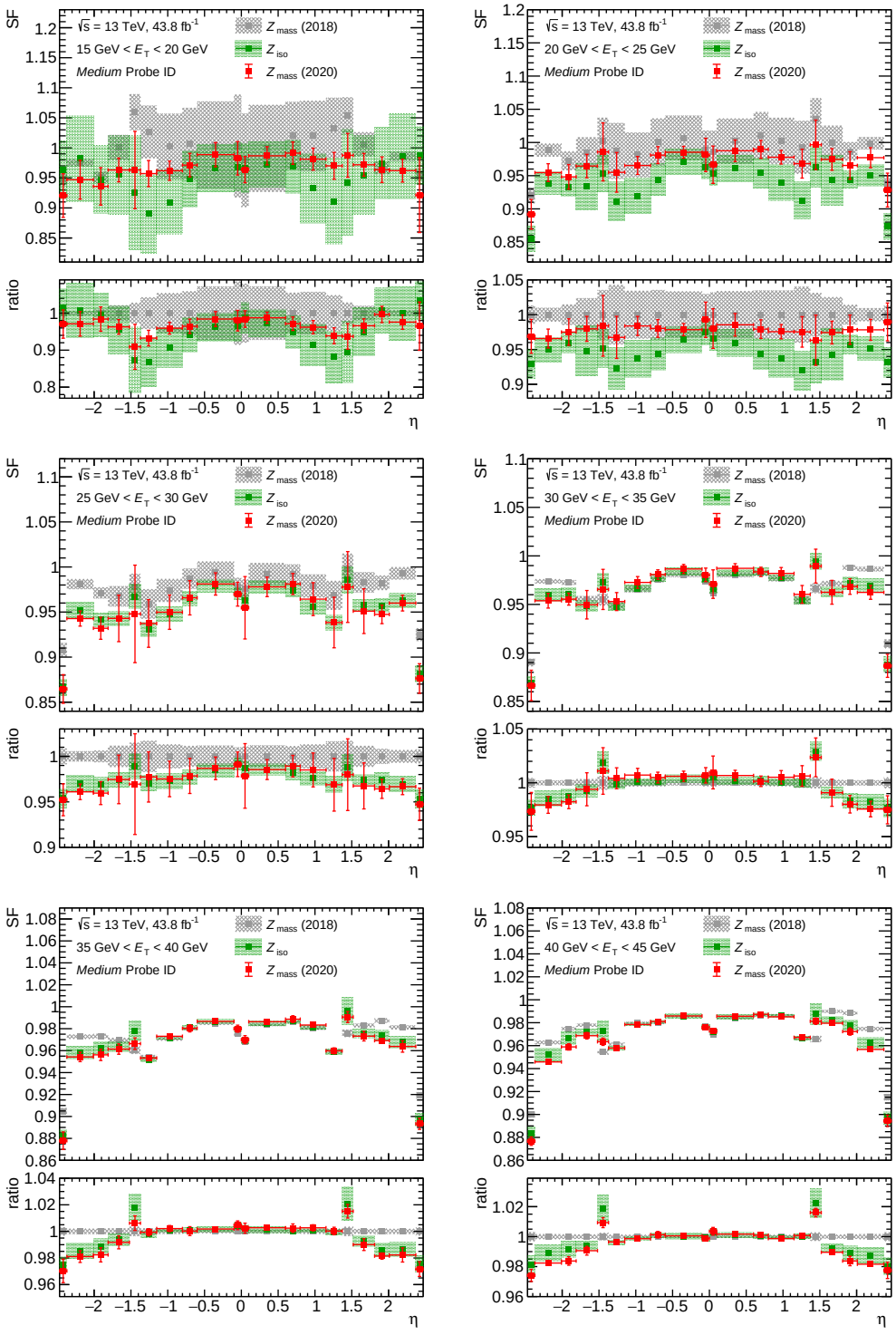

Figure 5.31: The resulting Z_{mass} SFs (labeled as Z_{mass} 2020) using the 2017 dataset in the range of $E_T = 15\,\text{GeV} - 45\,\text{GeV}$ for *Medium* probe identification requirements (red). In green, the corresponding Z_{iso} results are shown provided by Xiaowen Su [122]. Both are compared to Z_{mass} results from 2018, calculated using the old method published in Ref. [2].

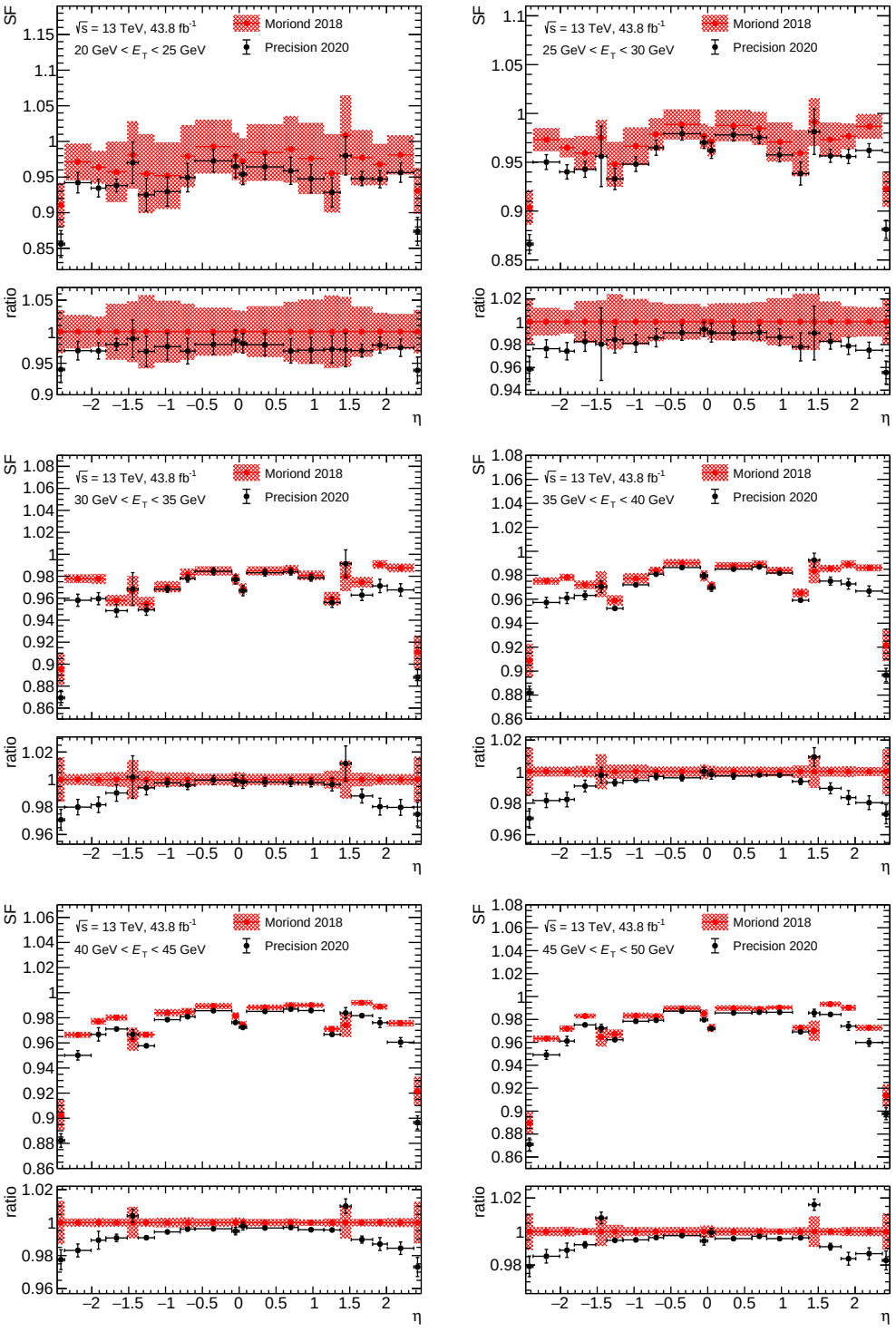

Figure 5.32: The SF recommendations for the *Medium* identification requirement, resulting from the combination of the Z_{mass} and Z_{iso} results, provided by Philip Sommer [124]. They are compared to the previous SF recommendations from 2018. The total error is reduced significantly in all bins of E_T. No statement can be made for $E_T < 20\,\text{GeV}$, since the required J/Ψ measurement was not available at the date of thesis submission.

Chapter 6

Measurement of the W^+W^- production cross section

The production of two heavy gauge bosons with opposite charge is a very interesting process to study at ATLAS. It gives an opportunity to measure some key properties of the SM, as discussed in Chapter 2. This chapter describes the first ATLAS measurements of differential W^+W^- production using 2015 and 2016 LHC data.

Authors contributions

The measurement has been published in Ref. [3]. This was a collaboration effort, therefore my personal contribution is pointed out here: The main contribution to the final result was the preparation of unfolding inputs, presented in Section **6.5 Unfolding and the differential cross section**. Further studies undertaken by me are targeting the background composition, these are presented in **6.4 Studies of the background composition**.

6.1 Overview

The W^+W^- cross section was measured using the ATLAS detector before, using the 8 TeV Run-1 dataset of 2012, determining total and differential cross sections as well as extracting limits on aTGCs [125]. aTGCs haven already been defined in Section 2.3. In Run-2 the total cross section was measured using 2015 data only [126].

The analysis described in Ref. [3], is the first differential measurement using 13 TeV Run-2 data, recorded in 2015 and 2016. The 2015+2016 dataset taken into account for this analysis is ten times larger in comparison to the 2015 analysis.

Taking into account the two times higher expected W^+W^- cross section at 13 TeV in comparison to 8 TeV, the dataset is effectively around three times larger than the 2012 dataset, hence it should be possible to improve the limits on aTGCs.

In general the cross section σ_{fid} is retrieved from number of observed data N_{observed} and the corresponding background estimate N_{bkg}:

$$\sigma_{\text{fid}} = \frac{N_{\text{observed}} - N_{\text{bkg}}}{C \times L} \quad , \tag{6.1}$$

where L is the integrated luminosity and C is a correction factor for detector acceptance and resolution. The measured cross section is valid only for the accessible phase space (instead of the total phase space), the so-called fiducial phase space, hence the index "fid". Tab. 6.1 lists the cuts defining the accessible phase space for the 2015+2016 measurement in this thesis and Ref. [3], the fiducial region (FR).

Table 6.1: Definition of the $WW \to e\mu$ fiducial phase space.

Fiducial selection requirement	Cut value
$p_T^{\ell\ell}$	> 27 GeV
$\lvert\eta_{\ell\ell}\rvert$	< 2.5
$m_{e\mu}$	> 55 GeV
$p_T^{e\mu}$	> 30 GeV
E_T^{miss}	> 20 GeV
Number of jets with $p_T > 35$ GeV , $\lvert\eta\rvert < 4.5$	0

The FR is defined at particle level, that is without any detector effects. Therefore, the particle level is also denoted as truth level. In addition one has to keep in mind, that at detector level usually selection cuts are applied in order to retrieve a signal enhanced dataset. This is why the factor $N_{\text{observed}} - N_{\text{bkg}}$ is measured in the so-called signal region (SR), which is defined by these selection cuts. The SR is defined at detector level, including all detector effects.

In the following Section 6.2 the event selection – and thus the SR – for this measurement is discussed in more detail. The selection requirements for the SR include quality cuts on the lepton candidate and are optimised to reduce the background. The remaining background has to be estimated carefully, as described in Section 6.3. One important background for this measurement is the background resulting from mis-identified leptons, the so called fake background. Studies on the composition of this fake background were undertaken and are presented in Section 6.4.

The final fiducial cross section is retrieved using a procedure called unfolding,

presented in Section 6.5. The final results and estimates on aTGCs are then presented in Section 6.6. The differential cross section measurements are carried out for 6 different observables.

6.2 Event selection

The SR is restricted to $e\mu$ final states, with the leptons having opposite charge. Even though this is only 8% of all possible W^+W^- production final states, it ensures a very clean signature. Same flavour states have more background from Drell-Yan (DY), while processes with hadronic final states have the problem of a high jet background at the LHC. The branching fraction BR of a W boson decaying into a lepton neutrino pair is measured to be

$$\mathrm{BR}(W^+ \to \ell^+ \nu_\ell) = (10.86 \pm 0.09)\% \,, \tag{6.2}$$

at the LEP experiments [38].

An overview of the SR is given in Tab. 6.2, while the following parts will discuss it further. All candidate events must have at least one primary vertex with

Table 6.2: Summary of lepton, jet, and event selection criteria for W^+W^- candidate events. In the table ℓ stands for e or μ. The transition region between end-caps and barrel ($1.37 < |\eta^e| < 1.52$) is excluded, because electrons can only be measured with worse resolution and efficiency due to a large amount of material present there.

Selection requirement	Selection value
$p_T^{\ell\ell}$	> 27 GeV
η^ℓ	$\lvert\eta^e\rvert < 2.47$ (excluding $1.37 < \lvert\eta^e\rvert < 1.52$), $\lvert\eta^\mu\rvert < 2.5$
Lepton identification	*Tight* (electron), *Medium* (muon)
Lepton isolation	*Gradient* working point
Number of additional leptons ($p_T > 10$ GeV)	0
Number of jets ($p_T >$35 GeV, $\lvert\eta\rvert <$4.5)	0
Number of b-tagged jets ($p_T > 20$ GeV, $\lvert\eta\rvert <$2.5)	0
E_T^{miss}	> 20 GeV
$p_T^{e\mu}$	> 30 GeV
$m_{e\mu}$	> 55 GeV

at least two associated tracks with a transverse momentum above 400 GeV. Further selection criteria are applied by the trigger selection, the quality of reconstructed

events and the background reduction.

A preselection of candidate events happens through the trigger selection. Two trigger types are used for recording: A single-muon trigger and a single-electron trigger. Both of them introduce a threshold on p_T and selection cuts on η. The p_T threshold varied during the data-taking periods, the minimal value for electrons was 24 GeV, while it was 20 GeV for muons. More than two thirds of the data taking happened with trigger threshold of $p_T > 26$ GeV for both lepton types. Electron and muon trigger efficiencies vary in η. Muons have a 70% efficiency in $|\eta| < 1.05$, and 90% for $1.05 < |\eta| < 2.4$, while electrons have a $> 90\%$ efficiency for $|\eta| < 2.47$ [127]. Leptons with $|\eta| > 2.47$ can not be recorded.

In addition to the primary triggers, additional triggers are applied to increase the total data taking efficiency up to 98.7%. This is made possible by increasing the p_T thresholds but loosening other properties like the isolation criteria.

Leptons need to originate from the primary vertex. The distance of the lepton track from the primary vertex along the z-axis times $\sin\theta$, $z_0 \times \sin\theta$, is required to be smaller than 5 mm. They need to satisfy isolation criteria using a *gradient* working point, which targets a fixed value of the isolation efficiency, and is dependent on the E_T of the electron but uniform in η [84, 128]. Muons need to be reconstructed with $p_T > 27$ GeV and $|\eta| < 2.5$ and the uncertainty of the impact parameter divided by the impact parameter itself needs to be $|\sigma_{d_0}/d_0| < 3.0$.

The electrons impact parameter significance needs to be at smaller than $|\sigma_{d_0}/d_0| < 5.0$. Electrons also need to satisfy the *Tight* identification criteria [128] and pass $p_T > 27$ GeV and $|\eta| < 2.47$ cuts, where the latter excludes the transition region $1.37 < |\eta| < 1.52$. Electrons stemming from photon conversions are reduced by removing events with electrons having an ambiguous reconstruction flag.

6.3 Background treatment and signal region

Background appearing within the SR can not be separated from signal like events, since it has exactly the same signature. In order to minimise the background contribution, further cuts targeting phase space regions dominated by the respective backgrounds are applied, defining the final SR which is listed in Tab. 6.2. The remaining irreducible background needs to be estimated using different methods, in order to get a grasp on the true signal yield. This is discussed in the following. The used estimation techniques can be found in more detail in Ref. [3]. Fig. 6.1 shows the feynman diagrams of some exemplary background processes discussed in the following sections.

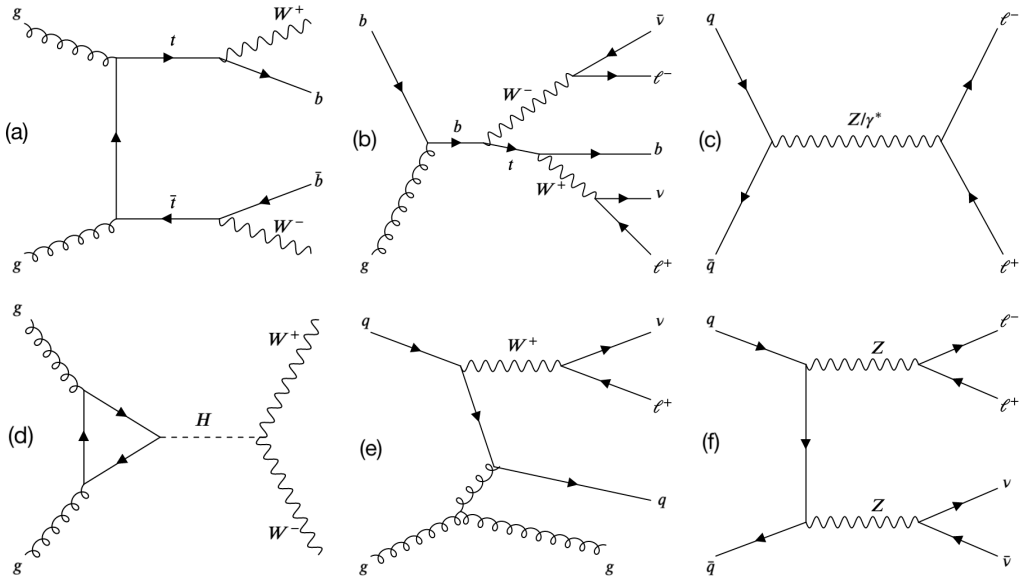

Figure 6.1: Feynman diagrams of background appearing within the W^+W^- SR. From top left to bottom right, as discussed in the corresponding Sections in the text: Top quark production (a: $t\bar{t}$, b: Wt), Drell-Yan (c), resonant Higgs production (d), W+jets (e), diboson (f: e.g. ZZ) production. It is assumed that W bosons are decaying into a lepton-neutrino pair, even if not drawn explicitly in the diagrams.

6.3.1 Top quark production

The main background source for W^+W^- production is top quark production, mainly through two mechanisms. The production of two top quarks leads to an instant decay of them into a W boson and a b jet each. The corresponding Feynman diagram is shown in Fig. 6.1 a. In addition single top processes (Fig. 6.1 b) leading to a top quark and a W boson have a similar signature. To suppress both of these backgrounds, events are required to have no jets with $p_T > 35$ GeV within $|\eta| < 4.5$, and no b-jets with $p_T > 20$ GeV and $|\eta| < 2.5$.

The so called jet-veto-survival-probability method [129] is used for estimating the irreducible top quark contributions. It extrapolates the contribution in the SR from a control region (CR) by estimating the probability of a top jet surviving the jet veto cut. This is done using MC and data estimates, leading to reduced modelling uncertainties.

Top quark processes constitute about 74 % of the total background in the SR.

6.3.2 Drell-Yan

A further important background is the production of two τ leptons through the DY process (Fig. 6.1 c). This can be effectively reduced by applying an $E_T^{\text{miss,track}} > 20\,\text{GeV}$ and a $p_T^{e\mu} > 30\,\text{GeV}$ requirement.

The DY background is estimated using MC simulation. The estimate is validated in a region being orthogonal to the SR, by inverting the $E_T^{\text{miss,track}}$ and $p_T^{e\mu}$ requirements. In this context, the term orthogonal means, that the regions do not share any common events by definition, by requiring the opposite cut on at least one observable.

The DY processes contribute by about 10 % to the total background.

6.3.3 Resonant Higgs

Contributions from Higgs boson decays (Fig. 6.1 d) can be reduced by expecting an invariant mass of $m_{e\mu} > 55\,\text{GeV}$ of the lepton pair. This reduces the $H \to WW^*$ contribution to a level below 1% of the expected signal. The $m_{e\mu} > 55\,\text{GeV}$ requirement is an inversion of the one used in the ATLAS 13 TeV measurement of $H \to WW^*$ production [130], making the two measurements statistically independent [3].

6.3.4 W+jets

Production of single W bosons and an associated jet or two jets with sufficient missing transverse energy can end up in the SR when the jets are mis-identified as leptons. An example Feynman diagram is shown in Fig. 6.1 e. These kinds of so-called fakes are hard to estimate via simulation, this can only happen using a data driven method.

The matrix method also described in Ref. [125] is used to estimate the W+jets and multi-jet backgrounds. The inputs of this method are the number of real and fake leptons passing either loose or *Tight* selection criteria, where the *Tight* criterion is on top of the loose. Further inputs are real lepton efficiencies and fake lepton mis-identification efficiencies. The real lepton efficiencies are calculated from leptons as a fraction of the number of leptons passing the *Tight* selection and the number of leptons passing the loose selection, similarly as in Chapter 5. Fake efficiencies are calculated using a fake enriched CR as the probability of a mis-identified hadronic jet passing the loose selection requirements for a lepton, to also pass the *Tight* selection requirements. The used CR is listed in Tab. 6.3.

In addition, as validation, the predicted contributions of W+jets background are validated using a same-sign validation region (VR), having the same definition

Table 6.3: Definition of the fake enriched CRs, used for fake efficiency calculation. It is applied to a data sample with only one triggered lepton. The alternate CR is used as a systematic variation of the fake estimate. Another systematic variation is targeting the sample composition by requiring exactly one *b*-jet in theCR, in the muon channel an additional d_0 requirement is used within this variation in order to enhance *c*-jet contributions. This is marked with a star * in the table.

Selection requirement	Selection value (CR)	Selection value (alternate CR)
m_T	< 40 GeV	< 20 GeV
$E_T^{\text{miss,track}}$	< 30 GeV	–
$m_T + E_T^{\text{miss,track}}$	–	< 60 GeV
$m_{e,\text{leadingjet}}$	outside $[95, 115]$ GeV	–
Number of additional leptons ($p_T > 10$ GeV)	0	
Number of jets ($p_T >$35 GeV, $\lvert\eta\rvert <$4.5)	$1-3$	$1-3$
Number of *b*-tagged jets ($p_T > 20$ GeV, $\lvert\eta\rvert <$2.5)	0 (1)*	0
$\lvert d_0^\mu/\sigma_{d_0^\mu}\rvert$	(> 1.0)*	–
$\Delta\phi$ between $E_T^{\text{miss,track}}$ and closest jet	< 2	–
$\Delta\phi$ between $E_T^{\text{miss,track}}$ and furthest jet	> 1.5	–

as the SR, with the exception that leptons are required to have the same electrical charge. The uncertainty of fake efficiencies is estimated, inter alia, varying the CR definitions, also listed in Tab. 6.3.

Using these inputs a set of four equations can be written down, which can be solved in order to estimate the number of events meeting the signal lepton selection criteria.

6.3.5 VV and VVV production

Further processes ending up in the SR are the production of two (VV) (e.g. Fig. 6.1 f) or more (VVV) vector bosons. These can be reduced by requiring the events not having an additional lepton with $p_T > 10\,\text{GeV}$ and passing *Medium* likelihood and the *GradientLoose* isolation requirement.

These backgrounds are estimated using MC predictions.

6.3.6 Signal yield and systematic uncertainties

Tab. 6.4 summarises the contributions of the signal and background processes to the SR. The number of events are expected to be 11930, with 7690 expected signal events. The table also summaries the statistic and systematic uncertainties.

The SR has a purity of about 73%, meaning 7690 out of the 12659 expected events are from W^+W^- processes.

Table 6.4: Number of events observed in data, compared to the numbers of predicted signal and background events in the signal region, taken from Ref. [3]. The systematic uncertainties do not include the uncertainty in the integrated luminosity. The uncertainties for the total background and the sum of signal and background are the quadratic sums of the uncertainties of the various background and signal sources.

	Number of events	Statistical uncertainty	Systematic uncertainty
$t\bar{t}$ and Wt	3120	$\pm$50	$\pm$370
DY	431	$\pm$13	$\pm$44
W+jets	310	$\pm$60	$\pm$280
WZ	290	$\pm$11	$\pm$33
ZZ	16	$\pm$1	$\pm$2
$V\gamma$	66	$\pm$11	$\pm$10
VVV	8	$\pm$1	$\pm$3
Total Background	4240	$\pm$80	$\pm$470
Signal ($W+W-$)	7690	$\pm$30	$\pm$220
Total Signal+Background	11930	$\pm$90	$\pm$520
Data	12659	$\pm$112	-

Systematic uncertainties on the signal and background predictions arise from the multiple estimates. Simulation uncertainties arise from detector uncertainties like PU and also from theory itself, when using different MC predictions. These uncertainties usually lie within a range of 10% to 20%. Compared to its total contribution to the SR, the W+jets background introduces the highest systematic uncertainty due to difficulty separating real prompt and misidentified electrons. The uncertainty on the estimate itself lies at the level of 90%. The uncertainties on the data driven top contribution estimates are about 12%. They arise from modelling in MC estimate, and from the choice of the control regions and other methodology choices. However, the greatest uncertainty in here stems from the b-tagging, being at a level of 9%.

Fig. 6.2 shows the measured data, the MC signal prediction as well as the discussed background estimates having SR requirements applied. In general data and prediction are in good agreement, indicating that background and signal is well understood. These control plots show distributions of the observables that are to be measured, discussed in more detail in Section 6.5.

The previous stated numbers in this Section were already published in Ref. [3], their retrieval was a collaboration effort of its analysis team.

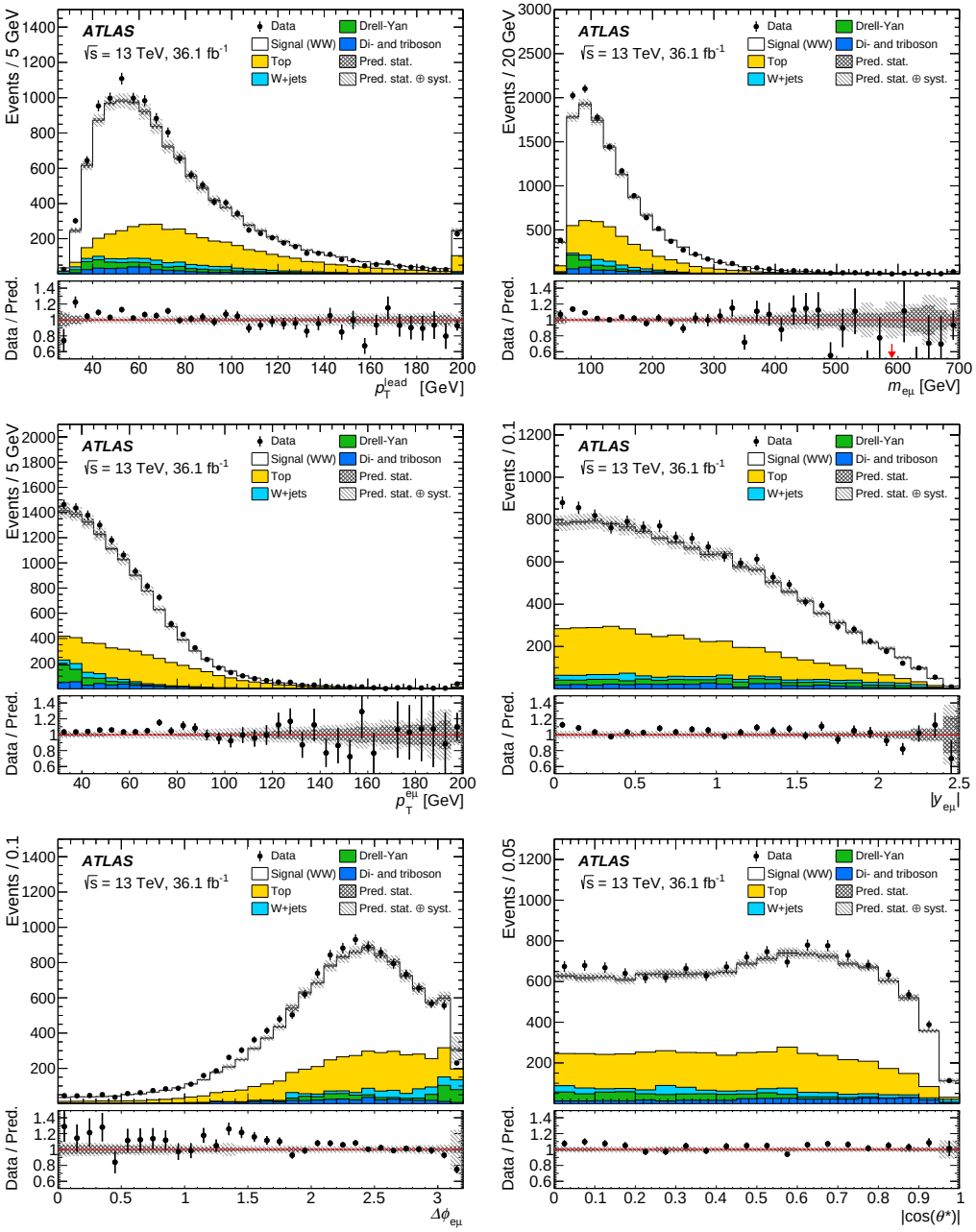

Figure 6.2: Signal region control plots of the W^+W^- cross section measurement, taken from Ref. [3]. Details are discussed in the text.

6.4 Studies of the background composition

Fakes can originate from hadrons, b-mesons, photons or other particles. Since the selection different types of fakes might be sensitive to the used control region, the measured efficiencies might be biased by the CR selection. In particularly, fake efficiencies are measured on events mainly having two fakes (di-jet events), because of usage of a fake enriched CR with real lepton contributions being subtracted. The fake-enriched control region has low transverse mass ($m_T < 40\,\text{GeV}$) and low missing transverse energy ($E_T^{\text{miss,track}} < 30\,\text{GeV}$) to reduce real lepton contributions, mainly from W/Z events. Further selection criteria are one triggered lepton and one to three jets. For calculating systematic uncertainties, the definition of the CR can be varied: One variation (the alternate CR) tightens the cut on the transverse mass ($m_T < 20\,\text{GeV}$) and uses a cut on the sum of transverse mass and missing transverse energy ($m_T + E_T^{\text{miss,track}} < 60\,\text{GeV}$). The full definition of the CR was already shown in Tab. 6.3.

However, the retrieved fake efficiencies are mainly applied to W+jet events, since they make up 99% of fake events in the SR. This might lead to a bias of the measurement due to the different fake contributions inside the CR and the SR: Fakes from di-jet events are more likely to be from light hadrons or photons, while the fakes from W+jets are more likely to stem from b- or c hadrons. Therefore, based on MC simulation, dedicated composition studies are performed. It should be noted that simulation can only provide a rough estimate, since it is statistically limited regarding fakes.

Two simulated samples were used for this study: A di-jet MC sample generated using Pythia8 [109] with A14 tune [131] and NNPDF23LO PDF set [115] and a W+jets sample generated using Sherpa2.2.1 [132].

On MC, the reconstructed leptons are matched via the hits in the simulation to the particles in the truth records that caused these hits. That way the type and the origin of a given fake lepton in the simulation can be determined. The muon and electron fakes are treated separately, since the efficiencies are also calculated separately.

To avoid counting real leptons as fakes in these studies, all leptons originating from W and Z bosons, as well as from tau lepton and top-quark decays, are not selected. Different selections are applied to the W+jets and di-jet samples, reflecting all selection cuts used in order to retrieve the fake estimate. Beside of the SR and same-sign VR definitions these are the previously defined fake enriched CR and the alternate CR shown in Tab. 6.3, as well as a further systematic variation with one b-jet. Thesame-sign validation region (VR) has the same definition as the

SR defined in Tab. 6.2, with the exception that leptons are required to have the same electrical charge.

Table 6.5 shows the composition of electron fakes for W+jets MC in SR and same-sign VR, and di-jet MC in various fake control regions. Overall, a good agreement between fake composition between SR (W+jets) and fake control regions (di-jets) is found. The largest contribution of electron fakes in the SR is coming from photon conversions.

Similarly, Table 6.6 shows the composition of muon fakes for W+jets MC in SR and same-sign VR, and di-jet MC in various fake control regions. The largest contribution of muon fakes in the SR is coming from charm decays.

However, charm decays are not represented equivalently in the di-jet sample. Therefore an additional study was performed on how to get a charm-enriched di-jet sample: By applying an extra transverse impact parameter cut for muons, $|d_0/\sigma_{d_0}| > 1.0$, on top of the 1 b-jet variation, the fraction of fakes from charm hadrons is increased to 87%. This is also listed in Table 6.6.

These results were important to check the validity of the fake estimate and its uncertainty in the analysis. The introduced $|d_0/\sigma_{d_0}|$ cut on top of the 1 b-jet variation was adapted for the systematic uncertainty calculation, since it helps to target explicitly the different charm contributions between the CR and the SR.

6.5 Unfolding and the differential cross section

As shown in Eq. (6.1), the fiducial cross section is retrieved from number of data events inside the SR N_{observed} and the corresponding background estimate N_{bkg}. The detector effects are summarised by a factor C in Eq. (6.1). It has to be noted, that the factor C also corrects the contribution of τ decays, which are not regarded as signal in this measurement. The contribution from τ lepton decays to the SR is estimated via a MC study to be 8.35%.

The detector effects summarised by the factor C have to be estimated and corrected to be able to extract the cross section.

6.5.1 Iterative Bayesian unfolding

Several effects can affect measured differential distributions [133]. First of all, every single bin can be affected by statistical Poison fluctuations. Furthermore finite detector resolution leads to migration between bins, e.g. the lepton p_T is reconstructed lower than its true value. In addition, the detector acceptance is not constant in the whole range of the variable distribution, leading to potential missing entries in a bin. A further effect is the non-linear detector response, leading to

Table 6.5: Comparison of electron fake composition in % for W+jets MC in SR and same-sign VR, and di-jet MC in various control regions. Main sources of electron fakes are pair production (photon conversion), decay of light mesons into electron pairs and a photon (Dalitz decays), and decays of charm or bottom hadrons. Unknown origin (non defined), can indicate direct mis-identification of particles like protons.

Truth origin	SR (W+jets MC)	CR (di-jet MC)	CR, $n_b = 1$ (di-jet MC)	alternate CR (di-jet MC)	same-sign VR (W+jets MC)
Photon conversion	73	65	44	45	66
Non defined	12	22	-	32	-
Dalitz decay	6	-	-	-	24
Charm hadron	5	6	18	9	2
Bottom hadron	3	7	38	13	1

Table 6.6: Comparison of muon fake composition in % for W+jets MC in SR and same-sign VR, and di-jet MC in various fake control regions. Main sources of muon fakes are the decay of heavy hadrons (charm, bottom), and the decay of pions or kaons. Unknown origin (non defined), can indicate direct mis-identification of particles like protons.

Truth origin	SR (W+jets MC)	CR (di-jet MC)	CR, $n_b = 1$ (di-jet MC)	CR, $n_b = 1 \wedge \lvert d_0/\sigma_{d_0}\rvert > 1.0$ (di-jet MC)	alternate CR (di-jet MC)	same-sign VR (W+jets MC)
Charm hadron	73	22	39	87	18	37
Non defined	18	43	-	-	46	49
Bottom hadron	-	27	61	13	34	13
Pion+kaon decay	8	9	-	-	2	-

shifts of average values, effects of this can be seen in the previous chapter, where the Z peak value changed with energy.

For differential distributions, the correction factor C often also changes as function of this distribution. This is specially the case, if events migrate between bins when going from the signal selection to the fiducial selection. To correct for the effects of detector resolution and efficiencies as function of the differential distributions that are to be measured, a so-called unfolding procedure is applied.

The differential cross section is measured in six different observables:

- The transverse momentum of the leading lepton p_T^{lead}.
- The transverse momentum of the di-lepton system $p_T^{\ell\ell}$
- The mass of the di-lepton system $m_{\ell\ell}$
- The rapidity of the di-lepton system $y^{\ell\ell}$
- The observable
$$|\cos\theta^*| = \left|\tanh\left(\frac{\Delta\eta_{e\mu}}{2}\right)\right| \tag{6.3}$$
This observable is sensitive to the spin structure of the lepton system [134].
- The difference of the polar angle of the two leptons $\Delta\phi^{\ell\ell}$.

The leading lepton is the lepton with the highest transverse momentum in the event.

The used method is an iterative Bayesian unfolding procedure [135, 136] which is also depicted on Fig. 6.3. The number of unfolded events N^j_{unfolded} in the bin j of the reconstructed distribution is retrieved via the equation

$$N^j_{\text{unfolded}} = \frac{1}{c^{\text{Rec},j}} \sum_{i=0}^{n_{\text{reco}}} \left[N^i_{\text{data}} - N^i_{\text{background}}\right] c^{\text{Res},i} P(N^j_{\text{reco}}|N^i_{\text{true}}), \tag{6.4}$$

where N^i_{data} is the number of data events in the ith bin of the distribution at particle level and $N^i_{\text{background}}$ the corresponding number of background events. c^{Rec} and c^{Res} are correction factors, the reconstruction efficiency and the resolution correction, respectively. The latter also can be called fiducial correction. $P(N^j_{\text{reco}}|N^i_{\text{true}})$ gives the Bayesian probability of measuring a certain number of reconstructed events N^j_{reco} given the number of actual events at particle level N^j_{true}. N^j_{reco} is the number of background subtracted data events:

$$N^j_{\text{reco}} = N^j_{\text{data}} - N^j_{\text{background}} \tag{6.5}$$

Eq. (6.4) can be seen as a matrix multiplication, the unfolded bin entries are retrieved from the reconstructed bin entries by multiplication with the matrix

$$P(N^j_{\text{reco}}|N^i_{\text{true}}) = \frac{P(N^i_{\text{reco}}|N^j_{\text{true}})P(N^j_{\text{true}})}{\sum_{j=0}^{n_{\text{true}}} P(N^i_{\text{reco}}|N^j_{\text{true}})P(N^j_{\text{true}})} \quad . \tag{6.6}$$

The factor written out in Eq. (6.6) is also called response matrix or unfolding matrix. By definition, it gives the probability of reconstructing N_{reco} events in bin j, given N_{true} events at particle level in bin i.

The unfolding procedure defined by Eq. (6.4) can be summarised as follows (also graphically shown in Fig. 6.3)

1. The background needs to be estimated and subtracted from a histogram of an observable X, resulting in a histogram with only signal events.

2. The resulting measured signal then is multiplied bin-wise with the resolution correction c^{Res}, this corrects for events reconstructed in the SR but are not actually part of the FR. This includes e.g. events stemming from τ decays.

3. The resulting histogram is then multiplied with the response matrix. This corrects for migration effects.

4. The resulting histogram of the previous step is then multiplied bin-wise with the reconstruction efficiencies c^{Rec}. This corrects for reconstruction losses.

Disregarded in this list is the estimate of the so-called prior $P(N_{\text{true}})$, the initial probability of the true distribution. This is in general model dependent, therefore the method is iterated, with the prior updated after each iteration with the unfolding result of the previous iteration.

In simulation, both, the objects reconstructed in the detector as well as the physical particles they originate from are accessible, allowing to use the simulation to create the correction factors c^{Rec} and c^{Res}, the response matrix as well as the prior.

6.5.2 Inputs of Bayesian unfolding

The described iterative Bayesian unfolding requires four inputs from W^+W^- signal MC predictions, listed in the following.

The resolution correction The resolution correction denominator is defined by all reconstructed events passing the SR requirements listed in Tab. 6.2. In case of

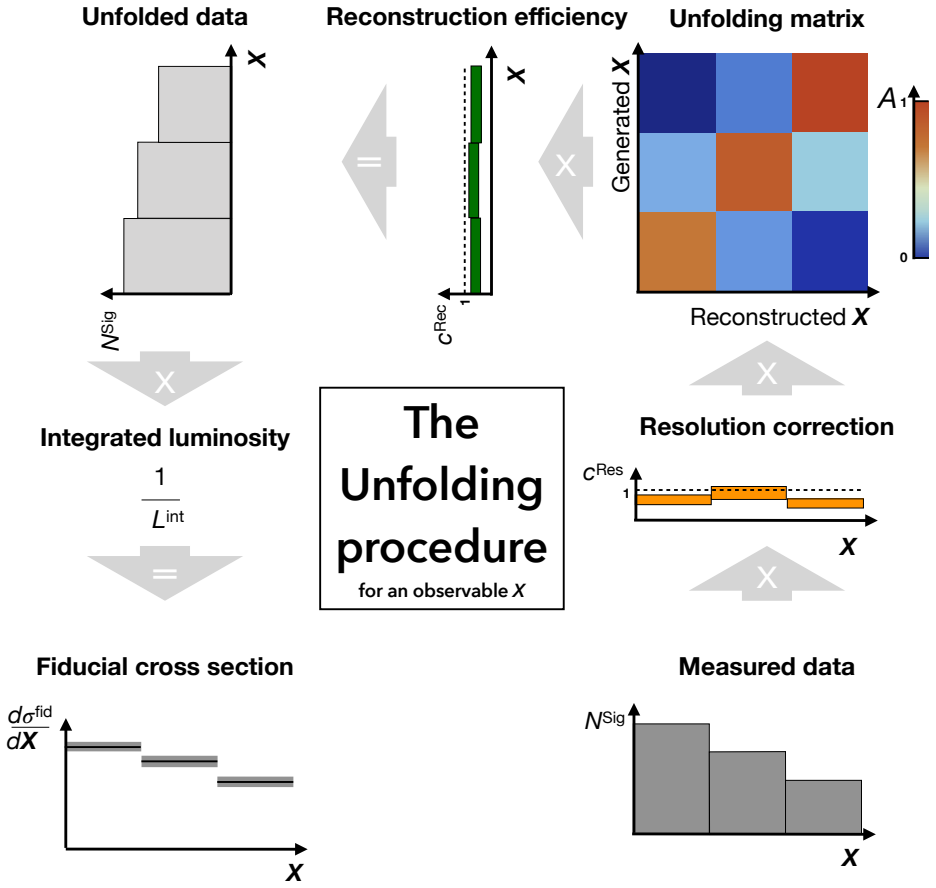

Figure 6.3: The multiple steps and inputs of data unfolding for an arbitrary variable X (begin at bottom right): Raw data is multiplied bin-wise by a resolution correction factor. The unfolding matrix then corrects for detector response effects, "shifting" bin contents. The corrected output finally is multiplied with reconstruction efficiencies, in order to retrieve the number of events at particle level or the fiducial cross section.

the numerator for each reconstructed event the truth event needs to pass the FR requirements listed in Tab. 6.1. The resolution correction reads as

$$c^{\text{Res}} = \frac{N_{\text{SR+FR}}}{N_{\text{SR}}} \quad , \tag{6.7}$$

where N_{SR} is the number of events in the SR, and $N_{\text{SR+FR}}$ is the number of events passing both, the SR and the FR requirements.

Fig. 6.4 shows the distributions of the resulting resolution corrections for the six to be unfolded distributions.

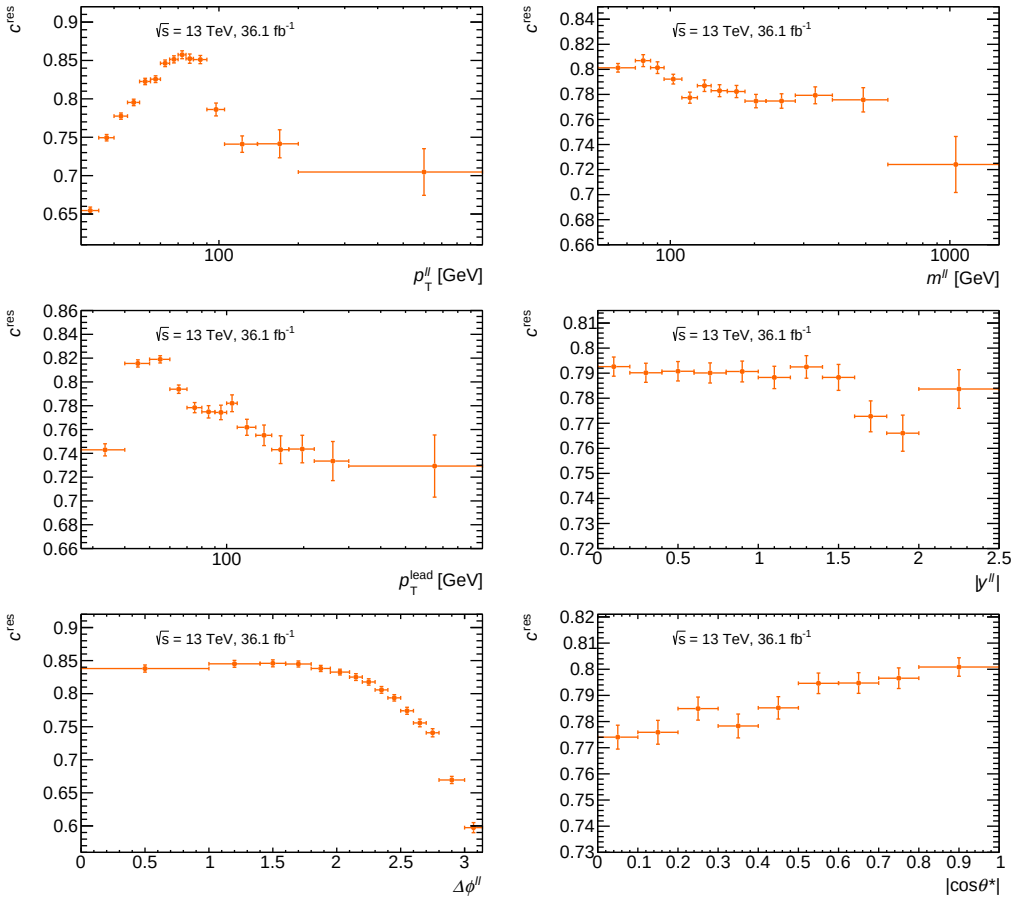

Figure 6.4: The resolution corrections c^{Res}, as explained in the text. Shown are from top left to bottom right the differential distributions in bins of $p_{\text{T}}^{e\mu}$, m_{ee}, $p_{\text{T}}^{\ell_0}$, $|y_{e\mu}|$, $\Delta\phi_{e\mu}$and $|\cos\theta^*|$.

Response matrices Response matrices correct for migrations caused by finite resolution effects in the reconstruction of the energy or angular direction of the particles. Their calculation makes use of Eq. (6.6): They are generated by filling 2-dimensional histograms with the reconstructed observables versus their corresponding truth level observable. All events used to calculate these observables need to be within the SR and the FR, where the SR cuts are applied to reconstructed events and the FR cuts to truth level events. The histograms are normalised "per truth bin", that is per row. In Fig. 6.5 the matrices for the used differential distributions are shown. They are expected to be diagonal, otherwise the procedure would be too model-dependent. The energy related observables (p_T, $m_{\ell\ell}$) show some off-diagonal entries, however, this is still within the accepted range of migrations.

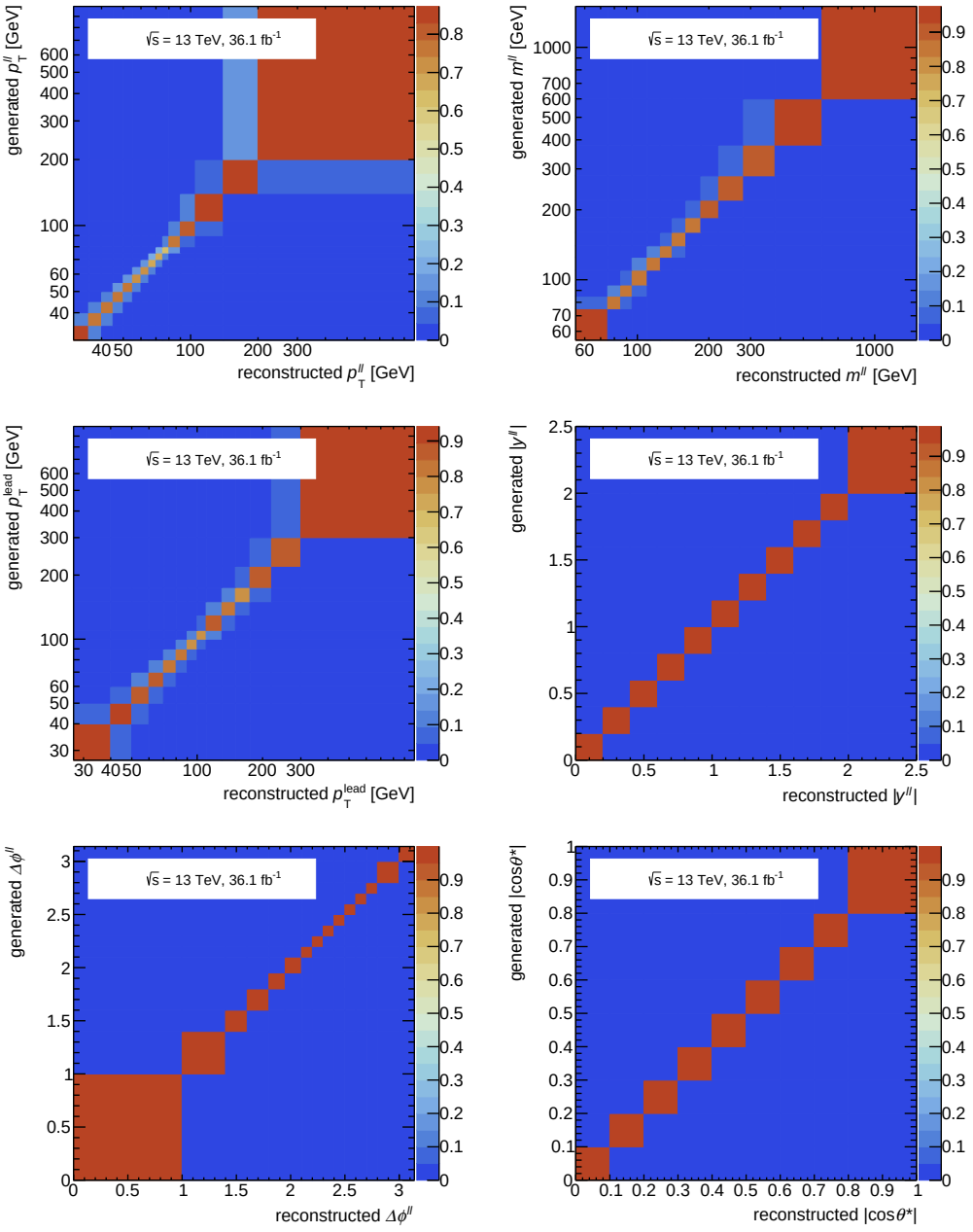

Figure 6.5: The response matrices as defined in the text for (from top left to bottom right) the differential distributions in bins of $p_{\mathrm{T}}^{e\mu}$, m_{ee}, $p_{\mathrm{T}}^{\ell_0}$, $|y_{e\mu}|$, $\Delta\phi_{e\mu}$and $|\cos\theta^*|$.

Reconstruction efficiencies The reconstruction efficiency denominator is defined by the number of generated events passing the FR selection. The numerator definition adds the SR requirements for the events to pass, such that

$$c^{\mathrm{Rec}} = \frac{N_{\mathrm{FR+SR}}}{N_{\mathrm{FR}}} \quad . \tag{6.8}$$

In this equation, N_{FR} is the number of events in the FR, and $N_{\mathrm{FR+SR}}$ is the number of events passing both, the FR and the SR requirements.

Fig. 6.6 shows the resulting reconstruction efficiencies, in bins of the unfolded differential distributions.

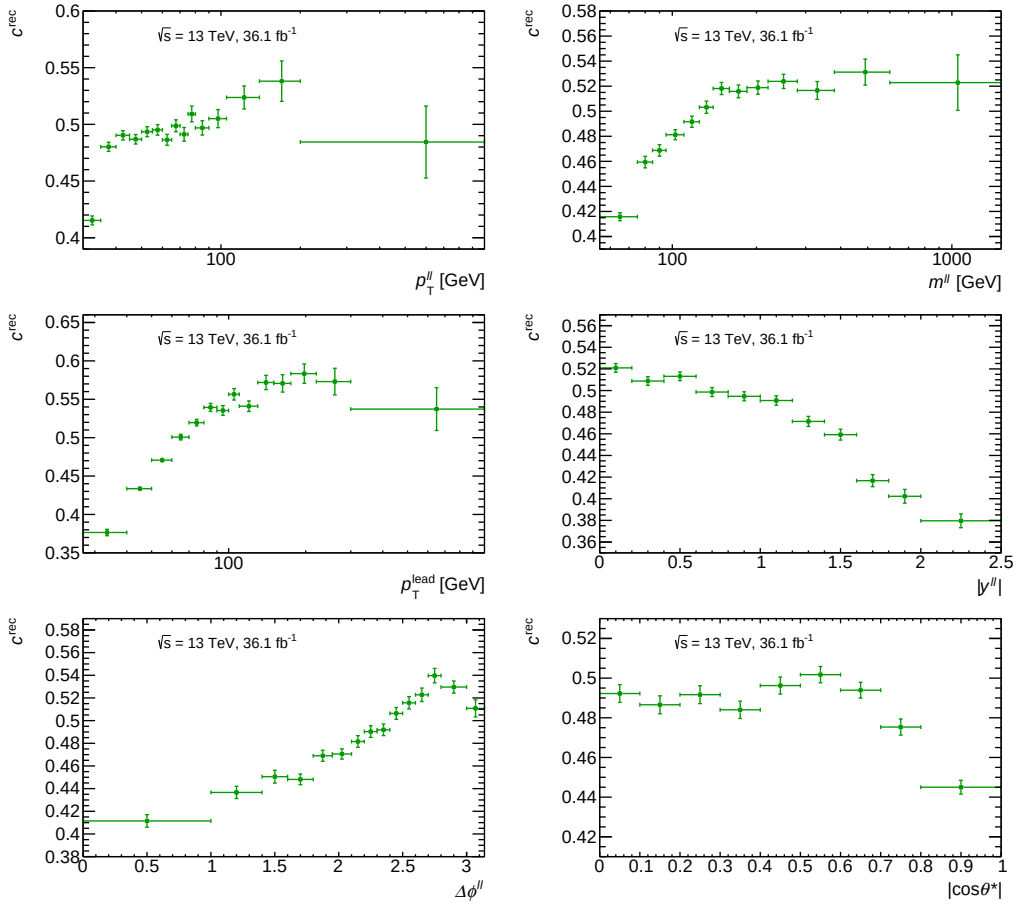

Figure 6.6: Reconstruction efficiencies c^{Rec} as described in the text. Shown are from top left to bottom right the differential distributions in bins of $p_{\mathrm{T}}^{e\mu}$, m_{ee}, $p_{\mathrm{T}}^{\ell_0}$, $|y_{e\mu}|$, $\Delta\phi_{e\mu}$and $|\cos\theta^{*}|$.

Prior The prior $P(N_{\mathrm{true}})$ for each observable is gained from the corresponding response matrix as a projection versus the truth level bins. Therefore it simply describes the theory prediction gained from MC without the use of any data.

6.5.3 Studies on possible bias arising from unfolding procedure

The unfolded distributions are being used in order to set limits on BSM physics using the EFT parametrisation with dimension-six operators, introduced in Chapter 2, Section 2.3. However, it needs to be ensured, that no bias on the results is introduced by the unfolding procedure itself, since the inputs presented in the previous Section 6.5.2 are generated using the SM assumption. If these inputs are different for the BSM case, and this difference is not accounted for, this could lead even to an amplification of BSM effects.

In the following, possible biases are studied by comparing unfolding inputs produced with the SM assumption and the same inputs produced with MC simulation generated using various BSM assumptions. If the inputs are identical for all cases, no bias is expected and possible BSM effects in data are expected to unfold properly, even if the unfolding inputs are produced using the SM assumption.

This comparison is made using two samples generated with the MC@NLO 4.10 event generator [137]. The used generator has the advantage, that it allows to re-weight an already produced sample to any arbitrary aTGC point, which is a point in the

$$\Delta g_1^Z, \Delta k^Z, \lambda^Z, \Delta g_1^\gamma, \Delta k^\gamma, \lambda^\gamma \tag{6.9}$$

parameter space. These parameters were previously defined in Section 2.3, they describe the deviation from SM couplings.

One sample is produced with SM parametrisation, the other with a BSM configuration, i.e. the aTGC parameter Δg^Z being set to 0.6, while all others are kept at 0. The re-weighting is realised by the generator by internally calculating the amplitudes contributing to the W^+W^- process:

$$\mathcal{A} = \mathcal{A}_0 + \Delta g_1^Z \mathcal{A}_{\Delta g_1^Z} + \Delta k^Z \mathcal{A}_{\Delta k^Z} + \lambda^Z \mathcal{A}_{\lambda^Z} + \Delta g_1^\gamma \mathcal{A}_{\Delta g_1^\gamma} + \Delta k^\gamma \mathcal{A}_{\Delta k^\gamma} + \lambda^\gamma \mathcal{A}_{\lambda^\gamma} \ , \tag{6.10}$$

where $\mathcal{A}_0$ is the SM amplitude and the other terms are the amplitudes of the aTGC contributions. Based on this, a total event weight can be calculated, which contains terms deriving from the squared amplitude terms and which stem from the interference terms:

$$\begin{aligned}
w_{\text{tot}} = w_0 &+ (\Delta g_1^Z)^2 & w_1 &+ (\Delta k^Z)^2 & w_2 &+ (\lambda^Z)^2 & w_3 \\
&+ (\Delta g_1^\gamma)^2 & w_4 &+ (\Delta k^\gamma)^2 & w_5 &+ (\lambda^\gamma)^2 & w_6 \\
&+ 2\Delta g_1^Z & w_7 &+ 2\Delta k^Z & w_8 &+ 2\lambda^Z & w_9 \\
&+ 2\Delta g_1^\gamma & w_{10} &+ 2\Delta k^\gamma & w_{11} &+ 2\lambda^\gamma & w_{12} \\
&+ 2\Delta g_1^Z \Delta k^Z & w_{13} &+ 2\Delta g_1^Z \lambda^Z & w_{14} &+ 2\Delta g_1^Z \Delta g_1^\gamma & w_{15}
\end{aligned}$$

$$
\begin{aligned}
&+2\Delta g_1^Z \Delta k^\gamma \quad w_{16} \quad +2\Delta g_1^Z \lambda^\gamma \quad w_{17} \quad +2\Delta k^Z \lambda^Z \quad w_{18} \\
&+2\Delta k^Z \Delta g_1^\gamma \quad w_{19} \quad +2\Delta k^Z \Delta k^\gamma \quad w_{20} \quad +2\Delta k^Z \lambda^\gamma \quad w_{21} \\
&+2\lambda^Z \Delta g_1^\gamma \quad w_{22} \quad +2\lambda^Z \Delta k^\gamma \quad w_{23} \quad +2\lambda^Z \lambda^\gamma \quad w_{24} \\
&+2\Delta g_1^\gamma \Delta k^\gamma \quad w_{25} \quad +2\Delta g_1^\gamma \lambda^\gamma \quad w_{26} \quad +2\Delta k^\gamma \lambda^\gamma \quad w_{27}
\end{aligned} \tag{6.11}
$$

These weights are stored in a vector of the form

$$
\texttt{weight\_vector} = (\texttt{mc\_weight}\ ,\ a_0\ ,\ a_1\ ,\ \ldots\ ,\ a_{27})\ , \tag{6.12}
$$

where $a_i = w_i / w_{\text{tot}}$. Therefore one can easily re-weight a sample by weighting it with

$$
\texttt{weight}\left(\Delta g_{1\,\text{new}}^Z\ ,\ \ldots\ ,\ \lambda^\gamma{}_{\text{new}}\right) = a_0 + a_1(\Delta g_{1\,\text{new}}^Z)^2 + \ldots + 2\Delta k^\gamma{}_{\text{new}} \lambda^\gamma{}_{\text{new}} a_{27}\ . \tag{6.13}
$$

The comparison of unfolding inputs is done for one of the aTGC parameters in Eq. (6.9) at a time, keeping all the others at 0. The used values are within the limits from Ref. [138]:

$$
\Delta g_1^Z = 0.2\ ,\ \Delta k^Z = 0.03\ ,\ \lambda^Z = 0.02\ ,\ \Delta k^\gamma = 0.08 \text{ and } \lambda^\gamma = 0.04\ .
$$

In order to be able to reduce statistical fluctuations when comparing the two sets (i.e. SM and BSM) of unfolding inputs, the same sample is reweighting to the SM and to an aTGC point and then compared, ensuring that the same events are used. This is done twice, one time for each sample.

The unfolding inputs are compared for the observables $m_{\ell\ell}$, $\Delta\phi^{\ell\ell}$ and $p_T^{\ell_0}$. Fig. 6.7 shows the ratios of reconstruction efficiencies (bottom left), resolution corrections (top left) and the response matrix for $p_T^{\ell_0}$, comparing SM and $\Delta g_1^Z = 0.2$. The ratio of the unfolding matrix is shown twice, the bottom left plot of Fig. 6.7 shows the ratio calculated using the BSM sample, the bottom right one makes use the SM sample. The ratios shown in Fig. 6.7 are reasonably flat, fluctuations in the matrices appearing in off-diagonal entries are due to statistical limitations and are expected to have little to no effect since the total values are very small. The same is true for the ratios shown in the Figs. 6.8 and 6.9, which show the corresponding comparison for the observables $m_{\ell\ell}$ and $\Delta\phi^{\ell\ell}$, respectively.

This test was performed for all measured observables and also comparing the SM inputs to those for $\Delta k^Z = 0.03$, $\lambda^Z = 0.02$, $\Delta k^\gamma = 0.08$ and $\lambda^\gamma = 0.04$, respectively. None of the unfolding inputs showed any significant deviation from the SM case for any of the listed BSM cases. Thus, no bias is expected to be introduced by unfolding BSM physics using SM assumptions.

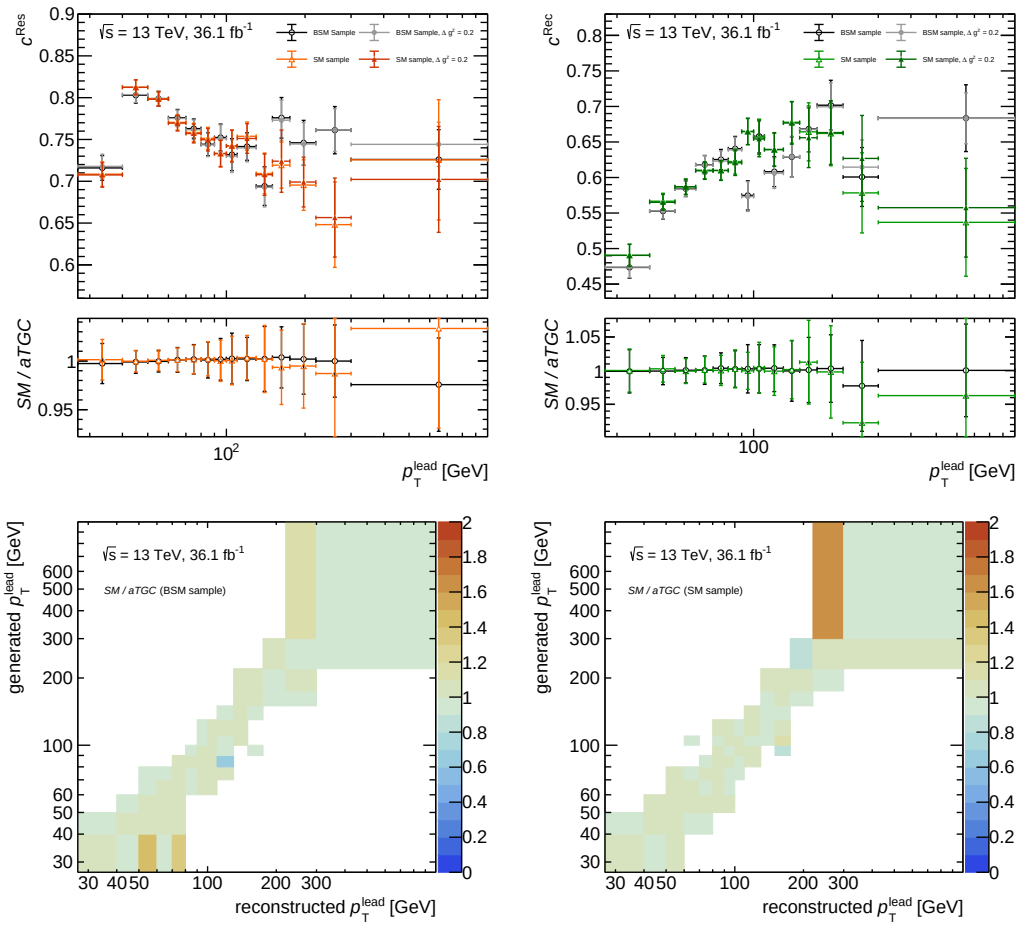

Figure 6.7: Ratios of unfolding inputs for $p_T^{\ell_0}$ and comparing SM to BSM (aTGC parameter $\Delta g_1^Z = 0.2$). The top left plot shows the comparison for the resolution correction, top right shows the comparison for the reconstruction efficiency If no aTGC paramter is given in the legend, the sample is re-weighted to SM. The distributions using round markers are made using the BSM sample, triangle markers are referring to the SM Sample. Bottom left shows the ratio of the response matrices, using the BSM sample. Bottom right, shows the response matrix ratio made with the SM sample.

Since the unfolding inputs are calculated from the very same sample which has just been reweighted to SM and to BSM, the statistical uncertainties might not be very accurate. Therefore, a similar test as the one shown above has been carried out comparing the inputs calculated for odd and even events only, which allows to estimate the statistical uncertainty as the difference between results. It was found that the differences between SM and BSM infolding inputs were well within that uncertainty.

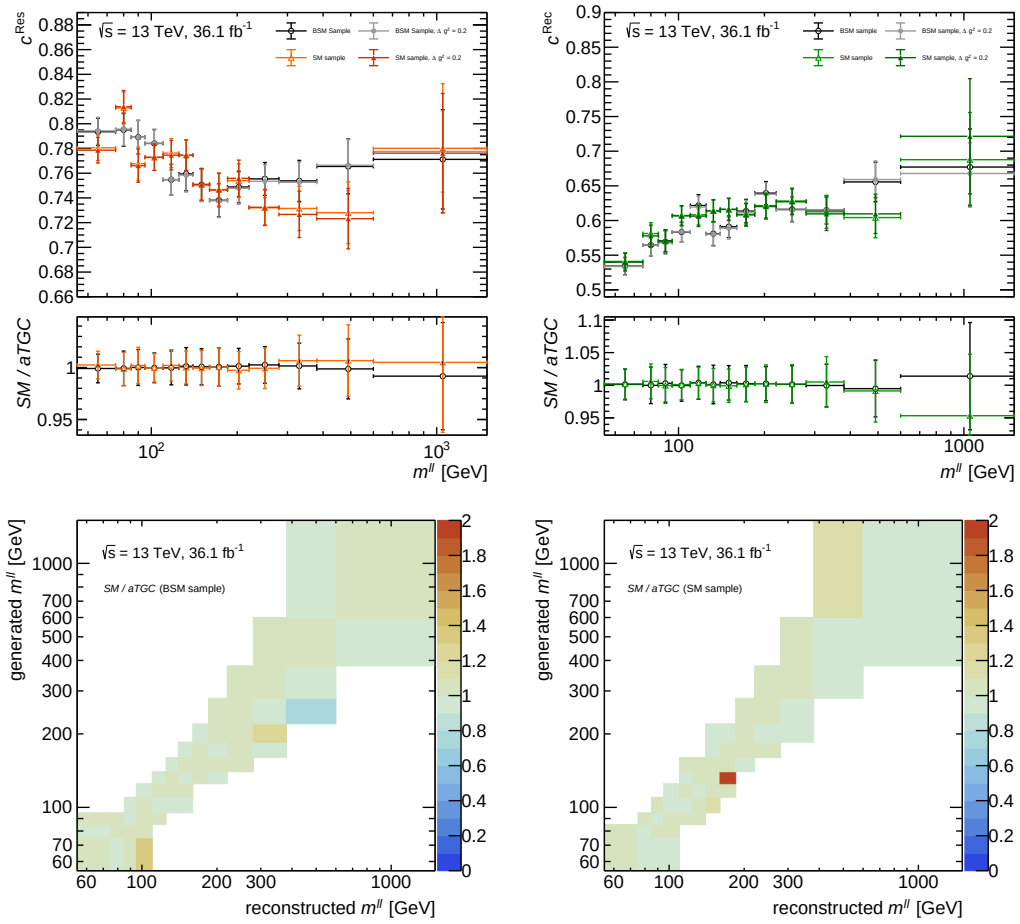

Figure 6.8: Ratios of unfolding inputs for $m_{\ell\ell}$ and comparing SM to BSM (aTGC parameter $\Delta g_1^Z = 0.2$). The top left plot shows the comparison for the resolution correction, top right shows the comparison for the reconstruction efficiency If no aTGC parameter is given in the legend, the sample is re-weighted to SM. The distributions using round markers are made using the BSM sample, triangle markers are referring to the SM Sample. Bottom left shows the ratio of the response matrices, using the BSM sample. Bottom right, shows the response matrix ratio made with the SM sample.

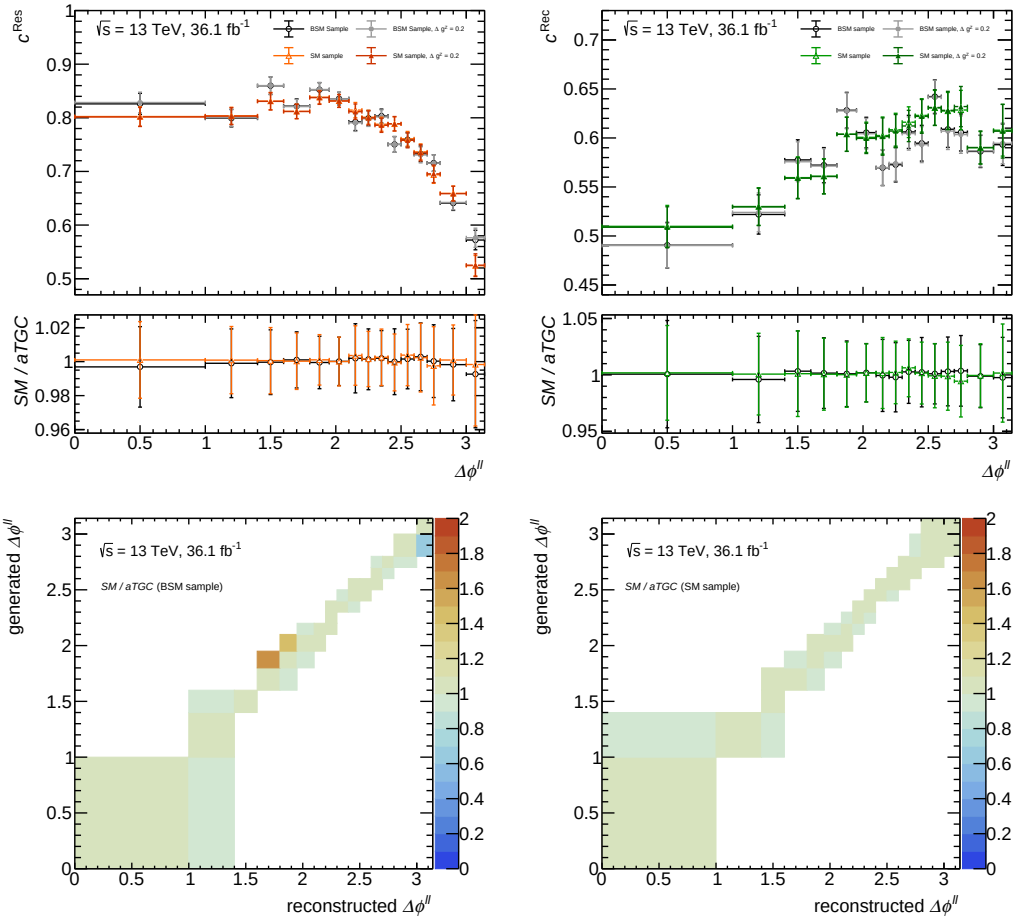

Figure 6.9: Ratios of unfolding inputs for $\Delta\phi_{e\mu}$ and comparing SM to BSM (aTGC parameter $\Delta g_1^Z = 0.2$). The top left plots shows the comparison for the resolution correction, bottom left shows the comparison for the reconstruction efficiency If no aTGC parameter is given in the legend, the sample is re-weighted to SM. The distributions using round markers are made using the BSM sample, triangle markers are referring to the SM Sample. Bottom left shows the ratio of the response matrices, using the BSM sample. Bottom right, shows the response matrix ratio made with the SM sample.

6.6 Results

Fig. 6.10 shows the resulting differential cross sections, as they are already published in Ref. [3]. The result is compared to three different NNLO theory predictions. Theory and measurement in general agree very well within the uncertainties.

In addition, the fiducial cross section is measured, the result is show on the left plot in Fig. 6.11. The right plot in Fig. 6.11 shows the fiducial cross section as a function of the cut on the jet transverse momentum. This is kind of measurement is performed as seven independent measurements of the fiducial cross section, each using a different jet p_T veto cut: Along the nominal $p_T^{\text{jet}-\text{veto}} = 35\,\text{GeV}$ fiducial cross section measurement, also the values 30, 40, 45, 50, 55 and 50 GeV are applied. In both plots of Fig. 6.11 the measurement is compared to three different theory predictions. The left plot also shows statistical and systematic uncertainties on the fiducial cross section result. The total uncertainty is dominated by the systematic uncertainty.

Limits on aTGC are set using an EFT fit on the unfolded leading lepton p_T (p_T^{lead}) fiducial cross section, which was identified as the unfolded distribution most sensitive to the effect of the five EFT operators presented in Section 2.3 [3], also referred to as Wilson coefficient in literature. The resulting limits are presented in Tab. 6.7.

Table 6.7: Constraints on the Wilson coefficient in an EFT model [35], i.e. the EFT parameters discussed in Section 2.3, that includes operators affecting gauge boson interactions. Taken from Ref. [3].

Operator	Observed, 95% CL [TeV^{-2}]	Expected, 95% CL [TeV^{-2}]
c_{WWW}/Λ^2	[-3.3 , 3.2]	[-3.0 , 3.0]
c_W/Λ^2	[-7.3 , 3.9]	[-6.4 , 5.1]
c_B/Λ^2	[-20 , 17]	[-18 , 17]
$c_{\tilde{W}WW}/\Lambda^2$	[-1.6 , 1.6]	[-1.5 , 1.5]
$c_{\tilde{W}}/\Lambda^2$	[-76 , 76]	[-91 , 91]

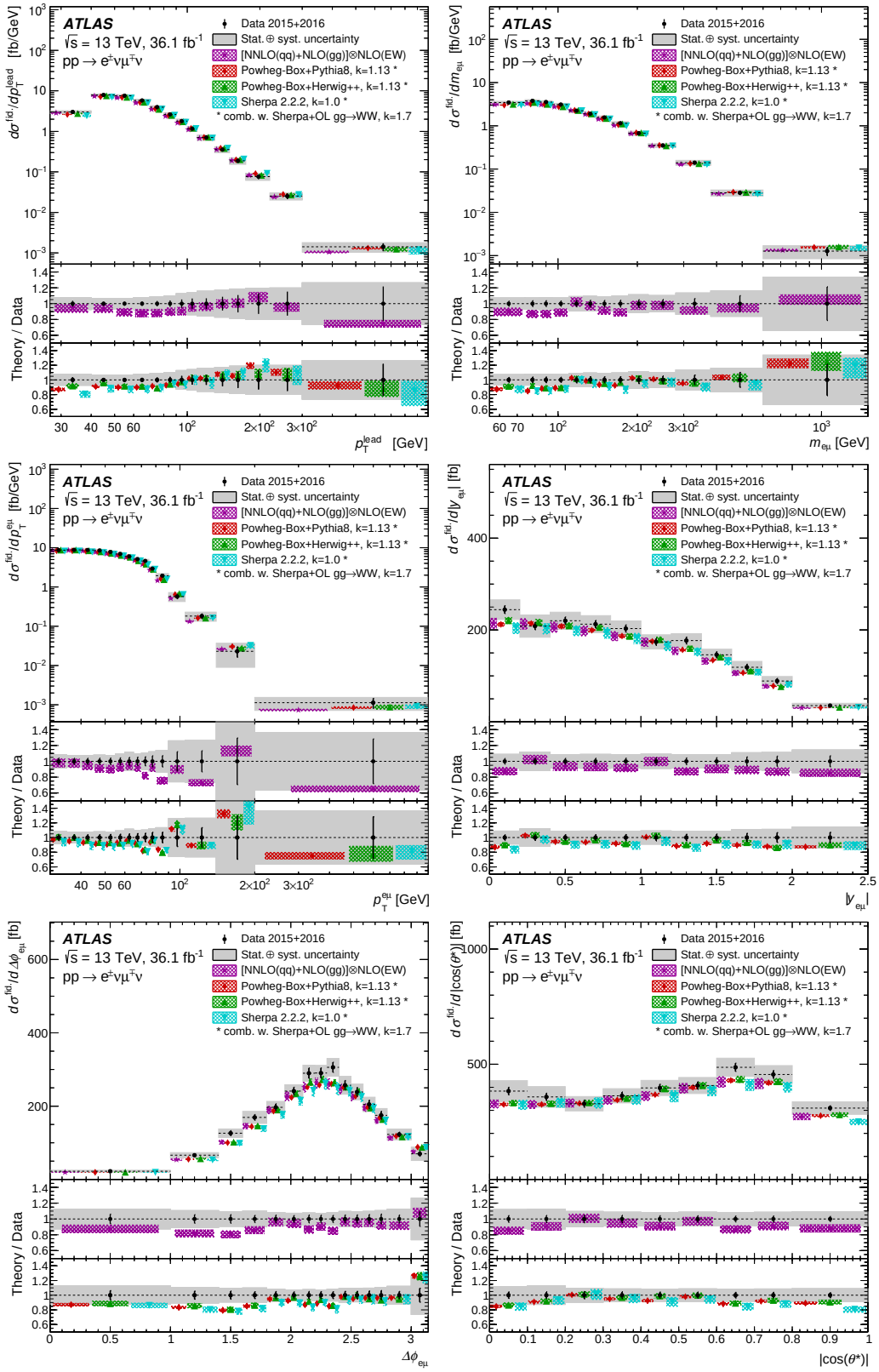

Figure 6.10: Measured differential cross sections of $pp \to W^+W^-$ compared to three different theory predictions, taken from Ref. [3]. The black dots show the measured cross sections, while the grey bars indicate the total uncertainty of this measurement.

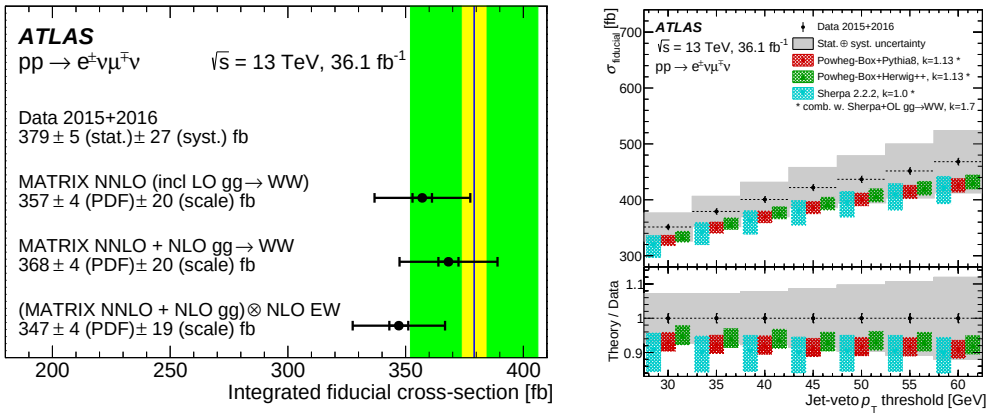

Figure 6.11: Measured fiducial cross section (left) and vs. the jet veto p_T threshold (right) of $pp \rightarrow W^+W^-$, compared to three different theory predictions, taken from Ref. [3]. The uncertainty is shown as a coloured band, where the green bands represent the systematic uncertainty and the statistical uncertainty is highlighted in yellow. The total uncertainty is clearly dominated by the systematic uncertainty. The shown result of the measured fiducial cross section uses $p_T^{\mathrm{jet-vetp}} = 35\,\mathrm{GeV}$ and therefore shows the same result as the second bin of the right plot.

Chapter 7

The future of W^+W^- cross section measurements

The previous Chapter 6 outlined the published analysis of the 2015+2016 data sets where the background rejection was purely based on applying simple selection criteria on physical variables, which can more or less be measured directly, but without taking into account combinations or correlations between these variables. In contrast to this "rectangular cut selection", multivariate classification methods or algorithms (MVA) use the multidimensional observable space rather than each variable separately [139].

This chapter presents studies on the use of MVA methods in the W^+W^- analysis using the so-called matrix element method (MEM). The presented studies did not result in a W^+W^- cross section measurement using the presented MVA methods at the date of thesis submission, therefore the chapter title has the word future in it.

7.1 Towards a multivariate analysis

Multivariate techniques usually combine the information gained from the multiple observables into a single variable $y = y(\mathbf{x})$. $\mathbf{x} = (x_1, ..., x_D)$ is the so-called feature vector, containing D observables mapped into the MVA classifier y [139]. The goal is to classify events into signal or background by simply applying a cut on y, that is, using it as a discriminant.

7.1.1 Receiver operating characteristic

Receiver operating characteristic (ROC) graphs are a good tool for estimating the performance of classifiers [140]. The basic idea is to display the relative rate of

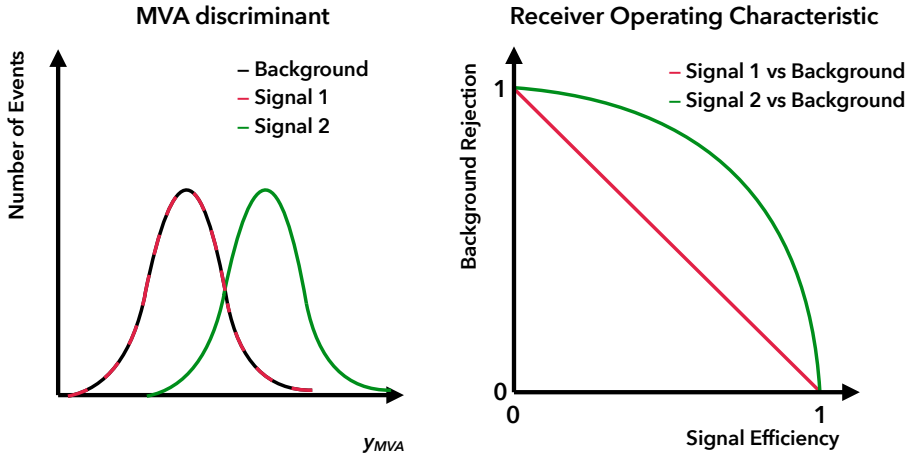

Figure 7.1: Distribution of two different signal events and background events using a classifier y_{MVA} (left) and the resulting ROC curves (right). Signal 1 can not be separated from background using this discriminant, the ROC curve is linear, so this classifier would not give any separation power. Signal 2 has a distinct different y_{MVA} distribution, the corresponding ROC curve has an integral between 0.5 and 1.

true positive (TP), false positive (FP), true negative (TN) and false negative (FN) classified events. A TP event is in this case a signal W^+W^- event which is correctly classified as signal, while a TN event would be a $t\bar{t}$ event classified as background. FP and FN events would be events classified into the wrong category such as a $t\bar{t}$ event classified as signal W^+W^-. The relative rate of TP event can be named signal efficiency, while the corresponding rate of TN events would be the background efficiency.

The left plot in Fig. 7.1 shows the distribution of two different type of signal events and one type of background events using the a classifier y_{MVA}. At every point of y_{MVA} a relative signal and background efficiency can be calculated. By drawing these against each other in a 2-dimensional ROC space (right plot in Fig. 7.1), the ROC graphs appear. An ideal classifier would have 100% signal efficiency while having 0% background efficiency and the other way round. Thus, the area covered by the ROC graph would be equal 1. However in general, MVA discriminant distributions overlap, therefore background rejection becomes worse for higher signal efficiency and vice versa [139]. The ROC integral can be used as a measure of quality of a classifier, the closer to 1 it gets, the better the classifier is performing. The other extreme, i.e. the case of no signal-background separation, is also depicted in fig 7.1: A linear ROC curve with an integral of 0.5.

7.1.2 Multivariate classifiers

Several MVA technics are available to perform this task. For example machine learning algorithms (MLAs) like BDTs or neural networks (NNs) became very popular in the last years [141]. MLAs are trained using signal and background samples before being applied to actual analysis. The classifiers gained for example by minimising a loss function $L(C, y(\mathbf{x}))$ in case of NN [139], where C stands for a hypothesis like signal ($S, C = 1$) or background ($B, C = 0$).

A more simple classifier is a likelihood classifier, or as in Ref. [139], a naive Bayes classifier. This was previously introduced in Eq. (5.2) as an electron identification discriminant:

$$y_L = \frac{L_S}{L_S + L_B} \tag{7.1}$$

The MVA discriminant y_L is based only on signal (S) and background (B) likelihoods $L_{S/B}$. However, instead of using likelihoods gained from detector responses, one can use the theoretical knowledge of the four-vectors in a reconstructed event, in order to calculate the likelihoods [142].

7.1.3 The Neyman-Pearson lemma

In fact, if one has access to the Pdfs for the signal case $p(\mathbf{x}|S)$ and the background case $p(\mathbf{x}|B)$, according to the Neyman-Pearson lemma [143], the optimal classifier can be gained by the ratio of the Pdfs [139]:

$$y = \frac{p(\mathbf{x}|S)}{p(\mathbf{x}|B)}. \tag{7.2}$$

The classifier y_L from Eq. (7.1) is a close-to-optimal classifier then, according to the Neyman-Pearson lemma [139]. Theoretical differential cross sections are basically nothing other than the likelihood of an event to happen at a certain point of the phase space. Using the theory predictions in combination with a parametrised detector response for calculating the likelihoods for constructing a classifier y, the method is then called the matrix element method*, since it makes use of the matrix element of the processes.

The MEM was originally introduced in 1988 as a method for analysing $t\bar{t}$ production and decays at Tevatron experiments [146, 147]. Back then, not the exact likelihood was calculated, but weights based on the likelihood, which are gained using simplifying assumptions due to measurement and computing power limitations. First uses at LHC experiments included the search for top quark-Higgs

*Previously this method was also referred to as dynamical likelihood method [144]. Another proposed name is method of total event likelihoods (TELL), as extensively discussed in Ref. [145].

couplings [148, 149] as well as Higgs boson measurements itself [6], among other uses [150]*.

Since MLAs usually are trained using MC predictions which are based on the cross section, these algorithms basically use the same input. However, they are limited by the statistics of the MC sample and by the choice of input variables. Thus, the MEM should be in principle superior to MLAs, since it makes use of the same matrix elements but is not statistically limited and uses by default the full kinematic information.

Recent developments make it possible to calculate the MEM likelihood in an automated way. This is provided by the MoMEMta package [151, 152], explained in the next section.

7.2 Calculating the likelihood

The challenge of the MEM introduced in the previous section is the calculation of the event likelihoods of reconstructed events. This section is following mainly the description from the MoMEMta reference paper [152], which on the other hand refers to Ref. [153] as a good description of the method. The likelihood for retrieving a partonic final state $\mathbf{x}^{\text{part}}$ † is proportional to the differential cross section $\mathrm{d}\sigma_\alpha$ [152]:

$$\mathrm{d}\sigma_\alpha(x_1, x_2, \mathbf{x}^{\text{part}}) = \frac{(2\pi)^4 |\mathcal{M}_\alpha(x_1, x_2, \mathbf{x}^{\text{part}})|^2}{x_1, x_2, s} \mathrm{d}\phi(\mathbf{x}^{\text{part}}) \tag{7.3}$$

The initial state proton momentum fractions are denoted as x_1 and x_2, while the hadronic centre-of-mass energy is denoted as s. The index α denotes any kind of process contained in the squared matrix element $|\mathcal{M}_\alpha(q_1, q_2, \mathbf{x}^{\text{part}})|^2$. The n-body phase space of the final state is denoted as $\mathrm{d}\phi(\mathbf{x}^{\text{part}})$. It is important to consider it in the calculation, since it plays an important role in possible change of variables in an integration of the differential cross section [152].

The initial state parton momenta are described by the PDFs $f_{a_1}(x_1)$ and $f_{a_2}(x_2)$ for a given flavour a_i. PDFs were already introduced in Chapter 2. The hadronic cross section is obtained by convoluting the cross section from Eq. (7.3) with these PDFs and summing over all possible flavour compositions of the colliding partons

*Ref. [150] provides a list of MEM uses at LHC Run-1.

†In Section 7.1, $\mathbf{x}$ denotes the feature vector, containing all possible variables. From now on this is specified to be the collection of final state momenta.

[152]:

$$\mathrm{d}\sigma_\alpha(\mathbf{x}^{\mathrm{part}}) = \int_{x_1,x_2} \sum_{a_1,a_2} \mathrm{d}x_1 \mathrm{d}x_2 f_{a_1}(x_1) f_{a_2}(x_2) \mathrm{d}\sigma_\alpha(x_1, x_2, \mathbf{x}^{\mathrm{part}}) \tag{7.4}$$

Remark Until now, a naive Bayes classifier calculated with likelihoods based on normalised cross sections calculated using Eq. (7.4) would be almost an ideal classifier. However, usually one is already limited to the usage of leading-order matrix elements: Using higher orders leads to an intrinsic theoretical difficulty to identify final state particles with partons [152].

7.2.1 Detector effects

In addition, using the full information $\mathbf{x}^{\mathrm{part}}$ is in general not possible, since the momenta from some particles cannot be reconstructed, because they lie outside the detector acceptance. For neutrinos this is always the case. Other effects stem from parton showers, hadronisation or simply insufficient detector resolution [152]. These effects make it necessary to parameterise the detector effects, such that the measured $\mathbf{x}^{\mathrm{vis}}$ final state can be transferred to the particle level configuration $\mathbf{x}^{\mathrm{part}}$. This happens by the usage of a so-called transfer-function (TF) $T(\mathbf{x}^{\mathrm{vis}}|\mathbf{x}^{\mathrm{part}})$. The TFs are normalised in order to act like a probability density. They contain reconstruction efficiency terms as well as resolution terms and are obtained for each type of particle separately*. They will be discussed in more detail in the next section.

The final likelihoods L_α going into the discriminant in Eq. (7.1) are then obtained by convoluting the TFs and the hadronic cross section from Eq. (7.4) [152]:

$$\begin{aligned} p(\mathbf{x}^{\mathrm{vis}}|\alpha) = &\frac{1}{\sigma_\alpha^{\mathrm{vis}}} \int_{x_1,x_2} \sum_{a_1,a_2} \int_{\mathbf{x}^{\mathrm{part}}} \mathrm{d}\phi(\mathbf{x}^{\mathrm{part}}) \mathrm{d}x_1 \mathrm{d}x_2 \\ &\times f_{a_1}(x_1) f_{a_2}(x_2) \mathrm{d}|\mathcal{M}_\alpha(x_1, x_2, \mathbf{x}^{\mathrm{part}})|^2 T(\mathbf{x}^{\mathrm{part}}|\mathbf{x}^{\mathrm{vis}}) \end{aligned} \tag{7.5}$$

The normalisation factor $\sigma_\alpha^{\mathrm{vis}}$ makes sure that $p(\mathbf{x}^{\mathrm{vis}}|\alpha)$ is a Pdf. Without proper normalisation, the result of Eq. (7.5) is also referred to as matrix element weight [152].

Remark 1 Note that in Eq. (7.5) the reconstruction efficiency term is absorbed into the TF $T(\mathbf{x}^{\mathrm{part}}|\mathbf{x}^{\mathrm{vis}})$. In the MoMEMta reference paper [152] it is written

*In a sense, TFs are similar to the unfolding inputs described in the previous chapter, however apply not to the whole event but only to a single particle. They are also used in the "opposite direction": Unfolding aims to remove the detector effects on a measured distribution, while TFs add the detector effects on a theoretical prediction.

explicitly as

$$p(\mathbf{x}^{\text{vis}}|\alpha) = \frac{1}{\sigma_{\alpha}^{\text{vis}}} \int_{x_1,x_2} \sum_{a_1,a_2} \int_{\mathbf{x}^{\text{part}}} \mathrm{d}\phi(\mathbf{x}^{\text{part}}) \mathrm{d}x_1 \mathrm{d}x_2 ... T(\mathbf{x}^{\text{part}}|\mathbf{x}^{\text{vis}}) \epsilon(\mathbf{x}^{\text{vis}}) \tag{7.6}$$

The reason for this is, that the final software implementation written for this theses treats efficiencies as TFs.

Remark 2 Note that the term likelihood is used, even though Eq. (7.5) uses the nomenclature of a Pdf. This is because usually products of several Pdfs are used for calculating the likelihood:

$$L_{S/B} = \prod_{i=1}^{D} p_i \alpha_{S/B} |\mathbf{x}^{\text{vis}} \tag{7.7}$$

The product of Pdfs is only a Pdf itself, if the individual probabilities are uncorrelated [139].

7.2.2 The MoMEMta toolkit

The calculation of likelihoods is done making use of MoMEMta [152]. This tool provides a framework for arbitrary weight or likelihood calculations. It uses the four-momenta as inputs and allows to easily construct configurations for various physics processes. This is done by separating the calculation into blocks [151] which can be plugged together such that any possible scattering processes can be constructed.

The user only has to choose the matrix element, the PDFs and it is also possible to define custom TFs.

Matrix elements are imported from MadGraph [154]. As default the CT10nlo PDF from LHAPDF [155] is used. Eq. (7.5) usually results in high-dimensional integrals. The necessary MC integration happens using the Vegas algorithm [156] from the cuba program library [157]. This is also already implemented in the MoMEMta toolkit.

The only tasks really leftover to the user setting up a MEM analysis is the implementation of solid and analysis-related TFs. Doing this, the user has to make sure, the custom module having these TFs implemented return the product of the value of the TF and a Jacobian ($T \times J$). The latter is important, because extra dimensions integrated using MC are by default restricted to values between 0 and 1. This interval has to be expanded to the actual phase space going into the calculation.

The configuration of blocks for the ME calculation is in principle also left over to the user, however the software package comes with some tutorials and examples which already cover most of the standard use cases, such that the work presented later in this chapter could be build upon these *.

The remaining sections will focus on the implementation of MEM into a possible full ATLAS Run-2 W^+W^- cross section measurement.

7.3 Transfer-functions

When absorbing the efficiency terms into the TF T, it reads as [145, 158] †

$$\begin{aligned} T(\mathbf{x}^{\text{part}}|\mathbf{x}^{\text{vis}}) = &\frac{1}{N_{\text{perm}}} \sum_{i \in \text{perm}} w_i \\ &\times \prod_{j \in \text{matched}} \epsilon(p_{ij}) W_{\text{res}}(p_{ij}^{\text{vis}}, p_{ij}) \prod_{k \in \text{unmatched}} (1 - \epsilon(p_{ik})) \quad . \end{aligned} \tag{7.8}$$

All possible permutations (perm) of final state particles have to be considered. Thus, their efficiency terms ϵ and the resolution functions W_{res} are summed up and divided by the number of permutations N_{perm}. Each permutation consists of the product of an efficiency term of the matched final state particles, the resolution function and a product of efficiency terms for the unmatched particles. The efficiencies and resolution functions are denoted as functions of the final state particle momenta p_i. The resolution function depends on the measured final state momenta p^{vis} and the actual momenta. Thus the efficiency terms act like reconstruction efficiencies, while the resolution functions consider the detector resolution. The latter are normalised to one, since they give the conditional probability to measure a recorded momentum p^{vis} given a momentum p [145, 158]:

$$\int \mathrm{d}^3 p^{\text{vis}} W_{\text{res}}(p^{\text{vis}}|p) = 1 \tag{7.9}$$

Both, efficiency terms and resolution functions are obtained from simulated data, since the real momenta p cannot be measured. They depend on the kind of final state particle, their energy and also the direction inside the detector.

*These can be easily be found via the MoMEMta website: `momemta.github.io`

†The doctoral theses by Sören Stamm and Patrick Rieck explain the usage of MEM in an ATLAS single top s-channel measurement, published in Ref. [159].

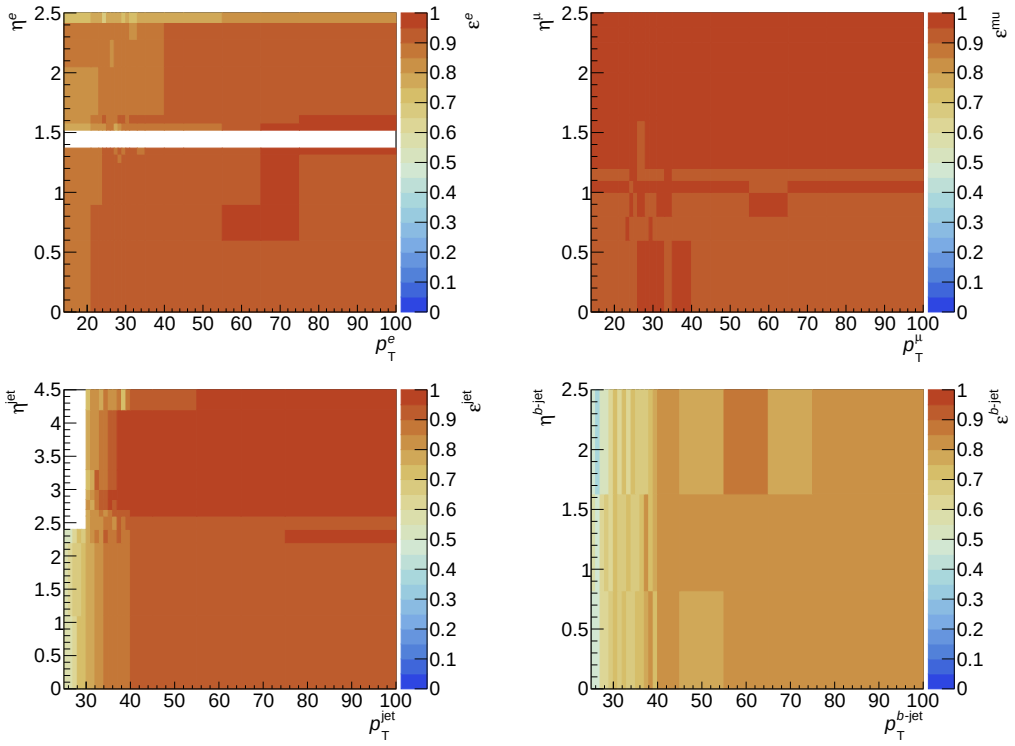

Figure 7.2: Reconstruction matching for electrons, muons, jets and b-jets (from top left to bottom right) as functions of η and p_T.

7.3.1 Reconstruction matching efficiencies

Reconstruction efficiencies are calculated by comparing generator level simulations (truth-level) and detector level simulations (reconstruction-level). Truth-level objects having a reconstruction-level counterpart within a cone with $\Delta R = 0.04$ are regarded as successfully reconstructed. The efficiency then is calculated by

$$\epsilon = \frac{N^{\text{reco},\Delta R=0.4}}{N^{\text{truth}}} \tag{7.10}$$

The efficiencies are calculated in bins of η and p_T for electron, muons, light jets and b-jets, the results are presented in Fig. 7.2. Lepton reconstruction efficiencies are in general very high ($> 90\%$). This is also true for jet efficiencies, with the caveat that especially at transverse momenta lower than 30 GeV they drop significantly to values around 50%. Note that jets can not be reconstructed for $p_T < 30\,\text{GeV}$ and $\eta > 2.4$ due to the detector acceptance. Jets stemming from b-quarks rely on tracking information, which is why they can not be reconstructed in the forward region $\eta > 2.5$. In addition due to limitations in b tagging, the efficiencies usually do not go beyond 85%, while for $p_T < 30\,\text{GeV}$ the combination of low jet reconstruction

in general in combination with the b tagging efficiency leads to efficiencies even below 50%.

Custom modules written for the MoMEMta toolkit in order to apply these efficiencies use the particle four-vectors as inputs and return the corresponding efficiency value as the value of $T \times J$.

7.3.2 Resolution functions

Resolution functions are calculated using simulated $t\bar{t}$ samples, again by comparing truth and reconstructed particle information. This is implemented by Hannes Mildner [160] as part as a combined effort on this topic. By taking the relative energy or transverse momentum difference into account, one can fit the result using a simple Gauss function for a certain range of p_T^{vis}.

$$W_{\text{res}}(p_T^{\text{vis}}|p_T) = \begin{cases} n \exp\left\{\left(\frac{-(p_T-\mu)^2}{\sigma}\right)\right\} & , \; p_T < c(\mu) \\ \exp\{(-\alpha p_T)\} & , \; p_T > c(\mu) \end{cases} \tag{7.11}$$

The multiple resolutions have five parameters: The width σ, the mean μ and the normalisation n for the gaussian part and the α parameter for the exponential tail. The cut off parameter c defines where the exponential takes over. For full parametrisation of the resulting resolution can be achieved by fitting these parameters of the gaussian function as a function of eta and p_T. An example of b-jet resolution functions using this approach is shown in Fig. 7.3. Two effects stick to the eye: Towards lower energies, the reconstructed b-jet transverse momentum is lower than at particle level. In addition the width of the resolution gets wider. This is expected, considering the known energy resolution of the calorimeters.

7.3.3 Missing jets

The challenging part of MEM in W^+W^- measurements is, that the W^+W^- matrix element comes with no final state jets, while the main background stemming from top decays have one or two final state b-jets. In a W^+W^- SR, no jets are expected to be reconstructed, however they are necessary in order to calculate the top matrix elements. While the missing transverse energy of the neutrinos E_T^{miss} is taken care of separately by the MoMEMta algorithm, there is no provided option to find solutions for missing jets.

Therefore a dedicated custom TF for these missing jets has to be implemented by the user. It provides an integral over the "invisible jet phase space", the phase space outside detector acceptance. In addition, reconstruction (in-)efficiencies

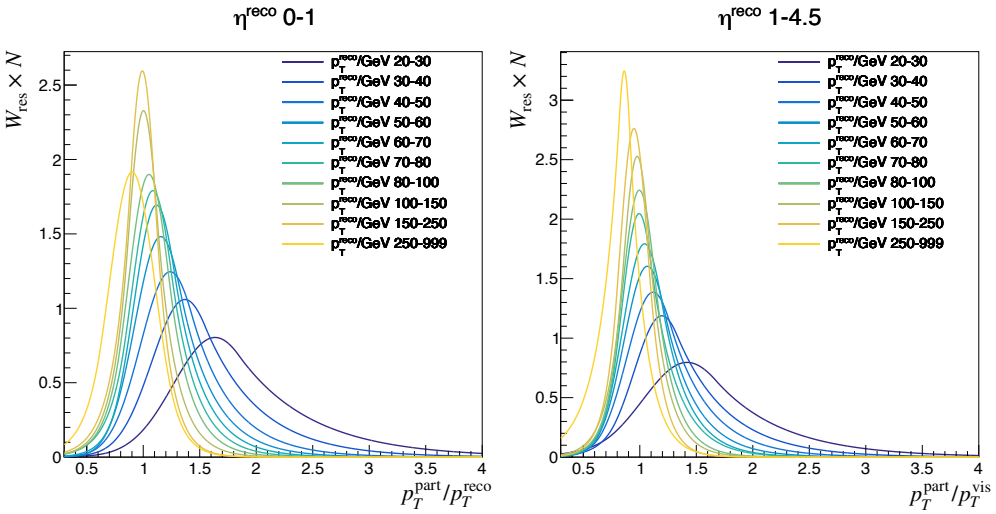

Figure 7.3: The resolution functions for b-jets in two different η bins and for different ranges of p_T, provided by [160]. They are drawn as functions of $p_T^{\text{part}}/p_T^{\text{vis}}$. There is a general trend of a lower reconstructed transverse momentum p_T^{vis}, than one would expect from the particle level p_T^{part}. This effect is stronger towards lower bins of $p_T^{\text{reco}} \equiv p_T^{\text{vis}}$. The y-axis label $W_{\text{res}} \times N$ indicates, that the shown resolution functions are not normalised.

$(1-)\epsilon^{\text{jet}}$ are directly adapted. Thus, one can parametrise the TF as

$$T_{\text{missing jet}} = \begin{cases} 1-\epsilon^{\text{jet}} & , \eta < 4.5 \text{ and } p_T < 30\,\text{GeV} \\ 1 & , \eta > 4.5 \\ 0 & , \text{else} \end{cases} \tag{7.12}$$

The cut-off transverse momentum of 30 GeV for $\eta < 4.5$ is chosen out of practical computing reasons. This TF is basically a flat resolution function on the whole η-p_T space, having the known jet efficiencies directly applied.

The MC integration is chosen to act on a $(\eta, \log E)$ phase space, since the transverse momentum is η dependent. The logarithm in the integration variable is chosen, since the expected event rate performs more uniform on a logarithmic range. This can be seen in Fig. 7.4, showing generator level distributions of η^{jet} and $\log E^{\text{jet}}$. From this, reasonable integration regions are estimated to be $0 < |\eta^{\text{jet}}| < 6$ and $2 < \log E^{\text{jet}}[\log \text{GeV}] < 8$, also defining the Jacobian used for the final weight calculation.

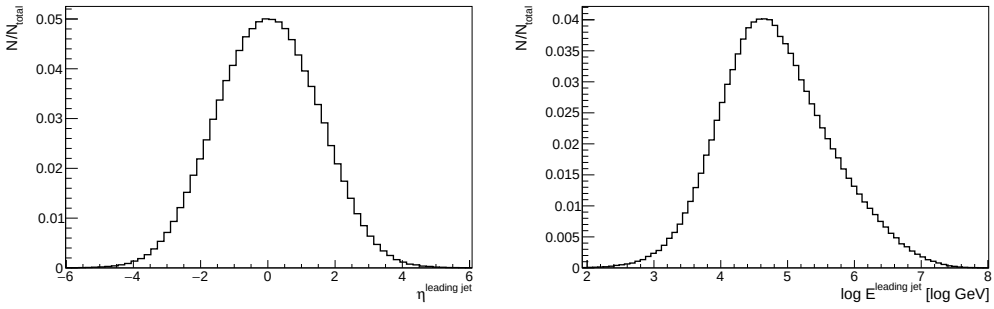

Figure 7.4: Normalised particle level distributions of the leading jets η (left) and $\log E$ (right) using 1 million $t\bar{t}$ events.

7.4 First steps

As a first test, the matrix elements which play a role in the analysis should be tested. Therefore some specifics of the processes are tested. These are sanity checks, reimplementing tests already undertaken in Ref. [152]. The first test is a top mass measurement, making use of a top matrix element. The second one tests the Wt process, by separating the charge configuration.

7.4.1 Top quark mass in $t\bar{t}$ events

In order to test the $t\bar{t}$ matrix element, a top mass measurement is undertaken. Since the top quark mass is a free parameter of the matrix element it can be changed by hand. By calculating the element several times but with different mass choices, the likelihood is expected to be minimal at the true mass. To have full control of the test, it is performed on a simulated sample, where the mass is already known. This kind of measurement was done by the DØ collaboration [161] and already has been implemented in MoMEMta as an example [151]. The basic principle is calculating the process likelihood

$$L = \prod_{i, i \in \text{data}} p(x_i|\alpha_m) \tag{7.13}$$

as the product of the event weights computed for an event x_i, where i stands for an event number. α_m denotes the assumption of the process given a certain top mass m, thus $p(x_i|\alpha_m)$ gives the likelihood of an event stemming from this kind of process. From this, one can easily regard the negative sum of the logarithms of

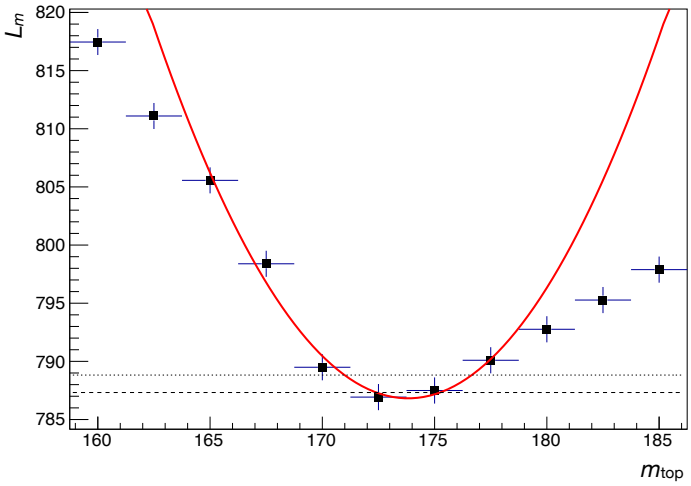

Figure 7.5: MEM top mass measurement using 20 events of a particle level sample. Shown is the sample logLikelihood introduced in the text vs. the mass assumption used for the $t\bar{t}$ matrix element calculation. The minimum of the fitted parabola indicates the measured mass, while the intersections of the parabola and the dashed line gives the uncertainty. The dashed line indicates the half width ($\log(L/L_{\text{max}}) = 0.5$), the dotted line indicates ($\log(L/L_{\text{max}}) = 2$).

event weights, the so-called sample logLikelihood:

$$L_m = -\sum_{i,i\in\text{data}} \log \frac{p(x_i|\alpha_m)}{\sigma_m^{fid}}, m \in (160, 162.5, ..., 185)\ \text{GeV} \tag{7.14}$$

The $t\bar{t}$ production cross section σ_m^{fid} depends on the top mass, this is taken care of explicitly by weighting the likelihood by it. The sample logLikelihood is expected to be minimal at the mass of the sample. For this test particle level samples were produced at different masses, with the two W bosons decaying into an electron and a muon. The process likelihoods are calculated using only 20 events. Fig. 7.5 shows this measurement undertaken on a simulated sample with a top mass of 172.5 GeV. Plotting the log sample likelihoods at their respective mass and fitting a parabola at the lowest four points results in a measured mass of 173.82 ± 1.42. Using particle level samples for this kind of test makes the use of any TFs unnecessary, since the full final state information is available.

7.4.2 Wt polarity

In order to test the correct implementation of the Wt matrix element, a spin correlation measurement is done like in Ref. [152]. The Wt process actually consists of

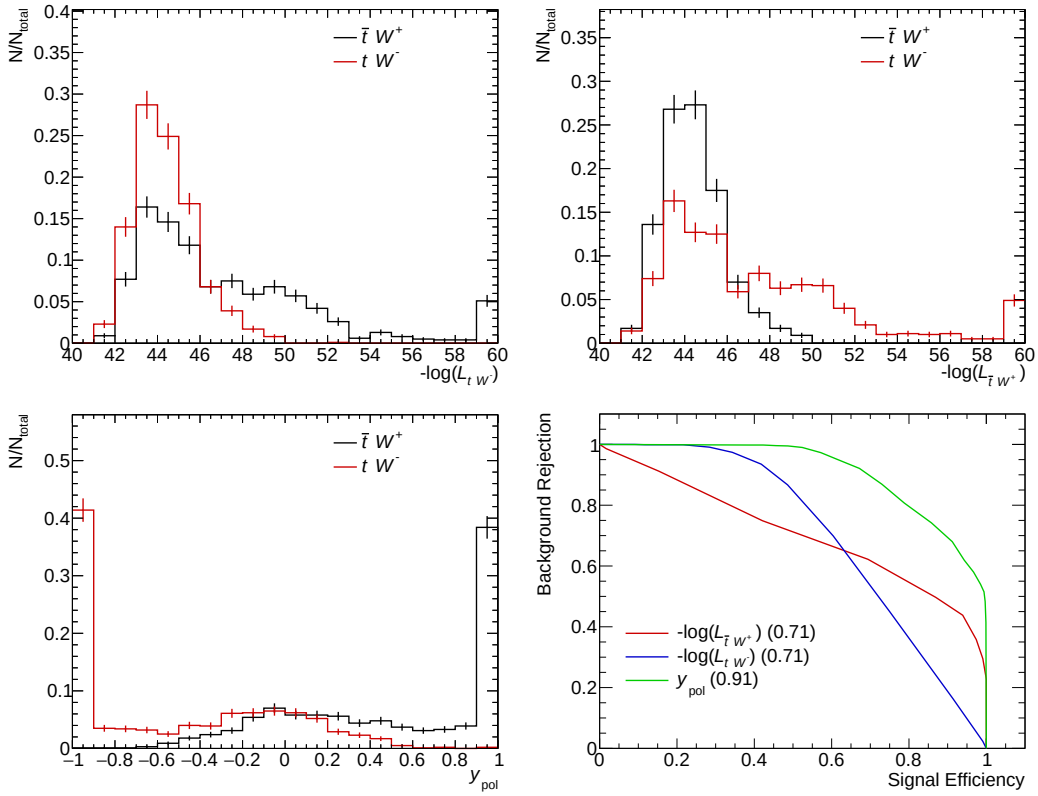

Figure 7.6: An example of a Wt polarity measurement. Shown are the matrix element likelihoods of tW^- (top left), $\bar{t}W^+$ (top right), the discriminant y_{pol} introduced in the text (bottom left), and the resulting ROC curves (bottom right). The combination of the single likelihoods into y_{pol} separates the $W^+\bar{t}$ and W^-t samples very well, as can also be seen in the very high ROC integral of 0.91 (right plot).

two processes: The $W^+\bar{t}$ and the W^-t processes, each occurring and the same rate at LHC. In case they would not occur at the same rate, a polarity would be present, stemming back to the $|V_{td}|$ CKM matrix element. Constructing a discriminant like

$$y_{\text{pol}} = \frac{p(x_i|\alpha_+) - p(x_i|\alpha_-)}{p(x_i|\alpha_+) + p(x_i|\alpha_-)} \tag{7.15}$$

makes it possible to separate the charge of the measured processes, with $\alpha_\pm$ being the assumption of the event being $W^+\bar{t}$ or W^-t, respectively. A first test calculates this discriminant on a particle level samples without the usage of any TFs. The result is shown in fig. 7.6. The left plot shows the distribution of this discriminant for two different samples, where the W^+ sample peaks at 1 while the W^- sample peaks at -1. The right plot shows the ROC curves for this discriminant and also the single probabilities. The discriminant exceeds the separation of single weights by

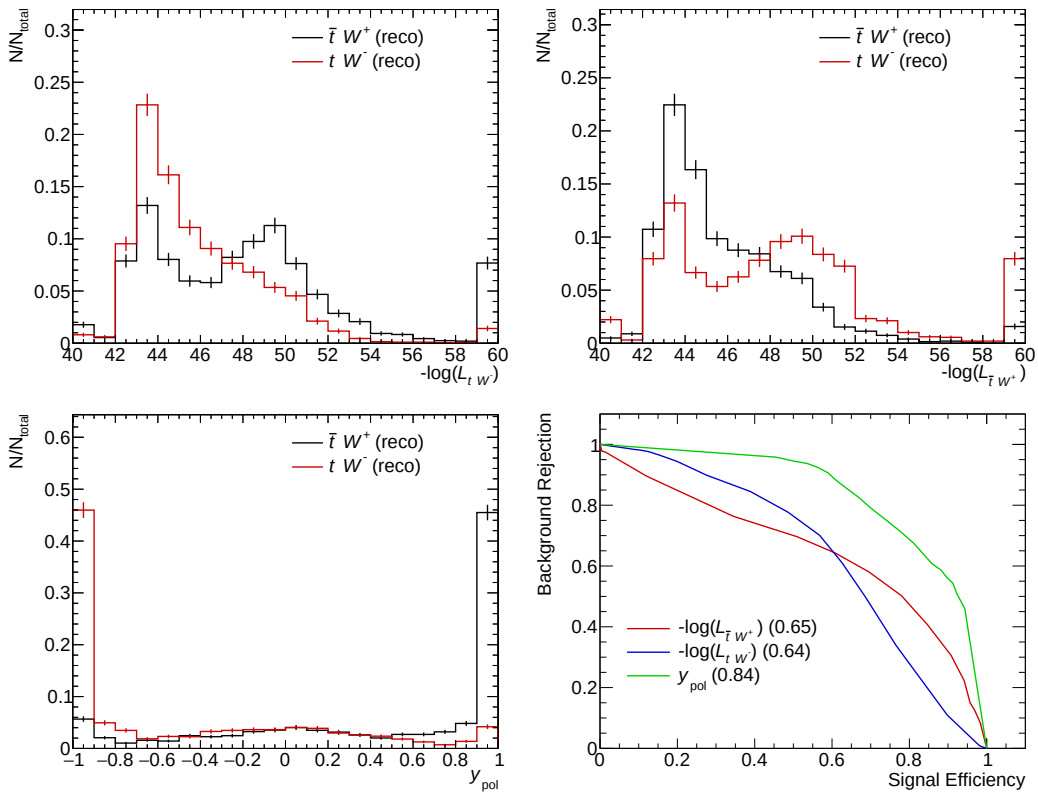

Figure 7.7: An example of a Wt polarity measurement, similar to the one shown in fig. 7.6, however using detector level events. Obviously there is an increased rate of mis-classifications of tW^- events as $\bar{t}W^+$ events and vice versa due to reconstruction losses.

far, having a ROC integral of 0.91, while the usage of only one weight calculation – e.g. only W^-t – would result in a ROC integral of only 0.7. This shows that the combination of several weights into a single discriminant can be very powerful.

A second test is undertaken on simulated detector level samples, however without making use of TFs. This shows similar results, as can be seen in Fig. 7.7. The detector level discrimination is not as strong as at particle level: Besides the missing TFs, no b-jet information was used but the jet with the highest transverse momentum (the leading jet) is assumed to be the b-jet. Due to this introduced uncertainty, there is an increased rate of mis-classifications of tW^- events as $\bar{t}W^+$ events and vice versa.

7.5 W^+W^- - $t\bar{t}$ production separation

A first step towards an actual W^+W^- implementation is a particle level separation of $t\bar{t}$ and W^+W^- events with $N_{\text{jets}} = 0$. This makes use of the 0-jet TF presented in

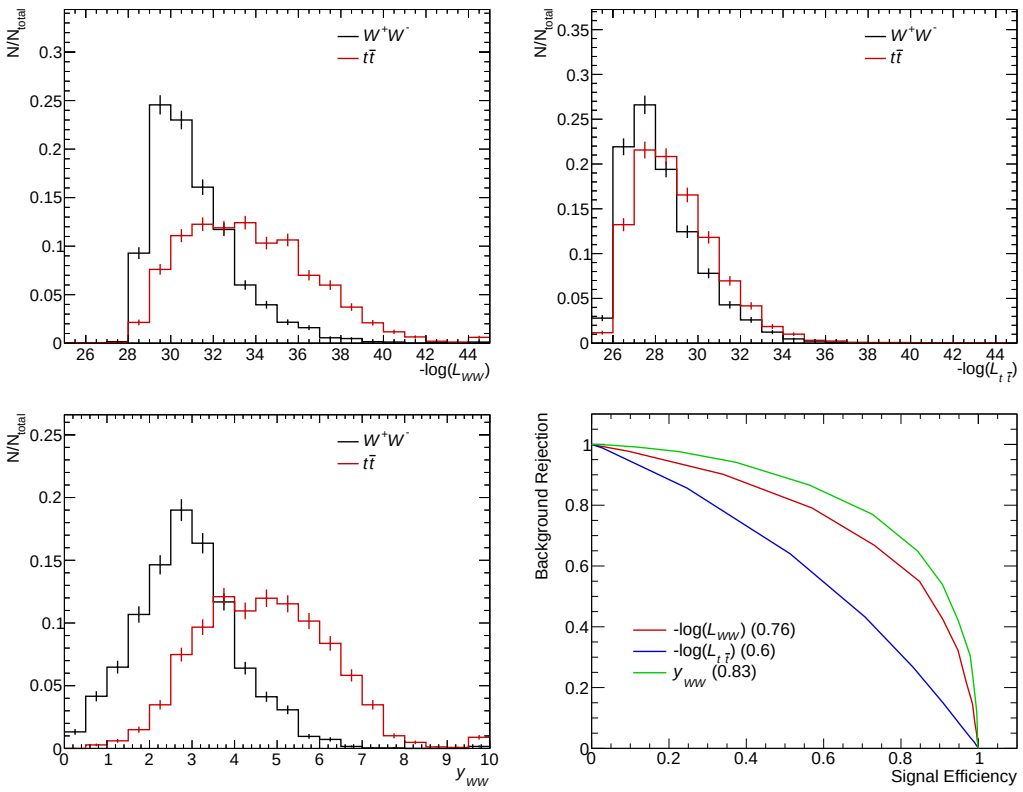

Figure 7.8: The MEM discriminant y_{WW} (bottom left) and ROC curve (bottom right) at particle level for a W^+W^- sample and a $t\bar{t}$ sample, as well as the individual likelihood results (top left and right). The $t\bar{t}$ sample is limited to events with jets being outside the W^+W^- fiducial region (see text). Even though no jet information is used, the two samples clearly can be separated using a MEM classifier.

Section 7.3.3, however without the reconstruction efficiencies applied. Two particle level sample were produced for this test: A $W^+W^- \to e\mu$ and a $t\bar{t} \to b\bar{b}e\mu$ sample. In order to simulate the 0-jet case, the b-jets of the $t\bar{t}$ sample have to lie outside the W^+W^- fiducial region, therefore no events with $p_T^b > 20\,\text{GeV}$ and $|\eta^b| < 4.5$ are selected. For providing sufficient statistics, 1 million events have to be simulated, leaving 2500 of these "fiducial events". The jet information is available but is ignored and the jet momenta are smeared over the invisible phase space ($p_T^b < 20\,\text{GeV}$ and $|\eta^b| > 4.5$) by the 0-jet TF. The right plot of Fig. 7.8 shows the normalised distribution of

$$y_{WW} = -\log \frac{\mathcal{L}_{WW}}{\mathcal{L}_{t\bar{t}} + \mathcal{L}_{WW}} \quad , \tag{7.16}$$

the left plot the resulting ROC curve, alongside the ROC curves of the single likelihoods. While the signal likelihood already provides some discrimination

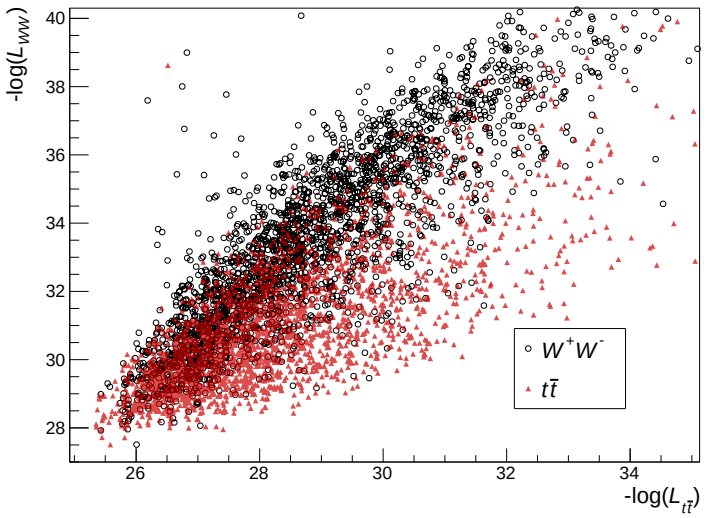

Figure 7.9: Scatter plot of the W^+W^- and $t\bar{t}$ log-likelihood result of the particle level 0-jet-$t\bar{t}$ and W^+W^- samples. The two samples show slightly different correlations and clusters within the 2-dimensional log-likelihood space.

power in this case, the combination of signal and background in d_{WW} surpasses the single weight calculation. This can also be seen by the ROC integral of 0.83 in case of d_{WW} compared to 0.76 and 0.6 of the integrals of $\mathcal{L}_{WW}$ and $\mathcal{L}_{t\bar{t}}$, respectively. The reason for this can also be seen in Fig. 7.9. This shows the W^+W^- and $t\bar{t}$ distributions within the 2-dimensional log $L_{W^+W^-}$ - log $L_{t\bar{t}}$ space. The distributions have visibly different correlations and scatter in general in different regions of the log-likelihood space, leading to a better separation of the samples.

Even though no detector level sample nor data was used for this test, it clearly shows that W^+W^- and top events clearly can be separated using MEM, even without any jet information being available.

Remark The scatter plot in Fig. 7.9 shows a very good example for the use of MVA techniques: Two different types of events show different clustering behaviour in a multi-dimensional variable space. Beside of the likelihood ratio, it might provide good input for a MLA, possibly leading to even better separation.

7.6 Conclusion

This chapter presented a possible MVA analysis of a W^+W^- cross section measurement, focusing on background separation. It outlines the necessary steps to do so using the MoMEMta toolkit, including the preparation of custom TFs and a first prove of principle on particle level events. A future analysis needs to apply

the gained resolution functions and reconstruction efficiencies on reconstruction level events and finally on data.

Due to the known limitations*, which are the usage of LO matrix elements and especially the information loss by non-reconstructed particles the final background separation power using a MEM classifier might not be as significant as presented on truth-level.

There are also more use-cases, which were not presented. For example MEM can be used for analysing the different W^+W^- production channels, presented in Fig. 2.4. Also analyses with $N_{\text{jets}} > 0$ have the benefit that less or no information of jet momenta is lost, while the whole analysis ansatz does not change significantly: For example it is not necessary to calculate the $W^+W^- + 2$ jets matrix element. It is sufficient to simply calculate the W^+W^- matrix element as already presented after boosting the system into the jet rest frame. This is possible, because the jets usually stem from initial state radiation and usually do not affect the actual matrix element.

However, as also stated in Ref. [152] and noted in the end of the previous section, the calculated MEM weights can be used as input of a machine learning algorithm.

There will be definitely a MVA analysis in the near future, possibly making use of more than only one MVA technique.

*Ref. [162] discusses known limitations and possible improvements in the near future, made possible by increasied computing power. Besides the usage of NLO matrix elements, also the parton showers, the jet substructure, the underlying event and an improved detector resolution based on the detector subsystems could be considered.

Chapter 8

Summary

This thesis presents and sums up the work done during my doctoral studies from 2016 to 2020 at DESY (Zeuthen) and the University of Sheffield. In this time two main topics were worked on.

Measurement of electron identification efficiencies The goals of the measurement presented in Chapter 5 was to reduce the systematic uncertainties and make it possible to track down the single sources of these uncertainties. Therefore, the Z_{mass} approach which was previously used by me in Ref. [1, 2] is completely rebuild. New background templates are introduced, being more consistent with the whole likelihood electron identification approach. The subtraction of signal contamination in these templates is optimised and the final background estimate is done using a template fit. Also new systematic variations targeting the template shapes and the signal contamination are introduced. The calculation of systematic uncertainties is changed, targeting the uncertainties on a measured default value, rather than the previous root-means-square approach. This also makes it easier to introduce sources of uncertainties. The new approach leads to better agreement with the alternate Z_{Iso} method, which leads to reduced the overall electron identification uncertainty stemming from the combination of the two methods.

Measurement of the W^+W^- production cross section Chapter 6 presents the measurement of the total and differential W^+W^- production cross section using 2015 and 2016 data [3]. The focus lays on my own contributions to this measurement. This included studies on the composition of fake background and most importantly the preparation of inputs for iterative Bayesian unfolding. The unfolding procedure is also cross checked such that it is made sure that no bias on the measurement on new physics is introduced by the method. Unfolding techniques are necessary in order to obtain differential cross sections from measured

differential distributions. In this sense, the shown work is a key feature of this measurement.

The last Chapter 7 focused on possible future W^+W^- cross section measurements, targeting the usage of the full ATLAS Run-2 dataset taken from 2015 to 2018. It introduces multivariate techniques, especially the matrix element method. This method calculates a MVA discriminant based on the theoretical likelihoods of event signatures. The necessary TFs are provided along side a first proof of principle of the method, such that a future measurement can be based on the presented work.

Acronyms

ALICE A Large Ion Collider Experiment.

aTGC anomalous triple gauge coupling.

ATLAS A Toroidal LHC ApparatuS.

BDT boosted decision tree.

BR branching ratio.

BSM beyond the Standard Model of particle physics.

CERN Conseil européen pour la recherche nucléaire.

CMS Compact Muon Solenoid.

CR control region.

CSC cathode strip chambers.

DY Drell-Yan.

EFT effective field theory.

EM calorimeter electromagnetic calorimeter.

FCal forward calorimeter.

FR fiducial region.

HEC hadronic end-cap calorimeter.

HLT high level trigger.

IBL inner B-Layer.

ID inner detector.

L1 hardware based level-1 trigger.

L1Calo level-1 calorimeter trigger.

L1Muon level-1 muon system trigger.

L1Topo level-1 topological trigger.

LAr liquid argon.

LEP Large Electron Positron Collider.

LHC Large Hadron Collider.

LHCb Large Hadron Collider beauty experiment.

LHCf Large Hadron Collider forward experiment.

Linac 2 Linear accelerator 2.

LL leading logarithm.

LLH likelihood.

LO leading order.

MC Monte Carlo.

MDT monitored drift tubes.

MEM matrix element method.

MLA machine learning algorithm.

MVA multivariate analysis.

NLO next-to-leading order.

NN neural network.

NNLO next-to-next-to-leading order.

NNLOPS next to next to leading order and parton shower.

Pdf probability density function.

PDF parton distribution function.

PS Proton Synchrotron.

PSB Proton Synchrotron Booster.

PU pile-up.

QCD quantum chromodynamics.

QED quantum electrodynamics.

QFT quantum field theory.

RF radio frequency.

ROC receiver operating characteristic.

SCT silicon strip detector.

SF scale factor.

SM Standard Model of particle physics.

SPS Super Proton Synchrotron.

SR signal region.

TF transfer-function.

TGC triple gauge coupling.

TOTEM Total, elastic and diffractive cross section measurement.

TRT transition radiation tracker.

VR validation region.

Bibliography

[1] ATLAS Collaboration, M. Aaboud et al., *Electron reconstruction and identification in the ATLAS experiment using the 2015 and 2016 LHC proton-proton collision data at $\sqrt{s}$ = 13 TeV*, Eur. Phys. J. C **79** (2019) 639, arXiv:1902.04655 [physics.ins-det].

[2] ATLAS Collaboration, G. Aad et al., *Electron and photon performance measurements with the ATLAS detector using the 2015-2017 LHC proton-proton collision data*, JINST **14** (2019) P12006, arXiv:1908.00005 [hep-ex].

[3] ATLAS Collaboration, M. Aaboud et al., *Measurement of fiducial and differential W^+W^- production cross-sections at $\sqrt{s} = 13$ TeV with the ATLAS detector*, Eur. Phys. J. C **79** (2019) 884, arXiv:1905.04242 [hep-ex].

[4] D. Harper, *Online Etymology Dictionary*, Entries of *physics, physic, *bheue-* , 2001. https://www.etymonline.com. last checked 2020-04-15.

[5] ATLAS Collaboration, G. Aad et al., *Observation of a new particle in the search for the Standard Model Higgs boson with the ATLAS detector at the LHC*, Phys. Lett. B **716** (2012) 1–29, arXiv:1207.7214 [hep-ex].

[6] CMS Collaboration, S. Chatrchyan et al., *Observation of a New Boson at a Mass of 125 GeV with the CMS Experiment at the LHC*, Phys. Lett. B **716** (2012) 30–61, arXiv:1207.7235 [hep-ex].

[7] H. Baer, V. Barger, A. Lessa, and X. Tata, *Supersymmetry discovery potential of the LHC at s**(1/2) = 10-TeV and 14-TeV without and with missing E(T)*, JHEP **09** (2009) 063, arXiv:0907.1922 [hep-ph].

[8] P. Salucci, *Dark Matter in Galaxies: evidences and challenges*, Found. Phys. **48** (2018) 1517–1537, arXiv:1807.08541 [astro-ph.GA].

[9] M. Klasen, M. Pohl, and G. Sigl, *Indirect and direct search for dark matter*, Prog. Part. Nucl. Phys. **85** (2015) 1–32, arXiv:1507.03800 [hep-ph].

[10] Nobel Media AB, *Advanced information*, NobelPrize.org, 2020. `https://www.nobelprize.org/prizes/physics/2017/advanced-information`.

[11] Super-Kamiokande Collaboration, Y. Fukuda et al., *Evidence for oscillation of atmospheric neutrinos*, Phys. Rev. Lett. **81** (1998) 1562–1567, `arXiv:hep-ex/9807003`.

[12] SNO Collaboration, Q. Ahmad et al., *Measurement of the rate of $\nu_e + d \to p + p + e^-$ interactions produced by ^8B solar neutrinos at the Sudbury Neutrino Observatory*, Phys. Rev. Lett. **87** (2001) 071301, `arXiv:nucl-ex/0106015`.

[13] SNO Collaboration, Q. Ahmad et al., *Direct evidence for neutrino flavor transformation from neutral current interactions in the Sudbury Neutrino Observatory*, Phys. Rev. Lett. **89** (2002) 011301, `arXiv:nucl-ex/0204008`.

[14] L. Willmann and K. Jungmann, *Matter-Antimatter Asymmetry - Aspects at Low Energy*, Annalen Phys. **528** (2016) 108–114, `arXiv:1506.03001 [hep-ph]`.

[15] P. A. M. Dirac, *The Quantum Theory of the Electron*, Proceedings of the Royal Society A: Mathematical, Physical and Engineering Sciences **117** (1928) 610–624.

[16] P. A. M. Dirac, *The Quantum Theory of the Emission and Absorption of Radiation*, Proceedings of the Royal Society A: Mathematical, Physical and Engineering Sciences **114** (1927) 243–265.

[17] S. Tomonaga, *On a relativistically invariant formulation of the quantum theory of wave fields*, Prog. Theor. Phys. **1** (1946) 27–42.

[18] J. Schwinger, *Quantum Electrodynamics. I, A Covariant Formulation*, Physical Review **74** (1948) 1439–1461.

[19] R. P. Feynman, *Space-Time Approach to Quantum Electrodynamics*, Physical Review **76** (1949) 769–789.

[20] C. N. Yang and R. L. Mills, *Conservation of Isotopic Spin and Isotopic Gauge Invariance*, Phys. Rev. **96** (1954) 191–195.

[21] S. L. Glashow, *Partial-symmetries of weak interactions*, Nuclear Physics **22** (1961) 579–588.

[22] S. Weinberg, *A Model of Leptons*, Physical Review Letters **19** (1967) 1264–1266.

[23] A. Salam, *Weak and Electromagnetic Interactions*, Conf. Proc. C **680519** (1968) 367–377.

[24] P. Higgs, *Broken symmetries, massless particles and gauge fields*, Physics Letters **12** (1964) 132–133.

[25] F. Englert and R. Brout, *Broken Symmetry and the Mass of Gauge Vector Mesons*, Phys. Rev. Lett. **13** (1964) 321–323.

[26] G. S. Guralnik, C. R. Hagen, and T. W. B. Kibble, *Global Conservation Laws and Massless Particles*, Phys. Rev. Lett. **13** (1964) 585–587.

[27] W. Buchmüller and C. Lüdeling, *Field Theory and Standard Model*, in *2005 European School of High-Energy Physics*. 2006. `arXiv:hep-ph/0609174`.

[28] S. Novaes, *Standard model: An Introduction*, in *10th Jorge Andre Swieca Summer School: Particle and Fields*. 1999. `arXiv:hep-ph/0001283`.

[29] M. E. Peskin and D. V. Schroeder, *An Introduction to quantum field theory*. Addison-Wesley, Reading, USA, 1995.

[30] C. Berger, *Elementarteilchenphysik (in German)*. Springer Spektrum, Heidelberg, Germany, 2014.

[31] O. Nachtmann, *Phänomene und Konzepte der Elementarteilchenphysik (in German)*. Vieweg, Braunschweig, Germany, 1986.

[32] W. Cottingham and D. Greenwood, *An introduction to the standard model of particle physics*. Cambridge University Press, 2007.

[33] E. Rüttinger, *Investigation of anomalous Triple Gauge Couplings in W^+W^--Events with the ATLAS detector*, Master's thesis, Humboldt-Universität zu Berlin, 2016.

[34] Particle Data Group Collaboration, K. Olive et al., *Review of Particle Physics*, Chin. Phys. C **38** (2014) 090001.

[35] C. Degrande et al., *Effective Field Theory: A Modern Approach to Anomalous Couplings*, Annals Phys. **335** (2013) 21–32, `arXiv:1205.4231 [hep-ph]`.

[36] H. Aihara et al., *Anomalous gauge boson interactions*, Electroweak Symmetry Breaking and New Physics at the TeV Scale (1997) 488–546, `arXiv:hep-ph/9503425`.

[37] J. Bjorken, *Asymptotic Sum Rules at Infinite Momentum*, Phys. Rev. **179** (1969) 1547–1553.

[38] Particle Data Group Collaboration, M. Tanabashi et al., *Review of Particle Physics*, Phys. Rev. D **98** (2018) 030001.

[39] T. Gleisberg et al., *Event generation with SHERPA 1.1*, JHEP **02** (2009) 007, arXiv:0811.4622 [hep-ph].

[40] S. Marzani, G. Soyez, and M. Spannowsky, *Looking inside jets: an introduction to jet substructure and boosted-object phenomenology*, vol. 958. Springer, 2019. arXiv:1901.10342 [hep-ph].

[41] V. Coco et al., *Jets and jet algorithms*, in *HERA and the LHC: 4th Workshop on the Implications of HERA for LHC Physics*. 2009.

[42] S. Dawson et al., *Resummation of jet veto logarithms at N^3LL_a + NNLO for W^+W^- production at the LHC*, Phys. Rev. D **94** (2016) 114014, arXiv:1606.01034 [hep-ph].

[43] P. Jaiswal and T. Okui, *Explanation of the WW excess at the LHC by jet-veto resummation*, Phys. Rev. D **90** (2014) 073009, arXiv:1407.4537 [hep-ph].

[44] P. F. Monni and G. Zanderighi, *On the excess in the inclusive $W^+W^- \to l^+l^-\nu\bar{\nu}$ cross section*, JHEP **05** (2015) 013, arXiv:1410.4745 [hep-ph].

[45] M. Grazzini et al., *W^+W^- production at the LHC: fiducial cross sections and distributions in NNLO QCD*, JHEP **08** (2016) 140, arXiv:1605.02716 [hep-ph].

[46] T. Gehrmann et al., *W^+W^- Production at Hadron Colliders in Next to Next to Leading Order QCD*, Phys. Rev. Lett. **113** (2014) 212001, arXiv:1408.5243 [hep-ph].

[47] F. Caola et al., *QCD corrections to W^+W^- production through gluon fusion*, Phys. Lett. B **754** (2016) 275–280, arXiv:1511.08617 [hep-ph].

[48] E. Re, M. Wiesemann, and G. Zanderighi, *NNLOPS accurate predictions for W^+W^- production*, JHEP **12** (2018) 121, arXiv:1805.09857 [hep-ph].

[49] K. Hamilton et al., *Merging WW and WW+jet with MINLO*, JHEP **09** (2016) 057, arXiv:1606.07062 [hep-ph].

[50] ATLAS Collaboration, G. Aad et al., *The ATLAS Simulation Infrastructure*, Eur. Phys. J. C **70** (2010) 823–874, arXiv:1005.4568 [physics.ins-det].

[51] GEANT4 Collaboration, S. Agostinelli et al., *GEANT4–a simulation toolkit*, Nucl. Instrum. Meth. A **506** (2003) 250–303.

[52] L. Evans and P. Bryan, *LHC Machine*, JINST **3** (2008) S08001.

[53] ATLAS Collaboration, G. Aad et al., *The ATLAS Experiment at the CERN Large Hadron Collider*, JINST **3** (2008) S08003.

[54] CMS Collaboration, S. Chatrchyan et al., *The CMS Experiment at the CERN LHC*, JINST **3** (2008) S08004.

[55] ALICE Collaboration, K. Aamodt et al., *The ALICE experiment at the CERN LHC*, JINST **3** (2008) S08002.

[56] LHCb Collaboration, J. Alves, A.Augusto et al., *The LHCb Detector at the LHC*, JINST **3** (2008) S08005.

[57] TOTEM Collaboration, G. Anelli et al., *The TOTEM experiment at the CERN Large Hadron Collider*, JINST **3** (2008) S08007.

[58] LHCf Collaboration, O. Adriani et al., *The LHCf detector at the CERN Large Hadron Collider*, JINST **3** (2008) S08006.

[59] E. Mobs, *The CERN accelerator complex*, OPEN-PHO-ACCEL-2018-005, 2018. https://cds.cern.ch/record/2636343.

[60] S. Gilardoni (ed) et al., *Fifty years of the CERN Proton Synchrotron : Volume 2*, arXiv:1309.6923 [physics.acc-ph].

[61] *Linear accelerator 2*, CERN website, 2012. https://cds.cern.ch/record/1997427.

[62] *The Proton Synchrotron Booster*, CERN website, 2012. https://cds.cern.ch/record/1997372.

[63] *The Proton Synchrotron*, CERN website, 2012. https://cds.cern.ch/record/1997189.

[64] *The Super Proton Synchrotron*, CERN website, 2012. https://cds.cern.ch/record/1997189.

[65] *Radiofrequency cavities*, CERN website, 2012. https://cds.cern.ch/record/1997424.

[66] ATLAS Collaboration, *Luminosity determination in pp collisions at $\sqrt{s} = 13$ TeV using the ATLAS detector at the LHC*, ATLAS-CONF-2019-021, 2019, https://cds.cern.ch/record/2677054.

[67] ATLAS Collaboration, *LuminosityPublicResultsRun2*, ATLAS Experiment – Public Results, 2019. https://twiki.cern.ch/twiki/bin/view/AtlasPublic/LuminosityPublicResultsRun2.

[68] J. Pequenao, *Computer generated image of the whole ATLAS detector*, CERN-GE-0803012, 2008. https://cds.cern.ch/record/1095924.

[69] K. Potamianos, *The upgraded Pixel detector and the commissioning of the Inner Detector tracking of the ATLAS experiment for Run-2 at the Large Hadron Collider*, PoS **EPS-HEP2015** (2015) 261, arXiv:1608.07850 [physics.ins-det].

[70] ATLAS Collaboration, M. Aaboud et al., *Reconstruction of primary vertices at the ATLAS experiment in Run 1 proton–proton collisions at the LHC*, Eur. Phys. J. C **77** (2017) 332, arXiv:1611.10235 [physics.ins-det].

[71] ATLAS Collaboration Collaboration, M. Capeans et al., *ATLAS Insertable B-Layer Technical Design Report*, ATLAS-TDR-19, 2010. https://cds.cern.ch/record/1291633.

[72] ATLAS Collaboration, *ATLAS Insertable B-Layer Technical Design Report Addendum*, ATLAS-TDR-19-ADD-1, 2012. http://cds.cern.ch/record/1451888.

[73] ATLAS Collaboration, B. Mindur, *ATLAS Transition Radiation Tracker (TRT): Straw tubes for tracking and particle identification at the Large Hadron Collider*, Nucl. Instrum. Meth. A **845** (2017) 257–261.

[74] A. Yamamoto et al., *The ATLAS central solenoid*, Nucl. Instrum. Meth. A **584** (2008) 53–74.

[75] ATLAS Collaboration, M. Aaboud et al., *Measurement of the photon identification efficiencies with the ATLAS detector using LHC Run-1 data*, Eur. Phys. J. C **76** (2016) 666, arXiv:1606.01813 [hep-ex].

[76] C. Fabjan and F. Gianotti, *Calorimetry for particle physics*, Rev. Mod. Phys. **75** (2003) 1243–1286.

[77] ATLAS Collaboration, *ATLAS level-1 trigger: Technical Design Report*, ATLAS-TDR-12, 1998. http://cds.cern.ch/record/381429.

[78] ATLAS Collaboration, A. Martínez, *The Run-2 ATLAS Trigger System*, J. Phys. Conf. Ser. **762** (2016) 012003.

[79] M. Nedden, *The LHC Run 2 ATLAS trigger system: design, performance and plans*, JINST **12** (2017) C03024.

[80] ATLAS Collaboration, M. Aaboud et al., *Measurement of the photon identification efficiencies with the ATLAS detector using LHC Run 2 data collected in 2015 and 2016*, Eur. Phys. J. C **79** (2019) 205, arXiv:1810.05087 [hep-ex].

[81] W. Lampl et al., *Calorimeter clustering algorithms: Description and performance*, ATL-LARG-PUB-2008-002, 2008, https://cds.cern.ch/record/1099735.

[82] T. G. Cornelissen et al., *The global χ^2 track fitter in ATLAS*, J. Phys. Conf. Ser. **119** (2008) 032013.

[83] ATLAS Collaboration, *Improved electron reconstruction in ATLAS using the Gaussian Sum Filter-based model for bremsstrahlung*, ATLAS-CONF-2012-047, 2012, https://cds.cern.ch/record/1449796.

[84] ATLAS Collaboration, G. Aad et al., *Muon reconstruction performance of the ATLAS detector in proton–proton collision data at $\sqrt{s}$ =13 TeV*, Eur. Phys. J. C **76** (2016) 292, arXiv:1603.05598 [hep-ex].

[85] J. Illingworth and J. Kittler, *A survey of the hough transform*, Computer Vision, Graphics, and Image Processing **44** (1988) 87–116.

[86] ATLAS Collaboration, *Measurement of the tau lepton reconstruction and identification performance in the ATLAS experiment using pp collisions at $\sqrt{s} = 13$ TeV*, ATLAS-CONF-2017-029, 2017, http://cds.cern.ch/record/2261772.

[87] R. Atkin, *Review of jet reconstruction algorithms*, J. Phys. Conf. Ser. **645** (2015) 012008.

[88] S. D. Ellis and D. E. Soper, *Successive combination jet algorithm for hadron collisions*, Phys. Rev. D **48** (1993) 3160–3166, arXiv:hep-ph/9305266.

[89] M. Cacciari, G. P. Salam, and G. Soyez, *The anti-k_t jet clustering algorithm*, JHEP **04** (2008) 063, arXiv:0802.1189 [hep-ph].

[90] L. Asquith et al., *Performance of Jet Algorithms in the ATLAS Detector*, ATL-PHYS-INT-2010-129, 2010, https://cds.cern.ch/record/1311867, ATLAS Internal Communication.

[91] M. Cacciari, G. P. Salam, and G. Soyez, *FastJet User Manual*, Eur. Phys. J. C **72** (2012) 1896, arXiv:1111.6097 [hep-ph].

[92] ATLAS Collaboration, G. Aad et al., *Topological cell clustering in the ATLAS calorimeters and its performance in LHC Run 1*, Eur. Phys. J. C **77** (2017) 490, arXiv:1603.02934 [hep-ex].

[93] ATLAS Collaboration, *Performance of the ATLAS Inner Detector Track and Vertex Reconstruction in the High Pile-Up LHC Environment*, ATLAS-CONF-2012-042, 2012, https://cds.cern.ch/record/1435196.

[94] ATLAS Collaboration, G. Aad et al., *A neural network clustering algorithm for the ATLAS silicon pixel detector*, JINST **9** (2014) P09009, arXiv:1406.7690 [hep-ex].

[95] ATLAS Collaboration, *Properties of Jets and Inputs to Jet Reconstruction and Calibration with the ATLAS Detector Using Proton-Proton Collisions at* $\sqrt{s} = 13$ *TeV*, ATL-PHYS-PUB-2015-036, 2015, https://cds.cern.ch/record/2044564.

[96] ATLAS Collaboration, M. Aaboud et al., *Jet energy scale measurements and their systematic uncertainties in proton-proton collisions at* $\sqrt{s} = 13$ *TeV with the ATLAS detector*, Phys. Rev. D **96** (2017) 072002, arXiv:1703.09665 [hep-ex].

[97] ATLAS Collaboration, *Constituent-level pile-up mitigation techniques in ATLAS*, ATLAS-CONF-2017-065, 2017, https://cds.cern.ch/record/2281055.

[98] ATLAS Collaboration, G. Aad et al., *Performance of pile-up mitigation techniques for jets in* pp *collisions at* $\sqrt{s} = 8$ *TeV using the ATLAS detector*, Eur. Phys. J. C **76** (2016) 581, arXiv:1510.03823 [hep-ex].

[99] ATLAS Collaboration, M. Aaboud et al., *Identification and rejection of pile-up jets at high pseudorapidity with the ATLAS detector*, Eur. Phys. J. C **77** (2017) 580, arXiv:1705.02211 [hep-ex], [Erratum: Eur.Phys.J.C 77, 712 (2017)].

[100] ATLAS Collaboration, *Expected performance of the ATLAS b-tagging algorithms in Run-2*, ATL-PHYS-PUB-2015-022, 2015, https://cds.cern.ch/record/2037697.

[101] ATLAS Collaboration, *Commissioning of the ATLAS b-tagging algorithms using* $t\bar{t}$ *events in early Run-2 data*, ATL-PHYS-PUB-2015-039, 2015, https://cds.cern.ch/record/2047871.

[102] ATLAS Collaboration, G. Aad et al., *Performance of algorithms that reconstruct missing transverse momentum in $\sqrt{s} = 8$ TeV proton-proton collisions in the ATLAS detector*, Eur. Phys. J. C **77** (2017) 241, arXiv:1609.09324 [hep-ex].

[103] ATLAS Collaboration, M. Aaboud et al., *Performance of missing transverse momentum reconstruction with the ATLAS detector using proton-proton collisions at $\sqrt{s}$ = 13 TeV*, Eur. Phys. J. C **78** (2018) 903, arXiv:1802.08168 [hep-ex].

[104] D. Adams et al., *Recommendations of the Physics Objects and Analysis Harmonisation Study Groups 2014*, ATL-PHYS-INT-2014-018, 2014, https://cds.cern.ch/record/1743654, ATLAS Internal Communication.

[105] R. M. Jacobs, *Probing new physics with boosted $H \to b\bar{b}$ decays with the ATLAS detector at 13 TeV*. PhD thesis, Rheinische Friedrich-Wilhelms-Universität Bonn, 2019. https://cds.cern.ch/record/2697316.

[106] ATLAS Collaboration, M. Aaboud et al., *Electron efficiency measurements with the ATLAS detector using 2012 LHC proton–proton collision data*, Eur. Phys. J. C **77** (2017) 195, arXiv:1612.01456 [hep-ex].

[107] R. Brun and F. Rademakers, *ROOT: An object oriented data analysis framework*, Nucl. Instrum. Meth. A **389** (1997) 81–86.

[108] S. Alioli et al., *NLO vector-boson production matched with shower in POWHEG*, JHEP **07** (2008) 060, arXiv:0805.4802 [hep-ph].

[109] T. Sjostrand, S. Mrenna, and P. Z. Skands, *A Brief Introduction to PYTHIA 8.1*, Comput. Phys. Commun. **178** (2008) 852–867, arXiv:0710.3820 [hep-ph].

[110] H.-L. Lai et al., *New parton distributions for collider physics*, Phys. Rev. D **82** (2010) 074024, arXiv:1007.2241 [hep-ph].

[111] ATLAS Collaboration, G. Aad et al., *Measurement of the Z/γ^* boson transverse momentum distribution in pp collisions at $\sqrt{s}$ = 7 TeV with the ATLAS detector*, JHEP **09** (2014) 145, arXiv:1406.3660 [hep-ex].

[112] J. Pumplin et al., *New generation of parton distributions with uncertainties from global QCD analysis*, JHEP **07** (2002) 012, arXiv:hep-ph/0201195 [hep-ph].

[113] N. Davidson, T. Przedzinski, and Z. Was, *PHOTOS interface in C++: Technical and Physics Documentation*, Comput. Phys. Commun. **199** (2016) 86–101, arXiv:1011.0937 [hep-ph].

[114] ATLAS Collaboration, *The Pythia 8 A3 tune description of ATLAS minimum bias and inelastic measurements incorporating the Donnachie-Landshoff diffractive model*, ATL-PHYS-PUB-2016-017, 2016, https://cds.cern.ch/record/2206965.

[115] R. D. Ball et al., *Parton distributions with LHC data*, Nucl. Phys. B **867** (2013) 244–289, arXiv:1207.1303 [hep-ph].

[116] ATLAS Collaboration, M. Aaboud et al., *Performance of the ATLAS Track Reconstruction Algorithms in Dense Environments in LHC Run 2*, Eur. Phys. J. C **77** (2017) 673, arXiv:1704.07983 [hep-ex].

[117] ATLAS Collaboration, G. Aad et al., *ATLAS data quality operations and performance for 2015–2018 data-taking*, JINST **15** (2020) P04003, arXiv:1911.04632 [physics.ins-det].

[118] W. Verkerke and D. P. Kirkby, *The RooFit toolkit for data modeling*, eConf **C0303241** (2003) MOLT007, arXiv:physics/0306116.

[119] J. H. Friedman, *Data Analysis Techniques for High-Energy Particle Physics*, in *3rd CERN School of Computing*. 10, 1974. https://cds.cern.ch/record/695770.

[120] F. James, *MINUIT: Function Minimization and Error Analysis Reference Manual*, CERN Program Library Long Writeups, CERNLIB-D506, 1998. https://cds.cern.ch/record/2296388.

[121] CDF Collaboration, C. Blocker, *Uncertainties on Efficiencies*, CDF-7168, 2004. https://www-cdf.fnal.gov/physics/statistics/notes/cdf6506_systematics.ps.

[122] X. Su, *Electron efficiencies calculated using the Z_{iso} method*, 2020. Private Communication.

[123] E. Auge, J. Dumarchez, and J. Tran Thanh Van, eds., *Proceedings, 53rd Rencontres de Moriond on Electroweak Interactions and Unified Theories (Moriond EW 2018): La Thuile, Italy, March 10-17, 2018*. 2018.

[124] P. Sommer, *Electron Scale Factor recommendations, calculated combining the Z_{iso} and Z_{mass} method*, 2020. Private Communication.

[125] ATLAS Collaboration, G. Aad et al., *Measurement of total and differential W^+W^- production cross sections in proton-proton collisions at $\sqrt{s} = 8$ TeV with*

the ATLAS detector and limits on anomalous triple-gauge-boson couplings, JHEP **09** (2016) 029, arXiv:1603.01702 [hep-ex].

[126] ATLAS Collaboration, M. Aaboud et al., *Measurement of the W^+W^- production cross section in pp collisions at a centre-of-mass energy of $\sqrt{s}$ = 13 TeV with the ATLAS experiment*, Phys. Lett. B **773** (2017) 354–374, arXiv:1702.04519 [hep-ex].

[127] ATLAS Collaboration, M. Aaboud et al., *Performance of the ATLAS Trigger System in 2015*, Eur. Phys. J. C **77** (2017) 317, arXiv:1611.09661 [hep-ex].

[128] ATLAS Collaboration, *Electron efficiency measurements with the ATLAS detector using the 2015 LHC proton–proton collision data*, ATLAS-CONF-2016-024, 2016, https://cds.cern.ch/record/2157687.

[129] B. Mellado, X. Ruan, and Z. Zhang, *Extraction of Top Backgrounds in the Higgs Boson Search with the $H \to WW^\star \to \ell\ell + E_T^{\text{miss}}$ Decay with a Full-Jet Veto at the LHC*, Phys. Rev. D **84** (2011) 096005, arXiv:1101.1383 [hep-ph].

[130] ATLAS Collaboration, M. Aaboud et al., *Measurements of gluon-gluon fusion and vector-boson fusion Higgs boson production cross-sections in the $H \to WW^* \to e\nu\mu\nu$ decay channel in pp collisions at $\sqrt{s} = 13$ TeV with the ATLAS detector*, Phys. Lett. B **789** (2019) 508–529, arXiv:1808.09054 [hep-ex].

[131] ATLAS Collaboration, *ATLAS Pythia 8 tunes to 7 TeV data*, ATL-PHYS-PUB-2014-021, 2014, https://cds.cern.ch/record/1966419.

[132] Sherpa Collaboration, E. Bothmann et al., *Event Generation with Sherpa 2.2*, SciPost Phys. **7** (2019) 034, arXiv:1905.09127 [hep-ph].

[133] V. Blobel, *Data Analysis in High Energy Physics – Chapter 6: Unfolding*. John Wiley & Sons, Ltd, 2013.

[134] A. J. Barr, *Measuring slepton spin at the LHC*, JHEP **02** (2006) 042, arXiv:hep-ph/0511115 [hep-ph].

[135] G. D'Agostini, *A Multidimensional unfolding method based on Bayes' theorem*, Nucl. Instrum. Meth. A **362** (1995) 487–498.

[136] G. D'Agostini, *Improved iterative Bayesian unfolding*, in *Alliance Workshop on Unfolding and Data Correction*. 2010. arXiv:1010.0632 [physics.data-an].

[137] S. Frixione and B. R. Webber, *Matching NLO QCD computations and parton shower simulations*, JHEP **06** (2002) 029, arXiv:hep-ph/0204244.

[138] ATLAS Collaboration, G. Aad et al., *Measurement of the $WW + WZ$ cross section and limits on anomalous triple gauge couplings using final states with one lepton, missing transverse momentum, and two jets with the ATLAS detector at $\sqrt{s} = 7$ TeV*, JHEP **01** (2015) 049, arXiv:1410.7238 [hep-ex].

[139] H. Voss, *Data Analysis in High Energy Physics – Chapter 5: Classification*. John Wiley & Sons, Ltd, 2013.

[140] T. Fawcett, *An introduction to ROC analysis*, Pattern Recognition Letters **27** (2006) 861–874.

[141] K. Albertsson et al., *Machine Learning in High Energy Physics Community White Paper*, J. Phys. Conf. Ser. **1085** (2018) 022008, arXiv:1807.02876 [physics.comp-ph].

[142] P. C. Bhat, *Multivariate Analysis Methods in Particle Physics*, Ann. Rev. Nucl. Part. Sci. **61** (2011) 281–309.

[143] J. Neyman and E. S. Pearson, *On the Problem of the Most Efficient Tests of Statistical Hypotheses*, Philosophical Transactions of the Royal Society of London. Series A, Containing Papers of a Mathematical or Physical Character **231** (1933) 289–337.

[144] K. Kondo, *Dynamical Likelihood Method for Reconstruction of Events With Missing Momentum. 1: Method and Toy Models*, J. Phys. Soc. Jap. **57** (1988) 4126–4140.

[145] P. Rieck, *Measurement of s-channel single top-quark production with the ATLAS detector using total event likelihoods*. PhD thesis, Humboldt-Universität zu Berlin, 2016. http://cds.cern.ch/record/2230028.

[146] R. H. Dalitz and G. R. Goldstein, *The Decay and polarization properties of the top quark*, Phys. Rev. D **45** (1992) 1531–1543.

[147] DØ Collaboration, B. Abbott et al., *Measurement of the Top Quark Mass in the Dilepton Channel*, Phys. Rev. D **60** (1999) 052001, arXiv:hep-ex/9808029.

[148] CMS Collaboration, V. Khachatryan et al., *Search for a Standard Model Higgs Boson Produced in Association with a Top-Quark Pair and Decaying to Bottom Quarks Using a Matrix Element Method*, Eur. Phys. J. C **75** (2015) 251, arXiv:1502.02485 [hep-ex].

[149] ATLAS Collaboration, G. Aad et al., *Search for the Standard Model Higgs boson produced in association with top quarks and decaying into $b\bar{b}$ in pp collisions at $\sqrt{s}$ = 8 TeV with the ATLAS detector*, Eur. Phys. J. C **75** (2015) 349, arXiv:1503.05066 [hep-ex].

[150] S. Wertz, *The Matrix Element Method at the LHC: status and prospects for Run II*, Journal of Physics: Conference Series **762** (2016) 012053.

[151] P. Artoisenet et al., *Automation of the matrix element reweighting method*, JHEP **12** (2010) 068, arXiv:1007.3300 [hep-ph].

[152] S. Brochet et al., *MoMEMta, a modular toolkit for the Matrix Element Method at the LHC*, Eur. Phys. J. C **79** (2019) 126, arXiv:1805.08555 [hep-ph].

[153] F. Fiedler et al., *The Matrix Element Method and its Application in Measurements of the Top Quark Mass*, Nucl. Instrum. Meth. A **624** (2010) 203–218, arXiv:1003.1316 [hep-ex].

[154] J. Alwall et al., *The automated computation of tree-level and next-to-leading order differential cross sections, and their matching to parton shower simulations*, JHEP **07** (2014) 079, arXiv:1405.0301 [hep-ph].

[155] A. Buckley et al., *LHAPDF6: parton density access in the LHC precision era*, Eur. Phys. J. C **75** (2015) 132, arXiv:1412.7420 [hep-ph].

[156] G. Lepage, *A New Algorithm for Adaptive Multidimensional Integration*, J. Comput. Phys. **27** (1978) 192–203.

[157] T. Hahn, *CUBA: A Library for multidimensional numerical integration*, Comput. Phys. Commun. **168** (2005) 78–95, arXiv:hep-ph/0404043.

[158] S. Stamm, *Combined Measurement of Single Top-Quark Production in the s and t-Channel with the ATLAS Detector and Effective Field Theory Interpretation*. PhD thesis, Humboldt-Universität zu Berlin, 2018.

[159] ATLAS Collaboration, G. Aad et al., *Evidence for single top-quark production in the s-channel in proton-proton collisions at $\sqrt{s}$ =8 TeV with the ATLAS detector using the Matrix Element Method*, Phys. Lett. B **756** (2016) 228–246, arXiv:1511.05980 [hep-ex].

[160] H. Mildner, *Resolution functions calculated using simulated $t\bar{t}$ events*, 2019. Private Communication.

[161] DØ Collaboration, V. M. Abazov et al., *Measurement of the Top Quark Mass Using the Matrix Element Technique in Dilepton Final States*, Phys. Rev. D **94** (2016) 032004, arXiv:1606.02814 [hep-ex].

[162] J. S. Gainer et al., *The Matrix Element Method: Past, Present, and Future*, in *Community Summer Study 2013: Snowmass on the Mississippi*. 2013. arXiv:1307.3546 [hep-ph].